

Winter 2004

# Nucleation and growth kinetics of tin and tin -silver alloy during initial stages of electrodeposition

Zhongqin Zhang

*University of New Hampshire, Durham*

Follow this and additional works at: <https://scholars.unh.edu/dissertation>

---

## Recommended Citation

Zhang, Zhongqin, "Nucleation and growth kinetics of tin and tin -silver alloy during initial stages of electrodeposition" (2004).  
*Doctoral Dissertations*. 254.  
<https://scholars.unh.edu/dissertation/254>

This Dissertation is brought to you for free and open access by the Student Scholarship at University of New Hampshire Scholars' Repository. It has been accepted for inclusion in Doctoral Dissertations by an authorized administrator of University of New Hampshire Scholars' Repository. For more information, please contact [nicole.hentz@unh.edu](mailto:nicole.hentz@unh.edu).

**NUCLEATION AND GROWTH KINETICS OF TIN  
AND TIN-SILVER ALLOY DURING INITIAL  
STAGES OF ELECTRODEPOSITION**

BY  
ZHONGQIN ZHANG

Baccalaureate Degree In Light Chemical Engineering (1983)  
Master's Degree In Applied Chemistry (Environmental Chemical Engineering) (1986)  
South China University of Technology

DISSERTATION

Submitted to the University of New Hampshire  
in Partial Fulfillment of  
the Requirements for the Degree of

Doctor of Philosophy  
In  
Chemical Engineering

December, 2004

UMI Number: 3158683

### INFORMATION TO USERS

The quality of this reproduction is dependent upon the quality of the copy submitted. Broken or indistinct print, colored or poor quality illustrations and photographs, print bleed-through, substandard margins, and improper alignment can adversely affect reproduction.

In the unlikely event that the author did not send a complete manuscript and there are missing pages, these will be noted. Also, if unauthorized copyright material had to be removed, a note will indicate the deletion.

**UMI**<sup>®</sup>

---

UMI Microform 3158683

Copyright 2005 by ProQuest Information and Learning Company.

All rights reserved. This microform edition is protected against unauthorized copying under Title 17, United States Code.

ProQuest Information and Learning Company  
300 North Zeeb Road  
P.O. Box 1346  
Ann Arbor, MI 48106-1346

This dissertation has been examined and approved.



---

Dissertation Director, Dr. Dale P. Barkey

Professor of Chemical Engineering  
University of New Hampshire



---

Dr. Palligarnai T. Vasudevan

Professor of Chemical Engineering  
University of New Hampshire



---

Dr. Nivedita Gupta

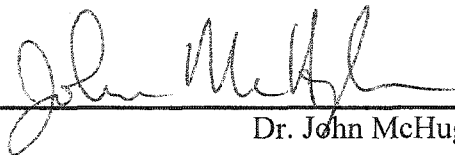
Assistant Professor of Chemical Engineering  
University of New Hampshire



---

Dr. Roy P. Planalp

Associate Professor of Inorganic Chemistry  
University of New Hampshire



---

Dr. John McHugh

Associate Professor of Mechanical Engineering  
University of New Hampshire

November 15, 2004

Date

## ACKNOWLEDGEMENTS

I would like to take this opportunity to express my sincere gratitude and deep appreciation to my advisor, Dr. Dale P. Barkey, for his invaluable insight, timely advice, and continual guidance. His scientific foresight and excellent knowledge have been crucial to the accomplishment of this work. I consider myself privileged for having had the opportunity to conduct research in the field of electrochemical deposition under his guidance.

I am grateful to Dr. Stephen ST. Fan for his continuous financial support and his encouragement and kindness during my PhD program studies. I also would like to thank Dr. Palligarnai T. Vasudevan, Dr. Gupta, Dr. Roy P. Planalp, and Dr. John McHugh for their assistance and valuable comments on the dissertation and for serving as my committee members.

Special thanks go to Dr. Zhenqiu Liu for true friendship and his great help in all aspects of my life. I enjoyed the time we spent together, which give me a pleasant and memorable time in my graduate study.

Finally, I wish to thank deeply my wife, Meizhen Wang, my son, Yilun Zhang and my parents and parents-in-law for their understanding and love. Their support, encouragement and love led me to move forward and made my dreams come true. I would like to dedicate the dissertation to them.

# TABLE OF CONTENTS

ACKNOWLEDGEMENTS.....	iii
LIST OF TABLES.....	vii
LIST OF FIGURES .....	viii
ABSTRACT.....	xiii
CHAPTER 1 INTRODUCTION.....	1
CHAPTER 2 LITERATURE REVIEW.....	4
2.1 Electrodeposition of Tin and Tin-silver Alloy.....	4
2.1.1 Plating Baths for Tin and Tin-silver Alloy Deposition.....	4
2.1.2 Electrodeposition of Tin.....	5
2.1.3 Electrodeposition of Tin-Silver Alloy.....	8
2.2 Effects of Additives on Tin Electrodeposition.....	10
2.3 Nucleation Studies of Tin Electrodeposition.....	15
2.4 Morphology Study of Tin Electrodeposition at Initial Stages.....	17
2.5 Theory of Nucleation and Growth during Initial Stages of Electrodeposition .	18
2.5.1 Multiple Nucleation with Mass Transfer Control.....	19
2.5.2 Critical Gibbs Free Energy and Critical Nucleus Size.....	26

CHAPTER 3	EXPERIMENTAL METHODS .....	30
3.1	Nucleation and Growth Kinetics of Tin and Tin-Silver Electrodeposition .....	30
3.1.1	Experiment setup.....	30
3.1.2	Cyclic voltammetry.....	32
3.1.3	Potentiostatic Current Transient Measurement.....	34
3.2	Morphology Studies of Tin and Tin-Silver Electrodeposition .....	35
3.2.1	Atomic Force Microscopy.....	35
3.2.2	AFM Experiment setup.....	36
3.2.3	SEM Imaging .....	37
3.3	Experimental Materials and Preparation.....	39
3.3.1	Polishing System.....	39
3.3.2	Single-crystal copper disk Substrate Preparation.....	40
3.3.3	Preparation of Bright Polycrystalline Copper Substrate and Polycrystalline Nickel Substrate .....	42
3.3.4	Solution Preparation.....	45
3.3.5	Cleaning of Electrochemical Cell .....	46
CHAPTER 4	NUCLEATION AND GROWTH KINETICS .....	47
4.1	RESULTS .....	48
4.1.1	Cyclic Voltammetry .....	48
4.1.2	Diffusion Coefficient Measurement.....	57
4.1.3	Potential Step Measurement (Chronoamperometry).....	60
4.1.3.1	Tin Electrodeposition in 0.02M SnSO <sub>4</sub> /1.0M H <sub>2</sub> SO <sub>4</sub> Solution.....	61

4.1.3.2	Tin Electrodeposition in 0.02M SnSO <sub>4</sub> / 1.0M H <sub>2</sub> SO <sub>4</sub> / 0.02MTu Solution.....	72
4.1.3.3	Tin Electrodeposition in 0.02M SnSO <sub>4</sub> /1.0M H <sub>2</sub> SO <sub>4</sub> /0.02M Tu / 2mM AgNO <sub>3</sub> Solution.....	75
4.1.3.4	Tin Electrodeposition from 0.02SnMS/1.0M MSA Solution....	84
4.2	Discussion.....	88
4.2.1	Effects of Thiourea on Tin Nucleation and Growth Kinetics .....	88
4.2.2	Effects of Thiourea-Silver Complex on Tin Nucleation and Growth Kinetics.....	91
4.2.3	Effects of Substrate on Nucleation and Growth Kinetics of Tin and Tin- Silver Alloy .....	94
4.2.4	Effects of Electrolyte Anion on Nucleation and Growth Kinetics of Tin Electrodeposition.....	95
CHAPTER 5	MORPHOLOGY OF TIN AND TIN-SILVER ALLOY .....	98
5.1	Effect of Deposition Potential on Tin Deposit Morphology.....	99
5.2	Effect of Additives on Deposit Morphology .....	105
5.3	Effect of Electrolyte Anion on Tin Deposit Morphology .....	110
CHAPTER 6	CONCLUSIONS .....	112
	REERENCE.....	116
	NOMENCLATURE.....	123



## LIST OF TABLES

Table 2-1	Expressions resulting from the analysis of the current transient maximum values for instantaneous and progressive nucleation.....	24
Table 3-1	Chemical Reagents .....	46
Table 4-1	The cathodic peak current and current function in sulfuric acid solution .....	49
Table 4-2	The apparent diffusion coefficient of Sn <sup>2+</sup> in different electrolyte solutions	58
Table 4-3	Parameters extracted from the current transients for tin electrodeposition on single crystal and polycrystalline copper substrates.....	64
Table 4-4	Nucleation parameters resulting from Scharifker and Mostany's model for tin electrodeposition on single crystal and polycrystalline copper substrates. .	64
Table 4-5	Critical Gibbs free energy of 3D nucleation and critical nucleus size for electrodeposition of tin on single crystal and polycrystalline copper substrates .....	70
Table 4-6	Parameters extracted from the current transients for tin electrodeposition on single crystal and polycrystalline copper, polycrystalline nickel substrates, from 0.02M SnSO <sub>4</sub> /1.0M H <sub>2</sub> SO <sub>4</sub> /0.02M Tu solution.....	73
Table 4-7	Parameters extracted from the current transients for tin electrodeposition on single crystal, polycrystalline copper, and polycrystalline nickel substrates, in 0.02M SnSO <sub>4</sub> /1.0M H <sub>2</sub> SO <sub>4</sub> /0.02M Tu /2mM AgNO <sub>3</sub> solution. ....	77
Table 4-8	Nucleation parameters resulting from SM model for tin electrodeposition on single crystal, polycrystalline copper, and polycrystalline nickel substrates, in 0.02M SnSO <sub>4</sub> /1.0M H <sub>2</sub> SO <sub>4</sub> /0.02M Tu /2mM AgNO <sub>3</sub> solution.....	77
Table 4-9	Critical Gibbs free energy of 3D nucleation and critical nucleus size for the electrodeposition of tin on single crystal and polycrystalline copper, from 0.02M SnSO <sub>4</sub> /1.0M H <sub>2</sub> SO <sub>4</sub> /0.02M Tu /2mM AgNO <sub>3</sub> solution. ....	82
Table 4-10	Parameters extracted from the current transients for tin electrodeposition on single crystal copper substrates, from 0.02M SnMS /1.0M MSA solution..	85
Table 4-11	Nucleation parameters resulting from Scharifker and Mostany's model for tin electrodeposition on single crystal copper substrates, from 0.02M SnMS /1.0M MSA solution.....	85
Table 4-12	Critical Gibbs free energy of 3D nucleation and critical nucleus size for electrodeposition of tin on single crystal copper substrates .....	87
Table 5-1	Calculated and measured nucleus density deposited from various tin electrolyte solutions.....	101

## LIST OF FIGURES

Figure 2-1	Shift of the standard potential for silver by complexation with thiourea, taken from Jordan. ....	10
Figure 2-2	Schematic plan view of hemispherical nuclei randomly distributed on the electrode surface. ....	22
Figure 2-3	Schematic of the growth of diffusion zones around growing nuclei and their eventual overlap on an electrode surface. ....	22
Figure 3.1	Experimental setup of the electrolysis cell.....	31
Figure 3.2	Control system of the electrolysis cell.....	32
Figure 3.3	Experimental settings for cyclic voltammogram measurements.....	33
Figure 3.4	Experimental settings for potential step measurement.....	34
Figure 3.5	Schematic principal of AFM measurements .....	36
Figure 3.6	AFM experimental setup.....	38
Figure 3.7	Polishing system.....	39
Figure 3.8	Schematic diagram of fluid flow on the RDE .....	43
Figure 3.9	Experimental setup for electrodeposition of bright polycrystalline copper and polycrystalline nickel on the platinum rotating disc electrode.....	44
Figure 4.1	Cyclic voltammograms of tin electrodeposition on single crystal copper in: (a) 0.02M SnSO <sub>4</sub> /1.0M H <sub>2</sub> SO <sub>4</sub> , (b) 0.02M SnSO <sub>4</sub> /1.0M H <sub>2</sub> SO <sub>4</sub> /0.02M Tu, (c) 0.02M SnSO <sub>4</sub> /1.0M H <sub>2</sub> SO <sub>4</sub> /0.02M Tu /2mM AgNO <sub>3</sub> . All at a sweep rate of 40 mV/s. ....	51
Figure 4.2	The fifth and tenth cyclic voltammograms of tin electrodeposition on single crystal copper in 0.02M SnSO <sub>4</sub> /1.0M H <sub>2</sub> SO <sub>4</sub> solution. The scan rate: (a) 40, (b) 80 mV/s.....	51
Figure 4.3	The fifth and tenth cyclic voltammograms of tin electrodeposition on single crystal copper in 0.02M SnSO <sub>4</sub> /1.0M H <sub>2</sub> SO <sub>4</sub> /0.02M Tu solution. The scan rate: (a) 40 mV/s, (b) 80 mV/s.....	52
Figure 4.4	The fifth and tenth cyclic voltammograms of tin electrodeposition on single crystal copper in 0.02M SnSO <sub>4</sub> /1.0M H <sub>2</sub> SO <sub>4</sub> /0.02M Tu /2mM AgNO <sub>3</sub> solution. The scan rate: (a) 40 mV/s, (b) 80 mV/s. ....	52
Figure 4.5	Cyclic voltammograms of tin electrodeposition on single crystal copper in 0.02M SnSO <sub>4</sub> /1.0M H <sub>2</sub> SO <sub>4</sub> solution. The scan rate from 20 to 100 mV/s..	53

Figure 4.6	Cyclic voltammograms of tin electrodeposition on single crystal copper in 0.02M SnSO <sub>4</sub> /1.0M H <sub>2</sub> SO <sub>4</sub> /0.02M Tu solution. The scan rate from 20 to 100 mV/s. ....	53
Figure 4.7	Cyclic voltammograms of tin electrodeposition on single crystal copper in 0.02M SnSO <sub>4</sub> /1.0M H <sub>2</sub> SO <sub>4</sub> /0.02M Tu /2mM AgNO <sub>3</sub> solution. The scan rate from 20 to 100 mV/s.....	54
Figure 4.8	Cyclic voltammograms of tin electrodeposition on bright polycrystalline copper in (a) 0.02M SnSO <sub>4</sub> /1.0M H <sub>2</sub> SO <sub>4</sub> , (b) 0.02M SnSO <sub>4</sub> /1.0M H <sub>2</sub> SO <sub>4</sub> /0.02M Tu, (c) 0.02M SnSO <sub>4</sub> /1.0M H <sub>2</sub> SO <sub>4</sub> /0.02M Tu /2mM AgNO <sub>3</sub> . All at the sweep rate of 40 mV/s. ....	54
Figure 4.9	Cyclic voltammograms of tin electrodeposition on polycrystalline nickel in (a) 0.02M SnSO <sub>4</sub> /1.0M H <sub>2</sub> SO <sub>4</sub> , (b) 0.02M SnSO <sub>4</sub> /1.0M H <sub>2</sub> SO <sub>4</sub> /0.02M Tu, (c) 0.02M SnSO <sub>4</sub> /1.0M H <sub>2</sub> SO <sub>4</sub> /0.02M Tu /2mM AgNO <sub>3</sub> . All at the sweep rate of 40 mV/s. ....	55
Figure 4.10	Cyclic voltammograms in 0.02M SnSO <sub>4</sub> /1.0M H <sub>2</sub> SO <sub>4</sub> solution at scan rate of 40 mV/s. The working electrodes are (a) Single crystal copper, (b) polycrystalline copper, (c) polycrystalline nickel. ....	55
Figure 4.11	Cyclic voltammograms in 0.02M SnSO <sub>4</sub> /1.0M H <sub>2</sub> SO <sub>4</sub> /0.02M Tu /2mM AgNO <sub>3</sub> solution at scan rate of 40 mV/s. The working electrodes are (a) Single crystal copper, (b) polycrystalline copper, (c) polycrystalline nickel. ....	56
Figure 4.12	Cyclic voltammograms of tin electrodeposition on a single crystal copper in various solutions: (a) 0.02M SnMS /1.0M MSA, (b) 0.02M SnMS /1.0M MSA /0.02M Tu, (c) 0.02M SnMS /1.0M MSA /0.02M Tu /2mM AgMS. All at a scan rate of 40 mV/s. ....	56
Figure 4.13	Current transients for tin electrodeposition on single crystal copper in various solutions. (a) 0.02M SnSO <sub>4</sub> /1.0M H <sub>2</sub> SO <sub>4</sub> , (b) 0.02M SnSO <sub>4</sub> /1.0M H <sub>2</sub> SO <sub>4</sub> /0.02M Tu, (c) 0.02M SnSO <sub>4</sub> /1.0M H <sub>2</sub> SO <sub>4</sub> /0.02M Tu /2mM AgNO <sub>3</sub> . The potential was -580 mV.....	59
Figure 4.14	Cottrell plots for tin electrodeposition on single crystal copper in various solutions. (a) 0.02M SnSO <sub>4</sub> /1.0M H <sub>2</sub> SO <sub>4</sub> , (b) 0.02M SnSO <sub>4</sub> /1.0M H <sub>2</sub> SO <sub>4</sub> /0.02M Tu, (c) 0.02M SnSO <sub>4</sub> /1.0M H <sub>2</sub> SO <sub>4</sub> /0.02M Tu /2mM AgNO <sub>3</sub> .....	59
Figure 4.15	Randle-Sevcik plots for tin electrodeposition on single crystal copper in various solutions: (a) 0.02M SnSO <sub>4</sub> /1.0M H <sub>2</sub> SO <sub>4</sub> , (b) 0.02M SnSO <sub>4</sub> /1.0M H <sub>2</sub> SO <sub>4</sub> /0.02M Tu, (c) 0.02M SnSO <sub>4</sub> /1.0M H <sub>2</sub> SO <sub>4</sub> /0.02M Tu /2mM AgNO <sub>3</sub> . The scan rate from 20 to 100 mV/s .....	60
Figure 4.16	Current transients for tin electrodeposition on single crystal copper (Cu-S) substrate at the indicated final potentials in 0.02M SnSO <sub>4</sub> /1.0M H <sub>2</sub> SO <sub>4</sub> solution. The initial potential is -465mV.....	65
Figure 4.17	Current transients for tin electrodeposition on the polycrystalline copper..	65
Figure 4.18	Current transients for tin electrodeposition on the polycrystalline nickel...	66

Figure 4.19	Comparison of theoretical (SM line) and experimental (Exp line) current transients. Tin was electrodeposited on: (a) single crystal copper (Cu-S), (b) polycrystalline copper (Cu-P), at $-570\text{mV}$ .....	67
Figure 4.20	Dependence of the number density of active sites ( $N_0$ ) with overpotentials for tin electrodeposition on (a) single crystal copper (Cu-S), (b) polycrystalline copper (Cu-P), in $0.02\text{M SnSO}_4 / 1.0\text{M H}_2\text{SO}_4$ solution. ....	68
Figure 4.21	Nucleation rate as a function of $1/\eta^2$ for tin electrodeposition on (a) single crystal copper (Cu-S), (b) polycrystalline copper (Cu-P), in $0.02\text{M SnSO}_4 / 1.0\text{M H}_2\text{SO}_4$ solution. ....	71
Figure 4.22	Dependence of nucleation rate with overpotentials for tin electrodeposition on (a) single crystal copper (Cu-S), (b) polycrystalline copper (Cu-P), in $0.02\text{M SnSO}_4 / 1.0\text{M H}_2\text{SO}_4$ solution. ....	71
Figure 4.23	Current transients for tin electrodeposition on single crystal copper (Cu-S) in $0.02\text{M SnSO}_4 / 1.0\text{M H}_2\text{SO}_4 / 0.02\text{MTu}$ Solution at the indicated final potentials. The initial potential is $-465\text{mV}$ . ....	73
Figure 4.24	Current transients for tin electrodeposition on the polycrystalline copper substrate (Cu-P) in $0.02\text{M SnSO}_4 / 1.0\text{M H}_2\text{SO}_4 / 0.02\text{MTu}$ Solution at the indicated potentials. The initial potential is $-465\text{ mV}$ .....	74
Figure 4.25	Current transients for tin electrodeposition on the polycrystalline nickel substrate (Ni-P) in $0.02\text{M SnSO}_4 / 1.0\text{M H}_2\text{SO}_4 / 0.02\text{MTu}$ Solution at the indicated potentials. The initial potential is $-465\text{ mV}$ .....	74
Figure 4.26	Current transients for tin electrodeposition on single crystal copper (Cu-S) in $0.02\text{M SnSO}_4 / 1.0\text{M H}_2\text{SO}_4 / 0.02\text{M Tu} / 2\text{mM AgNO}_3$ solution at the indicated final potentials. The initial potential is $-420\text{ mV}$ . ....	78
Figure 4.27	Current transients for tin electrodeposition on polycrystalline copper (Cu-P) in $0.02\text{M SnSO}_4 / 1.0\text{M H}_2\text{SO}_4 / 0.02\text{M Tu} / 2\text{mM AgNO}_3$ solution at the indicated final potentials. The initial potential is $-420\text{ mV}$ . ....	78
Figure 4.28	Current transients for tin electrodeposition on polycrystalline Nickel (Ni-P) in $0.02\text{M SnSO}_4 / 1.0\text{M H}_2\text{SO}_4 / 0.02\text{M Tu} / 2\text{mM AgNO}_3$ solution at the indicated final potentials. The initial potential is $-420\text{ mV}$ . ....	79
Figure 4.29	Comparison of theoretical (SM line) and experimental (Exp line) transients for tin deposition: (a) single crystal copper (Cu-S), (b) polycrystalline copper (Cu-P), (c) polycrystalline nickel, at $-570\text{mV}$ , in tin solution with thiourea-silver. ....	80
Figure 4.30	Dependence of the number density of active sites with overpotentials for tin electrodeposition on: (a) single crystal copper (Cu-S), (b) polycrystalline copper (Cu-P), (c) polycrystalline nickel (Ni-P), in $0.02\text{M SnSO}_4 / 1.0\text{M H}_2\text{SO}_4 / 0.02\text{M Tu} / 2\text{mM AgNO}_3$ solution .....	81
Figure 4.31	Nucleation rate as a function of $1/\eta^2$ for tin electrodeposition on (a) single crystal copper (Cu-S), (b) polycrystalline copper (Cu-P), (c) polycrystalline nickel, in $0.02\text{M SnSO}_4 / 1.0\text{M H}_2\text{SO}_4 / 0.02\text{M Tu} / 2\text{mM AgNO}_3$ solution. .	83

Figure 4.32	Dependence of nucleation rate with overpotentials for tin electrodeposition on (a) single crystal copper (Cu-S), (b) polycrystalline copper (Cu-P), (c) polycrystalline nickel, in 0.02M SnSO <sub>4</sub> /1.0M H <sub>2</sub> SO <sub>4</sub> /0.02M Tu /2mM AgNO <sub>3</sub> solution. ....	83
Figure 4.33	Current transients for tin electrodeposition on single crystal copper (Cu-S) in 0.02M SnMS /1.0M MSA solution at the indicated final potentials. The initial potential is -450 mV. ....	86
Figure 4.34	Nucleation rate as a function of 1/η <sup>2</sup> for tin electrodeposition on single crystal copper (Cu-S), in 0.02M SnMS /1.0M MSA solution. ....	87
Figure 4.35	Dependence of nucleation rate with overpotentials for tin electrodeposition on single crystal copper (Cu-S), in 0.02M SnMS /1.0M MSA solution. ....	88
Figure 4.36	Current transients for tin electrodeposition on single crystal copper in acidic tin solutions containing: (a) Additive free, (b) thiourea, (c) thiourea-silver. 90	
Figure 4.37	Relative position of the standard potentials of the metals, which are possible partners for leadfree tin alloys. ....	91
Figure 4.38	Current transients for tin electrodeposition on various substrates in 0.02MSnSO <sub>4</sub> /1MH <sub>2</sub> SO <sub>4</sub> /0.02MTu / 2mM AgNO <sub>3</sub> , (a) single crystal Cu, (b) polycrystalline Cu, (c) polycrystalline Ni. ....	95
Figure 4.39	Current transients for tin electrodeposition on single crystal copper in solutions: (a) 0.02M SnSO <sub>4</sub> /1M H <sub>2</sub> SO <sub>4</sub> , (b) 0.02M SnMS /1M MSA, at -570 mV. ....	96
Figure 5.1	SEM micrograph of tin deposit obtained at -520 mV for 4 sec in 0.02MSnSO <sub>4</sub> / 1.0M H <sub>2</sub> SO <sub>4</sub> solution. ....	102
Figure 5.2	SEM micrograph of tin deposit obtained at -550 mV for 4 sec in 0.02MSnSO <sub>4</sub> / 1.0M H <sub>2</sub> SO <sub>4</sub> solution. ....	102
Figure 5.3	SEM micrograph of tin deposit obtained at -520 mV for 4 sec in 0.02MSnSO <sub>4</sub> / 1.0M H <sub>2</sub> SO <sub>4</sub> solution. ....	103
Figure 5.4	AFM images of tin deposits obtained at -530 mV for 4 sec in 0.02MSnSO <sub>4</sub> / 1.0M H <sub>2</sub> SO <sub>4</sub> solution. ....	103
Figure 5.5	AFM images of tin deposits obtained at -550 mV for 4 sec in 0.02MSnSO <sub>4</sub> / 1.0M H <sub>2</sub> SO <sub>4</sub> solution. ....	104
Figure 5.6	AFM images of tin deposits obtained at -570 mV for 3 sec in 0.02MSnSO <sub>4</sub> / 1.0M H <sub>2</sub> SO <sub>4</sub> solution. ....	104
Figure 5.7	SEM micrograph of tin deposit obtained at -550 mV for 8 sec in 0.02MSnSO <sub>4</sub> / 1.0M H <sub>2</sub> SO <sub>4</sub> / 0.02M Thiourea solution. ....	107
Figure 5.8	SEM micrograph of tin deposit obtained at -550 mV for 6 sec in 0.02MSnSO <sub>4</sub> / 1.0M H <sub>2</sub> SO <sub>4</sub> / 0.02M Thiourea / 2mM AgNO <sub>3</sub> solution. ....	107
Figure 5.9	AFM images of tin deposit obtained at -550 mV for 8 sec in 0.02MSnSO <sub>4</sub> / 1.0M H <sub>2</sub> SO <sub>4</sub> / 0.02M Thiourea solution. ....	108

Figure 5.10	AFM images of tin deposit obtained at $-550$ mV for 6 sec in $0.02\text{M SnSO}_4 / 1.0\text{M H}_2\text{SO}_4 / 0.02\text{M Thiourea} / 2\text{mM AgNO}_3$ solution. ....	108
Figure 5.11	AFM images of tin deposit obtained at $-550$ mV for 30 sec in $0.02\text{M SnSO}_4 / 1.0\text{M H}_2\text{SO}_4 / 0.02\text{M Thiourea} / 2\text{mM AgNO}_3$ solution. ....	109
Figure 5.12	AFM images of tin deposit obtained at $-550$ mV for 300 sec in $0.02\text{M SnSO}_4 / 1.0\text{M H}_2\text{SO}_4 / 0.02\text{M Thiourea} / 2\text{mM AgNO}_3$ solution....	109
Figure 5.13	SEM micrograph of tin deposit obtained at $-530$ mV for 8 sec in $0.02\text{M SnMS} / 1.0\text{M MSA} / 0.02\text{M Thiourea}$ solution. ....	110
Figure 5.14	SEM micrograph of tin deposit obtained at $-530$ mV for 8 sec in $0.02\text{M SnMS} / 1.0\text{M MSA} / 0.02\text{M Thiourea} / 2\text{mM AgNO}_3$ solution....	111

## **ABSTRACT**

# **NUCLEATION AND GROWTH KINETICS OF TIN AND TIN-SILVER ALLOY DURING INITIAL STAGES OF ELECTRODEPOSITION**

By

Zhongqin Zhang

University of New Hampshire, December, 2004

Electrodeposition has played an essential role in electronics packaging because it gives superior thickness control for chip interconnects. Pure tin, tin-silver and tin-silver-based solders have been identified as leading candidates for lead-free solders due to the desirable melting point, good creep resistance and thermo-mechanical behavior.

The initial stage of electrodeposition, or the formation of small clusters of atoms (nuclei), is significant in the overall electrodeposition kinetics, as well as the appearance, structure, and properties of the resulting coatings. In this work, nucleation and growth kinetics of tin and tin-silver electrodeposition on copper and nickel substrates were investigated by electrochemical methods and surface analysis techniques (SEM and AFM). The nucleation rate, number density of active sites, critical nucleus size and free energy of critical nucleus formation were extracted under various electrolyte solutions.

Based on chronoamperometric studies, in acid tin solution without additives, tin electrodeposition is instantaneous nucleation with three-dimensional diffusion controlled

growth. Addition of thiourea to the solution changes the nucleation process from instantaneous to progressive, which was confirmed by SEM and AFM analysis. In the acid tin solution containing thiourea-silver, the process of nucleation is unclassified. In all cases, the number density of active sites increases exponentially as the deposition potential changes to more negative values, and it is the highest in the solution with thiourea-silver.

According to classical and atomistic theories, in all cases, tin electrodeposition proceeds with three-dimensional phase formation and growth. The number of atoms forming the critical nucleus ( $N_{crit}$ ) consists of 0-2 atoms. The critical Gibbs free energy ( $\Delta G_{crit}$ ) follows the sequence  $Cu-S > Ni-P > Cu-P$ , which is consistent with the number density of active sites on the substrate surface.

The number density of nuclei in the AFM images was measured by AFM. In comparison with calculated nucleus densities, the measured values are much higher. At –550 mV, the measured density is about 2 times as great as the calculated value in acid tin solution without additive. In the presence of thiourea-silver, the measured density is about 6 times as great as the calculated one.



# CHAPTER 1

## INTRODUCTION

Electrochemical technology has played an essential role in the semiconductor industry, including applications in storage, interconnection and packaging. As electronic components continue to evolve towards higher performance, higher density and miniaturization, electrodeposition is becoming important in electronics packaging. It is presently used to deposit solder bumps for flip-chip packaging because it gives superior thickness control and can produce solder bumps as small as a few tens of microns for chip interconnects on a two-hundred-micron pitch.

Chip-package interconnections currently used in the semiconductor industry include wire bonding, tape automated bonding (TAB), and flip-chip solder connection. Unlike interconnection through wire bonding, the flip-chip process uses solder bumps. It is an array configuration in which the entire surface of the chip can be covered with bumps for the highest possible number of connections. This technology offers superior electrical performance due to the shorter electrical connections between the chip and substrate, which results in the smallest possible package size.

Solders currently used in the flip-chip and wafer-level packaging are based on tin-lead alloy, primarily due to its low cost and unique characteristics such as low melting point, high strength, ductility, fatigue resistance, thermal cycling, electrical conductivity and joint integrity. It offers an advantageous low melting range, making it ideal for

joining most metals without damage to heat-sensitive parts. However, medical studies have shown that lead is a heavy-metal toxin that can damage the kidneys, liver, blood, and central nervous system. Less than one percent per year of global lead consumption is used in solder alloys for electronic products, but electronic products make up an increasing fraction of landfills. The issue of lead leaching from landfills into water tables is a potential source of long-term contamination of soil and ground water. Hence, the use of lead in electronic products is an increasingly visible environmental and political concern. The harmful environmental effects of lead have forced solder manufacturers and users to look for alternatives.

Research and development efforts in lead-free solder are focused on the study of alloys that provide physical, mechanical, thermal, and electrical properties similar to those of tin-lead eutectic solder. Among alloys that can be electrodeposited, tin-silver (Sn-Ag) alloy is considered one of the most promising alternatives to lead-free solders. The 96.5Sn-3.5Ag eutectic alloy offers superior strength compared with other solders. It also provides good mechanical and thermal properties.

As an interconnection technology for electronics packaging, one fundamental aspect of electrodeposition processes is the initial stage of phase formation. In almost all cases, the initial stage of formation of small clusters of atoms (nuclei) is significant for determination of the overall electrodeposition kinetics, as well as the appearance, structure, and properties of the finished deposit. This stage is normally associated with a two- or three- dimensional growth process where the number of nuclei formed on the electrode surface is strongly dependent on overpotential.

The electrodeposition of tin and tin-silver alloy on copper and nickel substrates is a matter of great technological importance since the process has been used to form interconnects in the semiconductor industry, and nickel is used as a diffusion barrier layer to exclude copper from the solder. The nucleation and growth kinetics of tin and tin-silver alloy electrodeposition must be understood and controlled to produce high quality lead-free solders. While the initial stage of tin and tin-silver alloy electrodeposition on copper and nickel substrates has a significant impact on the character of the subsequently grown film. Little information is available on the initial stages of tin electrodeposition, and still less on tin-silver alloy electrodeposition.

The purpose of this work was to investigate nucleation and growth kinetics of tin and tin-silver alloy electrodeposition on single crystal copper, polycrystalline copper and polycrystalline nickel substrates. The electrolyte systems were acid tin sulfate or acid tin methanesulfonate bath with and without thiourea or thiourea and silver ions. Electrochemical methods and atomic force microscopy (AFM) were used to examine the nucleation mechanism and nucleation rate of tin and tin-silver during the initial stage of electrodeposition.

## CHAPTER 2

### LITERATURE REVIEW

#### 2.1 Electrodeposition of Tin and Tin-silver Alloy

##### 2.1.1 Plating Baths for Tin and Tin-silver Alloy Deposition

Tin is the principal component of almost all solders used in the assembly of electronic parts <sup>[1]</sup> because it has a low melting point (232°C), high ductility and excellent corrosion resistance. It readily alloys with many metals to produce low-melting eutectics. Molten tin wets and spreads easily on a wide range of substrates including copper, nickel, copper-based alloys, and nickel-based alloys.

Two types of tin electrolyte solution are used in tin plating: alkaline and acid. Acid baths have become the choice of the electronics industry because of their high rates of deposition and high cathode efficiency <sup>[2]</sup>. All of the acid baths contain tin in the divalent form ( $\text{Sn}^{2+}$ ). The high solubility of the divalent tin salts in acid allows the formulation of concentrated electrolytes to achieve high current densities. The most commonly used acid baths are stannous sulfate/sulfuric acid, and tin fluoborate/fluoboric acid. Recently, the methane sulfonate bath (tin methanesulfonate /methanesulfonic acid) has been accepted and is quickly replacing the fluoborate bath <sup>[3, 4]</sup> which is highly corrosive and hazardous. The chelating ability of the fluoborate ion and the presence of fluoride ions in the effluent require complex waste treatment procedures <sup>[2]</sup>.

Proell <sup>[5, 6]</sup> was the first to propose the use of alkane sulfonic acid as an electroplating bath. He found that alkane sulfonates/alkane sulfonic acids with one to five carbons in the alkyl group were stable under wide ranges of temperature, and did not undergo hydrolysis. Methane sulfonic acid (MSA) is a strong, non-oxidizing organic acid that is completely miscible with water. MSA is about twice as strong as HCl and about one half as strong as the first ionization of sulfuric acid <sup>[7]</sup>. Proell found that it was possible to plate many metals from alkane sulfonate baths, including cadmium, lead, nickel, silver and zinc. Many patents based on this system have been granted <sup>[8-15]</sup> since the late 1980's.

### 2.1.2 Electrodeposition of Tin

In acid solution, the stannous ion ( $\text{Sn}^{2+}$ ) is stable, but is oxidized by dissolved oxygen to  $\text{Sn}^{4+}$  resulting in precipitation of  $\text{SnO}_2$ . To minimize the oxidation of the divalent tin antioxidants may be added to the bath. The mechanisms <sup>[16]</sup> of inhibition for  $\text{Sn}^{4+}$  formation by antioxidants can be: (1) the additives form stable complexes with  $\text{Sn}^{2+}$ , (2) the additives reduce oxygen solubility in the plating solution, therefore reducing the rate of oxidation, (3) the additives tie up the soluble oxygen in the solution and lower the oxidation rate <sup>[17]</sup>. Alternatively, a piece of tin sponge is placed in the plating solution. Tin sponge drives the consumption of  $\text{Sn}^{4+}$  by



In an activation-controlled process in which the rate of reaction is controlled solely by the rate of the electrochemical charge transfer, the rate of metal deposition is related to the applied overpotential by the Butler–Volmer equation.

$$i = i_0 \left[ \exp\left(\frac{\alpha_a zF}{RT} \eta\right) - \exp\left(-\frac{\alpha_c zF}{RT} \eta\right) \right] \quad (2.2)$$

where  $i$  and  $i_0$  are current density and exchange current density ( $\text{mA}/\text{cm}^2$ ),  $\alpha_a$  and  $\alpha_c$  the dimensionless anodic and cathodic transfer coefficients,  $\eta$  the overpotential (mV),  $z$  the equivalents transferred per mole of metal deposited, and  $RT/F$  the thermal voltage.

A negative overpotential and negative current correspond to reduction and deposition. At large overpotentials, the Butler-Volmer can be simplified to the Tafel form.

$$\ln(-i) = -\frac{\alpha_c zF}{RT} \eta + \ln(i_0) \quad (2.3)$$

In this limit, a plot of  $\ln(i)$  vs  $\eta$  is linear. The parameters  $i_0$ ,  $\alpha_a$  and  $\alpha_c$  can be obtained from plots of the experimental current density vs the applied overpotential.

Tzeng<sup>[18]</sup> and Barry et al<sup>[19]</sup> investigated the mechanism of tin (II) reduction from sulfate/sulfuric acid solution. In Tzeng's study, the transfer coefficient ( $\alpha$ ) of anode and cathode were 1.13 and 0.56 in 0.01M  $\text{SnSO}_4$  / 10% (v/v)  $\text{H}_2\text{SO}_4$  solution. Barry reported an exchange current density of  $2.6 \times 10^{-1} \text{ mA}/\text{cm}^2$  and anodic and cathodic transfer coefficients of 1.31 and 0.68, respectively, in 0.14M  $\text{SnSO}_4$  / 2M  $\text{H}_2\text{SO}_4$  solution. The values of  $(\alpha_a + \alpha_c)$  were about 1.7 or 1.99, approaching 2. Therefore, the electrodeposition of tin is a two-electron transfer reaction in acid sulfate solution.



Meibuhr et al<sup>[20]</sup> found that  $\text{Sn}^{2+}$  reduction in acid system is a first order reaction. Gorodetski et al<sup>[21]</sup> also studied the mechanism and the kinetics of  $\text{Sn}^{2+}$  electroreduction at a tin amalgam electrode. The electrode reaction was shown to be reversible. They

proposed a two-step electron transfer mechanism for tin (II) electro-reduction in acidic solution:



The first reduction step is much slower than the second. So the reduction of  $\text{Sn}^{2+}$  to  $\text{Sn}^+$  is the rate-limiting step, and it determines the rate of the overall process described by equation (2.4). This mechanism was verified by Chen et al <sup>[3]</sup>, who studied the kinetics of tin (II) reduction in 0.0025M  $\text{Sn}(\text{CH}_3\text{SO}_3)_2$  / 1M  $\text{CH}_3\text{SO}_3\text{H}$  (MSA) solution at a rotating disk electrode (RDE). They reported an exchange current density of  $3.98 \times 10^{-2} \text{ mA/cm}^2$ , and confirmed that tin (II) reduction was first order. The value of exchange current density in MSA system is about 7 times smaller than that in sulfuric acid. The slower cathodic reaction rate in MSA system is probably due to the fact that activation energies of charge transfer in an organic acid are usually higher<sup>[22]</sup> than in aqueous solution.

Tin is electrodeposited with little activation polarization from acid stannous sulfate solution in the absence of additives. The deposits obtained under such conditions are usually non-adherent, coarse, and porous, with a tendency to form dendrites <sup>[23]</sup>. The presence of certain organic additives results in a substantial increase in polarization even at low current densities and a large improvement in the quality of the tin deposits in terms of adherence, decreased grain size, and freedom from dendrites. Such deposits may be specularly smooth or "bright". However, it is known that co-deposition of organics may adversely influence the solderability. In addition whisker formation results from the presence of compressive internal stress and organic brighteners after the deposit is formed <sup>[24-30]</sup>. Bright tin finishes are therefore prohibited on microelectronics parts.

Tin electrodeposits, especially if they contain Sn-Cu intermetallic compounds or incorporated organics may spontaneously form microscopic single-crystal projections in air, referred to as whiskers. Whiskers may appear months after the plated parts are put in service. Several remedies have been proposed to overcome the problem of whisker formation: alloying with a small percentage of other metal or depositing a nickel undercoat beneath the tin coating. According to Kuhl <sup>[31]</sup> et al, a nickel barrier layer applied over copper can eliminate tin whisker formation. A 4 to 5  $\mu\text{m}$  electroplated nickel layer on the copper substrate provided a barrier to diffusion of copper and growth of Sn-Cu intermetallic compounds so that whisker free tin electrodeposits were obtained.

### **2.1.3 Electrodeposition of Tin-Silver Alloy**

Tin-silver alloys are considered to be suitable for use as lead-free solder from the viewpoints of mechanical, soldering, creep and thermal cyclic fatigue characteristics <sup>[32-34]</sup>. Artaki et al <sup>[35]</sup> examined the feasibility of printed circuit board assembly with Sn-Ag solders, and concluded that the performance of Sn-Ag solder was adequate for surface mount applications. Yang et al <sup>[36]</sup> studied the effects of soldering temperature, reflow time, and cooling rate on the microstructure and mechanical properties of eutectic Sn-Ag solder joints. As a lead-free alternative, eutectic Sn-Ag solder offers enhanced mechanical properties and good wettability on Cu and Cu alloys. They also explored the influence of microstructure on the shear strength, ductility, and creep resistance of the joint, and found that low soldering temperatures, fast cooling rates, and short reflow times were beneficial for the solder joint.



At present, there are few reports on the electrodeposition of tin-silver alloy from acid plating solutions. One of the major problems in the acid tin-silver system is the large difference in the reduction potentials between tin and silver. In an uncomplexed electrolyte silver is reduced in the solution by divalent tin.



This reaction results in formation of finely divided black particles of metallic silver. Thus, it is desirable to bring the silver reduction potential as close as possible to the potential of tin by addition of suitable complexing agents. Silver forms complexes readily with some anionic species such as  $\text{CN}^-$ ,  $\text{SCN}^-$ ,  $\text{S}_2\text{O}_3^{2-}$ , and  $\text{S}_2\text{O}_8^{2-}$ , which are limited to alkaline media. Thiourea is a strong ligand for silver in acid solution. The shift of the standard potential in relation to the concentration of thiourea is shown in Figure 2.1, taken from Jordan<sup>[34]</sup>. Although it is seen that the potential of silver complex cannot reach or fall below the standard potential of tin, tin-silver alloys can be obtained by electrodeposition if a sufficient concentration of thiourea is used.

Tin-silver alloy has been electrodeposited from alkaline baths, such as silver cyanide/tin pyrophosphate<sup>[37-39]</sup> or silver iodide/tin pyrophosphate baths<sup>[32]</sup>. Recently, a cyanide free bath for tin-silver alloy plating composed of acid sulfate/sulfuric acid solution<sup>[40]</sup> with thiourea was developed. The electrodeposition of a wide composition range of alloys was successfully achieved with this solution.

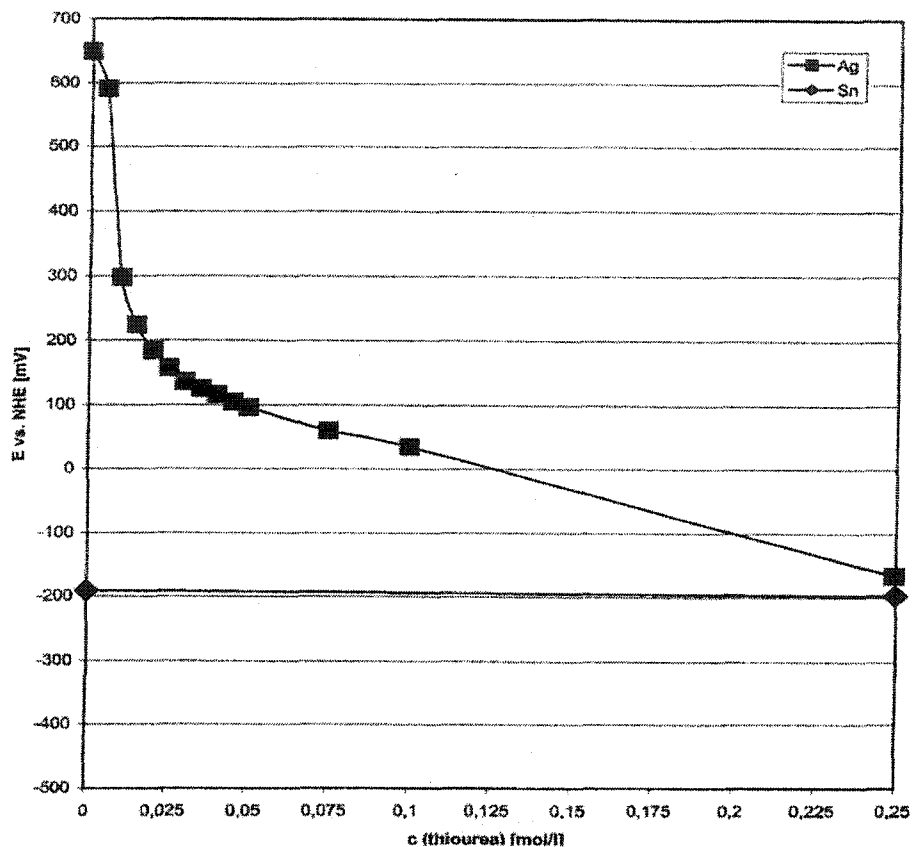


Figure 2.1 Shift of the standard potential for silver by complexation with thiourea, taken from Jordan<sup>[34]</sup>.

## 2.2 Effects of Additives on Tin Electrodeposition

Regardless of the type of electrolyte employed, different additives are used to produce satisfactory surface finishes: matte, semi-bright, and full bright. According to their functions, additives are classified as levelers, brighteners, grain refiners, dendrite inhibitors, or wetting agents. The use of additives in aqueous electroplating solutions is extremely important, primarily due to the effects on nucleation, cluster growth and deposit structure. The potential benefits of additives include brightening the deposit, reducing grain size, reducing the tendency to form dendrites, promoting leveling, and improving mechanical and physical properties. The quantity of additive agents is

typically very small (~100 ppm) and their action is usually specific for a particular bath<sup>[80]</sup>. Adsorption on the metal surface is believed to be necessary for most additives to influence the electrodeposition process. To explain the behavior of additives, Oniciu et al<sup>[41]</sup> and Frankin<sup>[42]</sup> suggested some mechanisms, such as: surface modification by blocking and surface complex formation including adsorption and ion bridging.

Organic additives are an important component of plating baths for the deposition of tin with properties suitable for electronic and other practical applications. Without additives, the tin deposits are rough, porous, and sometimes dendritic. Addition of certain organic additives to the acidic plating baths improves the quality of the deposits. The effects of various additives on tin electrodeposition from acidic solution have been investigated by many authors<sup>[18, 43-56]</sup>. Meibuhr et al<sup>[43]</sup> studied the kinetics of tin deposition from a sulfate solution containing various non-ionic organic additives (such as Triton, Pluronic, Polyglycol etc). Many of these additives cause a significant increase in the cathodic polarization and a pronounced improvement in the quality of the deposits.

In the absence of additives, the activation polarization is very small. As a result, transport of tin ion to the deposit is the rate-limiting step, and the concentration polarization is predominant in steady state polarization measurements. Tafel linearity was not observed in this case. In the presence of additives, however, the Tafel linearity was observed, indicating that the rate-determining step is probably charge transfer through a layer of adsorbed organic molecules. Meibuhr et al<sup>[43]</sup> stated that the film of adsorbed additives was in a steady state of adsorption, desorption, and occlusion on the solid cathodes, and some of the adsorbed organic molecules were occluded into the tin deposits during the deposition process.

Nagaraj <sup>[44]</sup> investigated bright tin deposition from acid sulfate baths containing some organic surface-active agents. High molecular weight organic compounds (such as alkyl-aryl polyether alcohols) were found to be good brighteners. The organic layer inhibits growth of nuclei, producing a high rate of new nucleus formation. Therefore, bright, fine-grained uniform deposits are obtained. These additives also increase the hydrogen overpotential, producing higher current efficiency at higher current densities.

Aragon et al <sup>[45]</sup> studied the effects of a polyethoxylated additive, Triton X-102 on the electrodeposition of tin. Below the critical micelle concentration (CMC, about 0.2-0.3 g/L), the additive has little effect on the quality of the tin deposits. When the additive concentration is higher than the CMC, high molecular weight micelles are formed. These micelles form a thick layer, anchored on the sites of highest energy on the electrode surface. As nucleation progresses, the anchoring micelles shift to newly formed sites of high energy, forcing continuous formation of new active nuclei. Thus, the deposit is constituted of many small crystals rather than a few large ones.

Kaneko <sup>[48, 49]</sup> found that addition of N, N-bis(polyoxy ethylene) octadecylamines and aromatic carbonyl compounds (benzalacetone, benzophenone) in sulfate solution increased cathodic polarization, and produced smooth, compact and uniform deposits over the whole surface. These kinds of additives are adsorbed on the electrode and inhibit the electrochemical reduction of  $\text{Sn}^{2+}$  ions. Rehim <sup>[50]</sup> investigated the effects of additives on cathodic polarization for tin electrodeposition from acidic sulfate solution with sodium gluconate. It was found that the presence of gluconate ions significantly increased the cathodic polarization by formation of tin complexes. The complex ions cannot be reduced as easily as the free  $\text{Sn}^{2+}$  ions. In addition to the complexation process, the gluconate ions

may be adsorbed on the electrode surface and block active sites for tin deposition. This phenomenon increases the overpotential for the reaction by decreasing the sites available for discharge of metal ions <sup>[47]</sup>.

Tzeng <sup>[18, 51]</sup> studied the kinetics of tin electrodeposition from sulfate electrolytes with various additives (formaldehyde, propionaldehyde, benzaldehyde, acetophenone and 4-methyl-2-pentanone). In his study, the polarization behavior and kinetic parameters of stannous sulfate were investigated by Tafel polarization and Cyclic Voltammometry. Tzeng found that the Tafel slope and anodic and cathodic transfer coefficients in the various plating solutions were approximately equal. Based on this result, he concluded that the reaction mechanism remained the same whether the solution contains an additive or not. Carbonyl compounds containing a phenyl group may act as a grain refiner.

Zhang et al <sup>[52, 53]</sup> studied the electrodeposition of tin in methanesulfonic acid (MSA) with two non-volatile additives. Additive A is a wetting agent and Additive B a grain refiner. It was found that during electrodeposition, only the grain refiner, Additive B was consumed, and semi-bright tin deposits were obtained with large, well-polygonized grains and very low organic content. Both factors are believed to reduce the internal stress, which is the root cause of whisker formation. Tin whiskers develop under compressive internal stress that represents a thermodynamically unstable condition. If the grain size of the tin coating is in the few micron range, the driving force for creating internal stress is eliminated, and the probability of whisker formation is greatly reduced.

Kakeshita et al <sup>[57]</sup> reached a similar conclusion. Kakeshita has shown that tin deposits having grain sites in the range of 0.2 to 0.8  $\mu\text{m}$  formed whiskers easily, whereas no whiskers were found for tin deposits having grain size in the range of 1 to 8  $\mu\text{m}$ .

Moreover, fine-grained deposits have a higher rate of forming intermetallic compounds. Finer grained deposits have larger grain boundary, resulting in faster diffusion. As a result, there will be more intermetallic compounds formed at a given time for a fine-grained (e.g.  $< 0.1 \mu\text{m}$ ) deposit compared to a large-grained (e. g.  $> 2 \mu\text{m}$ ) deposit. Intermetallics increase the internal stress, increasing the probability of whisker formation.

The concentration of organic additives in the tin deposits also plays a key role in the formation of whiskers. High organic inclusion has been shown to significantly accelerate whisker formation <sup>[25, 26]</sup>. It is also thought to increase the internal stress of the plated tin layer. Additionally, high organic inclusions in tin coatings have other detrimental effects. When the deposit is soldered, the co-deposited additives are volatilized. Dewetting is thus inevitable if high concentrations of organic additives are co-deposited in the tin coating during the deposition process.

Zhang et al <sup>[54]</sup> also studied the adsorption behavior and the effect of organic additives on tin electrodeposition utilizing electrochemical and surface enhanced Raman spectroscopy techniques in MSA baths. Triton X-100 is adsorbed on the electrode surface over a wide potential range. A hydrophobic head group serves to anchor the molecule to the metal surface. At negative potential, around  $-500\text{mV}$ , the molecule turns its long hydrophilic tail to the surface, increasing the effective surface coverage. The authors also showed that the co-adsorption of Triton X-100 and phenolphthalein modified the grain size and the deposit structure to a uniform and smooth surface.

## 2.3 Nucleation Studies of Tin Electrodeposition

A number of investigations of tin electrodeposition from acid solution with or without additives have addressed cathodic polarization and the deposited film structure of the advanced stages. However, little information on the initial stages of electrodeposition of tin is available. The nucleation and growth kinetics of tin electrodeposition with and without additives have only been examined by a few authors [19, 58-59]. Gomez [58] et al studied tin electrodeposition on vitreous carbon from sulfuric acid solution without additives. It was found that the plot of current density  $i$  vs  $t^{1/2}$  for the increasing part of  $i$  vs  $t$  transient is a straight line. The analysis of the current transients reveals that the tin electrodeposition process is an instantaneous nucleation with three-dimensional diffusion controlled growth.

Guaus et al [59] investigated tin electrodeposition on a vitreous carbon electrode from a sulfuric acid solution containing sodium gluconate as a chelating agent. From chronoamperometric studies, at high overpotential, they concluded that the nucleation process is instantaneous with diffusion control. At low overpotential, the nucleation process is either instantaneous or progressive, depending on the gluconate concentration. If the concentration of gluconate is 0.06 to 0.12M (low to medium), nucleation is instantaneous. At high gluconate concentration (0.2M), nucleation is progressive. The presence of gluconate favors two-dimensional growth under diffusion control. The calculated nucleus density and nucleus size are smaller in the presence of gluconate.

Barry et al [19] determined the synergistic effects of organic additives on the nucleation and growth mechanisms of tin electrodeposition on a rotating disk electrode. The polycrystalline copper working electrode was prepared by galvanostatically plating

copper on a platinum electrode. In all cases, hemispherical nucleation with three-dimensional (3D) growth was observed. According to the nucleation model <sup>[60]</sup> based on electron transfer control, it was found that Triton X-100, phenyl-2-butenalimine (AARP) and formaldehyde (HCHO), solely or in combination, altered the nucleation mechanism of tin electrodeposition. In the presence of a combination of Triton X-100, phenyl-2-butenalimine (AARP) and formaldehyde (HCHO), or combination of Triton X-100 and AARP, nucleation is instantaneous. In the sulfuric acid solution containing AARP and HCHO, or only AARP, nucleation is progressive. For other cases, no rate-limiting nucleation step was observed.

Petersson et al <sup>[61]</sup> studied the kinetics of electrodeposition of tin and tin-lead alloys on glassy carbon electrodes. The analysis of current transients clearly shows that deposition of tin and tin-lead alloys proceeds by instantaneous nucleation with a 3D growth mechanism limited by diffusion. A plot of applied overpotential versus the logarithm of the number density of nuclei ( $N_0$ ) is linear with a slope of 60 mV/decade, and so the density of nucleation sites increases exponentially with overpotential. The number of nucleation sites for tin-lead alloy is one order of magnitude larger than that for pure tin. They also reported when the concentration of the electrolyte was increased by a factor of 10, the characteristic nucleation behavior and the rate-limiting process was the same as in the low concentration, but the number of nucleation sites was smaller at the high concentration.



## 2.4 Morphology Study of Tin Electrodeposition at Initial Stages

Electrochemical techniques can be used to access the kinetics of nucleation and growth during metal electrodeposition, while scanning electron microscope (SEM) and atomic force microscopy (AFM) can be used to observe the surface microstructure, and provide information about the initial stages of metal electrodeposition. The SEM has a large depth of field, which allows a large amount of the sample to be in focus at one time. AFM provides a quantitative topographic map of surface features. Several authors have examined the formation of nuclei by these techniques [62-76]. But few reports [58, 59] are available for the initial stages of tin electrodeposition.

In Gomez's and co-workers' studies [58], the morphology of tin electrodeposits at the initial stages on vitreous carbon in acid tin solution without additives was examined by SEM. It was found that only a few crystallites of well-defined tetragonal shapes were observed at low overpotentials. In contrast, at high overpotentials, no well-defined crystals were observed. The crystallites had multiple shapes and overlapped, and the number of microcrystallites increased considerably. They also studied the surface morphology of tin electrodeposition on highly oriented pyrolytic graphite (HOPG) by AFM in the initial stages of tin electrodeposition. In order to attain a slow deposition rate, low overpotentials were applied in which the current transients showed a monotonic increase. Under these conditions, the number of microcrystallites increases with deposition time, and three-dimensional deposits were obtained. The growth of nuclei was favored in the horizontal direction rather than in the vertical direction. The number density of tin crystallites observed by SEM was  $1.3 \times 10^5 \text{ cm}^{-2}$  for 100 s at  $-530 \text{ mV}$ . At longer times (130s), AFM images revealed that the homogeneous distribution of deposit

on the terraces observed at shorter deposition times was lost. The overlap of growing microcrystallites was observed. However, large tin-free areas, some of which were even larger than those observed at shorter deposition times, remained on the terraces, probably due to surface diffusion.

Guaus et al<sup>[59]</sup> studied the morphology of tin electrodeposition on vitreous carbon electrode from a sulfuric acid solution containing sodium gluconate. A set of tin electrodeposits was formed potentiostatically at low overpotentials and short times. SEM images showed that the tin crystals were of uniform size, indicating that nucleation occurred instantaneously. The number of tin crystallites per unit area was  $1.5 \times 10^7 \text{ cm}^{-2}$  for 75 s at  $-625 \text{ mV}$ , and  $1.4 \times 10^8 \text{ cm}^{-2}$  for 50 s at  $-680 \text{ mV}$ .

## **2.5 Theory of Nucleation and Growth during Initial Stages of Electrodeposition**

Nucleation is a very important process in metal electrodeposition. The greater the number density of nucleation sites, the finer are the crystal grains of the deposit. In addition, the forms of the growing nuclei influence the appearance and structure of the deposit. With a higher growth rate normal to the substrate, for instance, a whisker, or columnar structure is obtained. A high growth rate parallel to the substrate provides a patchy structure. Thus, the initial stage of metal electrodeposition, or the formation of small clusters of atoms (nuclei), is significant for the overall electrodeposition kinetics, as well as the appearance, structure, and properties of the resulting coatings.

## 2.5.1 Multiple Nucleation with Mass Transfer Control

The early stages of metal electrodeposition are associated with two- or three-dimensional nucleation processes. The nucleation rate strongly depends on the activation overpotential, or electrochemical driving force for discharge of dissolved ions to the metallic state and their attachment to the substrate. It is therefore important to analyze the relationship between the overpotential and the rate of nucleation. Several theories describing these processes have been developed [77-92].

A nucleus, or a cluster of atoms, is stable only if it exceeds a critical size that depends on the electrochemical driving force for deposition. The creation of stable nuclei is an activation-controlled process. The growth of each individual nucleus is determined by the rate of incorporation of new atoms. In the case of mass-transfer control, the nucleus growth is limited by the rate at which metal ions diffuse through the solution to the electrode surface. Charge transfer rates for tin ion reduction in acid solution are usually fast so that diffusion to the established nuclei typically controls their growth rate.

In early studies of nucleation and growth kinetics of metal electrodeposition, Fleischmann and Thirsk [93, 94] used the potential step method in which the potential is stepped from zero overpotential to a constant finite overpotential and the current is measured as a function of time. The current transients showed a maximum, followed by an approximately exponential decay. They derived an equation to describe the rate of nuclei formation.

$$\frac{dN}{dt} = AN_0 e^{-At} \quad (2.8)$$

or

$$N = N_0(1 - e^{-At}) \quad (2.9)$$

where  $t$  is the time after the step,  $N$  the number density of nuclei,  $N_0$  the number density of active sites and  $A$  the nucleation rate constant. This nucleation rate law is of great significance, as it is assumed as a basis for more sophisticated models.

Astley et al. [95] investigated electrodeposition of mercury, silver and palladium on inert electrodes of vitreous carbon and pyrolytic graphite, and verified that the rate of growth is controlled by diffusion of mercury ions to the electrode surface. They classified the nucleation mechanism as either instantaneous, when all nuclei are formed immediately after the application of an overpotential, or progressive, when the nuclei are formed continuously following first-order kinetics. Astley et al modeled this situation by assuming that transfer of ions to individual nuclei occurs by one-dimensional diffusion. They derived the following expressions for the current transient for both instantaneous and progressive mechanisms:

$$i(t) = \frac{8zFM^2C^3D^{3/2}N}{\rho^2\pi^{1/2}}t^{1/2} \quad (2.10) \quad (\text{Instantaneous})$$

$$i(t) = \frac{16zAN_\infty FM^2C^3D^{3/2}}{3\rho^2\pi^{1/2}}t^{3/2} \quad (2.11) \quad (\text{Progressive})$$

where  $i(t)$  is the current density ( $A/cm^2$ ),  $M$  and  $\rho$  the molecular weight ( $g/mol$ ) and density ( $g/cm^3$ ) of the deposited metal,  $N$  the number density of growing nuclei,  $N_\infty$  number density of active sites ( $1/cm^2$ ),  $F$  Faraday's Constant ( $96486$  Coulomb/mole), and  $C$  and  $D$  the bulk concentration ( $mol/cm^3$ ) and diffusion coefficient ( $cm^2/s$ ) of the depositing metal ions.

These equations were modified by Hill et al <sup>[79]</sup> in terms of spherical diffusion to each nucleation site rather than linear diffusion. The following equations represent the current transients for instantaneous and progressive nucleation, respectively.

$$i(t) = \frac{zFN\pi(2DC)^{3/2} M^{1/2}}{\rho^{1/2}} t^{1/2} \quad (2.12) \quad (\text{Instantaneous})$$

$$i(t) = \frac{2zFAN_{\infty}\pi(2DC)^{3/2} M^{1/2}}{3\rho^{1/2}} t^{3/2} \quad (2.13) \quad (\text{Progressive})$$

These models are based on the assumption that the nuclei grow independently of one another and the current is the sum of the individual currents produced by each nucleus. However, experimental studies of multiple nucleation combined with microscopic observation of the electrode surface <sup>[96-97]</sup> show that the growth rate of N nuclei is different from that predicted by equations (2.12) and (2.13). The growth rates of individual nuclei are coupled because the diffusion fields around individual growth sites overlap. Scharifker and Hills <sup>[84-85]</sup> therefore introduced the concept of planar diffusion zones. In this model, hemispherical nuclei are randomly distributed on the electrode surface and grow under diffusion control as shown in Figure 2.2. A hemispherical diffusion zone radiating from each center grows such that its radius  $\delta$  is described as a function of time by:

$$\delta(t) = (kDt)^{1/2} \quad (2.14)$$

where k is an empirical constant. At short times, the radii of the diffusion zones are small and the current transients will be given by equations (2.12) and (2.13). However, as the nuclei grow, at some point the diffusion zones will overlap. After a long time, they form a linear diffusion layer, as illustrated in Figure 2.3, and the amount of metal ions

available for incorporation into the growing nuclei is reduced. The diffusive flux to a single nucleus is described by semi-infinite linear diffusion to the portion of the electrode surface within the circular perimeter of the growing diffusion zone. The planar area of one diffusion zone is

$$S(t) = \pi\delta^2(t) = \pi kDt \quad (2.15)$$

If  $N$  growing centers are nucleated instantaneously after the potential step, then the actual fraction ( $\theta$ ) of the area covered by diffusion zones taking overlap into account can be found by the Avrami theorem <sup>[98-100]</sup>,

$$\theta = 1 - \exp(-\theta_{ex}) \quad (2.16)$$

where  $\theta_{ex}$  is the fractional area covered by diffusion zones without overlap, which is equal to  $N\pi kDt$ .

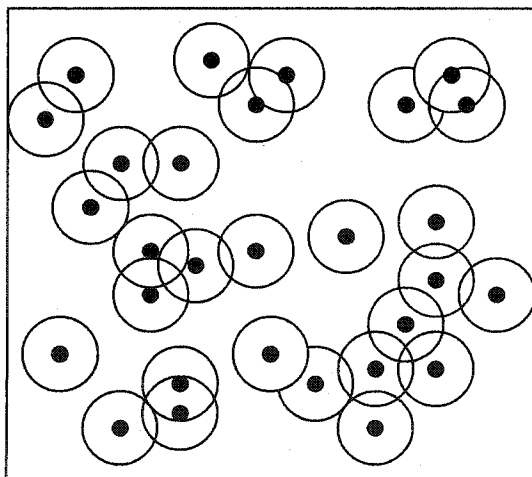


Figure 2.2 Schematic plan view of hemispherical nuclei (•) randomly distributed on the electrode surface. The surrounding circles represent their diffusion zones.

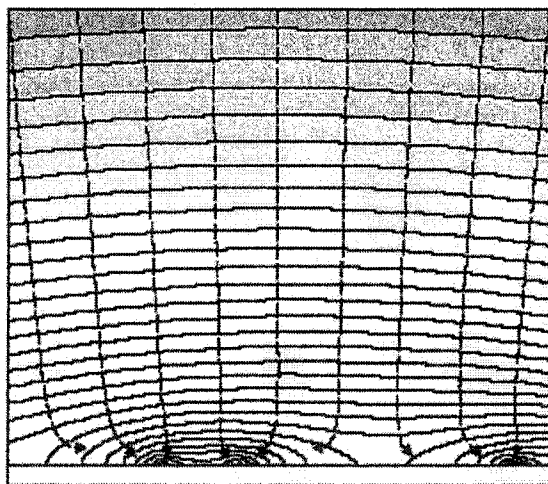


Figure 2.3 Schematic of the growth of diffusion zones around growing nuclei and their eventual overlap on an electrode surface. The arrows indicate the directions of diffusion.

The radial flux through the boundaries of the diffusion zones can be expressed as the equivalent planar flux to an electrode of fractional area  $\theta$ . By quasi-steady mass balance, the metal ions entering the diffusion zones must be incorporated into the growing nuclei. Therefore, the current density to the entire electrode is

$$i(t) = \frac{zFD^{1/2}C\theta}{(\pi t)^{1/2}} = \frac{zFD^{1/2}C}{(\pi t)^{1/2}} [1 - \exp(-N\pi kDt)] \quad (2.17)$$

At short times,  $Nt \rightarrow 0$ , the current density becomes:

$$i(t) = zFD^{3/2}C^{1/2}Nkt^{1/2} \quad (2.18)$$

This current density must be identical to that flowing to  $N$  isolated hemispherical nuclei, as described by equation (2.12). So  $k$  is defined as

$$k = \left( \frac{8\pi CM}{\rho} \right)^{1/2} \quad (2.19)$$

where  $M$  is the molecular weight and  $\rho$  density of the metal.

If nucleation is progressive,  $N(t) = AN_{\infty}t$  and

$$\theta_{ex} = \int_0^t AN_{\infty}\pi k' Dtdt = \frac{AN_{\infty}\pi k' Dt^2}{2} \quad (2.20)$$

The current density for progressive nucleation and growth follows as

$$i(t) = \frac{zFD^{1/2}C}{(\pi t)^{1/2}} \left[ 1 - \exp\left( \frac{-AN_{\infty}\pi k' Dt^2}{2} \right) \right] \quad (2.21)$$

and  $k'$  is again evaluated by taking the limit  $AN_{\infty}t \rightarrow 0$ , and comparing with equation (2.13),

$$k' = \frac{4}{3} \left( \frac{8\pi CM}{\rho} \right)^{1/2} \quad (2.22)$$

Equations (2.17) and (2.21) describe the current transients for instantaneous and progressive nucleation. In each case, the current passes through a maximum and then approaches the diffusion-limited current to a planar electrode. The maximum current and the time at which it occurs can be evaluated by setting the first derivative of the  $i$ - $t$  relation to zero. The resulting expressions for both instantaneous and progressive nucleation are given in Table 2-1.

Table 2-1 Expressions resulting from the analysis of the current transient maximum values for instantaneous and progressive nucleation

Instantaneous nucleation	Progressive nucleation
$t_m = \frac{1.2564}{N\pi kD}$ $i_m = 0.6382zFDC(kN)^{1/2}$ $i_m^2 t_m = 0.1629(zFC)^2 D$ $\frac{i^2}{i_m^2} = \frac{1.9542}{t/t_m} \left\{ 1 - \exp \left[ -1.2564 \left( \frac{t}{t_m} \right) \right] \right\}^2$	$t_m = \left( \frac{4.6733}{AN_\infty \pi k' D} \right)^{1/2}$ $i_m = 0.4615zFD^{3/4} C (k' AN_\infty)^{1/4}$ $i_m^2 t_m = 0.2598(zFC)^2 D$ $\frac{i^2}{i_m^2} = \frac{1.2254}{t/t_m} \left\{ 1 - \exp \left[ -2.3367 \left( \frac{t}{t_m} \right)^2 \right] \right\}^2$

This model is widely used to characterize the kinetics of nucleation as either instantaneous or progressive. But it suffers from the requirement of the two limiting cases. In the case of progressive nucleation, the parameters  $A$  and  $N_\infty$  can be estimated only in the form of their product. For instantaneous nucleation only the number of growing centers  $N$  can be estimated.

In practice, it is important to be able to determine  $A$  and  $N_\infty$  separately for all cases. In fact, the number of active sites varies with the overpotential <sup>[101-103]</sup>, and the



diffusion zones have different birth-times. To account for these, Scharifker and Mostany<sup>[86]</sup> introduced the appropriate time variable for consideration of the size of a diffusion zone at time  $t$ . The variable is  $(t-u)$  for a nucleus born at time  $u$ . According to the definition of radius of diffusion zone, the radius is given by

$$r_d = [kD(t-u)]^{1/2} \quad (2.23)$$

where  $k$  is defined by equation (2.18).

As with the Scharifker and Hills model, using the Avrami theorem, the fractional area covered by diffusion zones is expressed as

$$\theta = 1 - \exp\{-N_o \pi k D [t - (1 - e^{-At})]\} \quad (2.24)$$

The radial flux density of electroactive metal ions through the boundaries of the diffusion zones equates the equivalent planar diffusive flux to the electrode of fractional area  $\theta$ . Thus the expression for the current density is

$$i(t) = \frac{zFD^{1/2}C}{(\pi t)^{1/2}} \left( 1 - \exp\left\{-N_o \pi k D t \left(t - \frac{1 - e^{-At}}{A}\right)\right\} \right) \quad (2.25)$$

Setting the first derivative of this equation to zero, we can obtain the following non-linear equations to evaluate the nucleation rate constant ( $A$ ) and the number of active sites ( $N_o$ ). The current  $J_m$  and time  $t_m$  corresponding to the maximum can be obtained from the experimental current transients.

$$\ln\left(1 - \frac{i_m t_m^{1/2}}{a}\right) + x - \alpha \left(1 - e^{-x/\alpha}\right) = 0 \quad (2.26)$$

$$\ln\left(1 + 2x \left(1 - e^{-x/\alpha}\right)\right) - x + \alpha \left(1 - e^{-x/\alpha}\right) = 0 \quad (2.27)$$

where

$$\alpha = b/A, \quad a = \frac{zFD^{1/2}C}{\pi^{1/2}}, \quad b = N_0\pi kD, \quad x = bt_m, \quad k = \left( \frac{8\pi CM}{\rho} \right)^{1/2}$$

Under this model, it is not necessary to classify the nucleation process as instantaneous or progressive. Furthermore, this theory allows separate determination of A and  $N_0$ . Equation (2.25) is widely used as it can be directly compared to experimental data based on the parameters  $N_0$  and A.

Some attempts have been made to improve this model. Sluyters-Rehbach et al <sup>[87]</sup> argued that in order to preserve a uniform thickness of the diffusion layer appropriate to planar diffusion, the hypothetical planar flux should not relate only to their age but also to their time of formation. In the model developed by Mirin and Nilov <sup>[88]</sup>, it was noted that multiplying the covered area fraction with the Cottrell equation is not correct as the planar diffusion zones in progressive nucleation have different times of formation, and hence, must be accounted for by initiating the Cottrell equation at different times for each zone. Heerman et al <sup>[104-106]</sup> have later presented the same theory as Mirkin and Nilov, and discussed the resulting transients in detail. These models are more complicated than Scharifker and Mostany one, but all yield similar results, and accordingly, parameters extracted from experimental data are similar.

## 2.5.2 Critical Gibbs Free Energy and Critical Nucleus Size

From a thermodynamic point of view, if the ambient phase is supersaturated, a new phase larger than a critical size will grow spontaneously. In the electrodeposition system, the ions transfer from the solution to the electrode surface across the electrochemical double layer under the influence of the overpotential ( $\eta$ ), which is a

measure of supersaturation. The Gibbs free energy of nucleus formation with respect to the bulk phase can be expressed in the form <sup>[107]</sup>

$$\Delta G(n) = -nze\eta + \Phi(n) \quad (2.28)$$

where  $\Delta G(n)$  is the Gibbs free energy of nucleus formation,  $n$  the number of atoms in the nucleus,  $z$  the valency of the metal ions,  $e$  the elementary electron charge, and  $\Phi(n)$  the total surface excess free energy.

According to equation (2.28), The Gibbs free energy of nucleus formation is the sum of the bulk energy and surface energy of the nucleus. The first term is related to the transfer of  $n$  atoms from the liquid phase to the substrate surface because the solution is supersaturated, this term is always negative. The second term represents an excess free energy that arise from the energy contributions derived from the deviation of the new phase from the bulk phase. Both terms are functions of the size  $n$  of the nucleus. In the first approximation, the first term increases linearly with  $n$ , and the second term increases with the power  $^{2/3}$  of  $n$  <sup>[108]</sup>. As the size of the nucleus increases, the Gibbs free energy of nucleus formation pass through a maximum at the critical nucleus size  $n_{crit}$ .

There are two theories for quantitative evaluation of critical Gibbs free energy for critical nucleus formation and critical nucleus size: classical theory and atomistic theory. The classical approach is based on the macroscopic surface tension concept, and the atomistic approach is based on the binding energy of an atom to a nucleus.

- **Classical Nucleation Theory**

In the classical model, the size of the nucleus is a continuous variable. The nucleus is assumed to be in the equilibrium form, in which the total surface energy is minimized. For a 3D nucleation process, by differentiation of equation (2.28) with

respect to  $n$  under the condition  $d\Delta G(n)/dn = 0$ , the critical Gibbs free energy and critical nucleus size can be expressed by <sup>[109]</sup>

$$n_{crit} = \frac{8BV_m^2\sigma^3}{27(ze\eta)^3} \quad (2.29)$$

$$\Delta G_{crit} = \frac{4BV_m^2\sigma^3}{27(ze\eta)^2} = \frac{n_{crit}ze\eta}{2} \quad (2.30)$$

where  $V_m$  is the volume occupied by one atom,  $\sigma$  is the average specific surface energy, and  $B$  is a constant value that depends on the geometry. For a sphere,  $B = 36\pi$  and for a cube  $B = 6^3$ .

Kashchiev <sup>[110, 111]</sup> derived the differential form of  $\Delta G_{crit}$  with respect to  $\eta$ :

$$\frac{d\Delta G_{crit}}{d\eta} = -zen_{crit} \quad (2.31)$$

Equation (2.31) is applicable to all cases of nucleation, and not restricted by any assumptions about size or form of the nucleus.

The rate of nucleation is governed by activated kinetics where  $\Delta G_{crit}$  plays the role of an activation energy. The relationship of the steady state nucleation rate to the critical Gibbs free energy for the critical nucleus formation was derived by Volmer and Weber <sup>[112]</sup>.

$$J_{st} = K \exp\left(-\frac{\Delta G_{crit}}{kT}\right) \quad (2.32)$$

where  $K$  is a constant, and  $k$  is the Boltzmann constant.

Substitution of equation (2.30) into (2.32) to give

$$J_{st} = K \exp\left(-\frac{4BV_m^2\sigma^3}{27(ze\eta)^2 kT}\right) \quad (2.33)$$

From the intercept of the plot of  $\ln(J_{st})$  vs  $1/\eta^2$ , the parameter  $K$  can be obtained, and from the slope, the nucleation rate parameters involved in equation (2.33) can be found. Therefore, with equations (2.29) to (2.33) the parameters  $\Delta G_{crit}$  and  $n_{crit}$  of the critical nucleus can be evaluated.

- **Atomistic Nucleation Theory**

The atomistic theory relating nucleation rate to supersaturation was first suggested by Walton <sup>[113, 114]</sup> and later developed by Stoyanov <sup>[115]</sup>. In this model, the nucleation rate at steady state can be presented in the form <sup>[109]</sup>

$$J_{st} = A(N_o, n_{crit}) \exp\left(\frac{\beta^* z e \eta}{kT}\right) \exp\left(\frac{n_{crit} z e \eta}{kT}\right) \quad (2.34)$$

The factor  $\beta^*$  depends on the mechanism of attachment of one atom to the critical cluster. In the case of direct transfer,  $\beta^* = 0.5$ , or it is equal to unity for adatom attachments. The plot of  $\ln J_{st}$  vs  $\eta$  is a straight line. From the slope, the  $n_{crit}$  parameter can be obtained. The contribution of  $\beta^*$  makes the uncertainty of the critical nucleus size  $n_{crit}$  by 0.5 or 1 atoms insignificant.

## CHAPTER 3

### EXPERIMENTAL METHODS

#### 3.1 Nucleation and Growth Kinetics of Tin and Tin-Silver Alloy Electrodeposition

##### 3.1.1 Experiment setup

The electrochemical cell used for the kinetics studies is shown in Figure 3.1. A 100 ml beaker served as the main electrolyte compartment. The working electrode was a single-crystal copper disk (Goodfellow), or an electroplated copper or nickel layer on a platinum disk. The single-crystal copper disk with nominal surface area of  $0.785 \text{ cm}^2$  was mounted in a Teflon holder. The platinum rotating disk with a surface area of  $0.126 \text{ cm}^2$  was received from the manufacturer molded in a Teflon cylinder. The preparation of working electrode surfaces is described in Sections 3.3.2 and 3.3.3.

The counter electrode was a carbon rod. A silver/silver chloride (Ag/AgCl) electrode was used as the reference electrode. The inner compartment of this reference electrode was filled with a saturated KCl-AgCl solution and terminated with a porous frit. The frit was inserted in a bridge tube filled with 1M  $\text{H}_2\text{SO}_4$  and fitted with a porous glass frit. The bridge tube frit was dipped into the working electrolyte. Unless specifically

noted, all potentials in the text are reported with respect to the Ag/AgCl reference electrode.

The control system consisted of a Bipotentiostat Model AFCBP1 and HP Pavilion computer with PineChem software, shown in Figure 3.2. The potentiostat, which controls the potential of the working electrode, is designed to work with a three-electrode cell in a way which assures that all current flows between the counter and working electrodes. The experimental parameters were executed by the PineChem program. All experiments were carried out under atmospheric pressure and at room temperature.

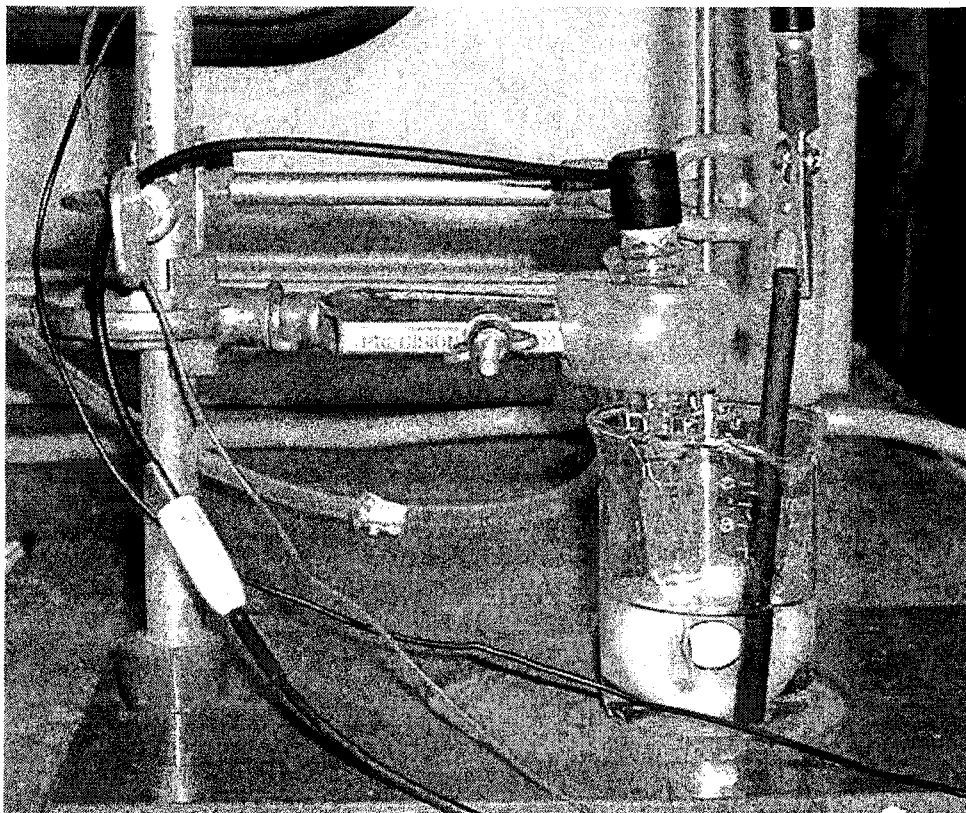


Figure 3.1 Experimental setup of the electrolysis cell

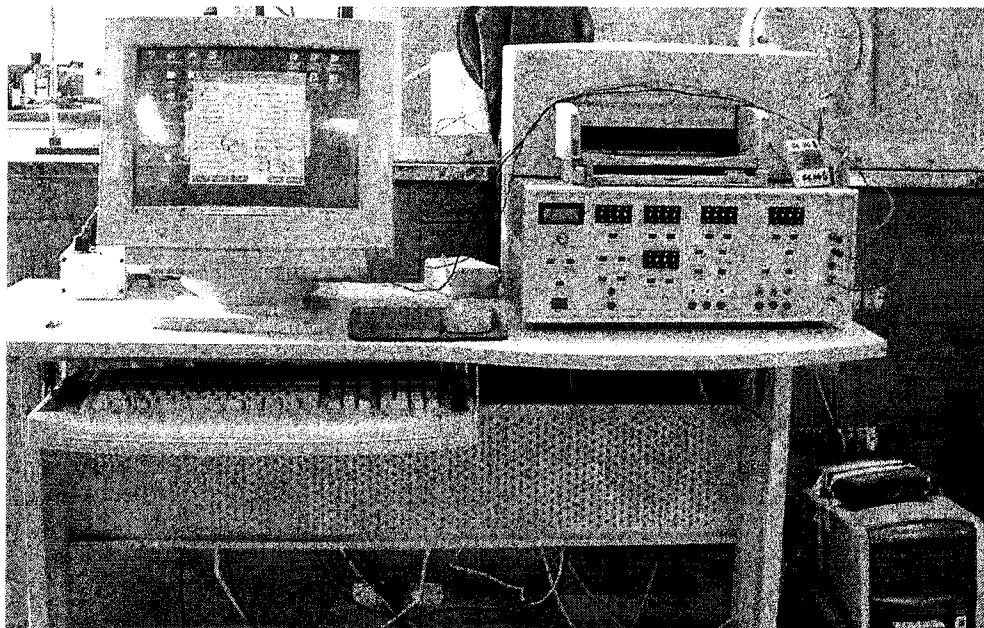


Figure 3.2 Control system of the electrolysis cell

### 3.1.2 Cyclic voltammetry

Cyclic voltammetry is an electroanalytical technique used to determine charge transfer mechanisms and the rate of redox reactions. In cyclic voltammetry (CV) the potential applied to the working electrode (WE) is scanned linearly from an initial value ( $E_i$ , with respect to Ag/AgCl reference electrode) to a second value ( $E_f$ ) and then back to  $E_i$ . The current flowing between the working electrode (WE) and the counter electrode (CE) is recorded as a function of time and potential.

Prior to each experiment, the working electrode surface was cleaned sonically for 2 min in ethanol (99.5%), and then rinsed with ultrapure water. The electrolysis cell was assembled and filled with solution so that the ends of all electrodes were immersed. After making all necessary electrical connections between the electrodes and the potentiostat,



the potentiostat was turned on. All experiment settings were adjusted as shown in Figure 3.3.

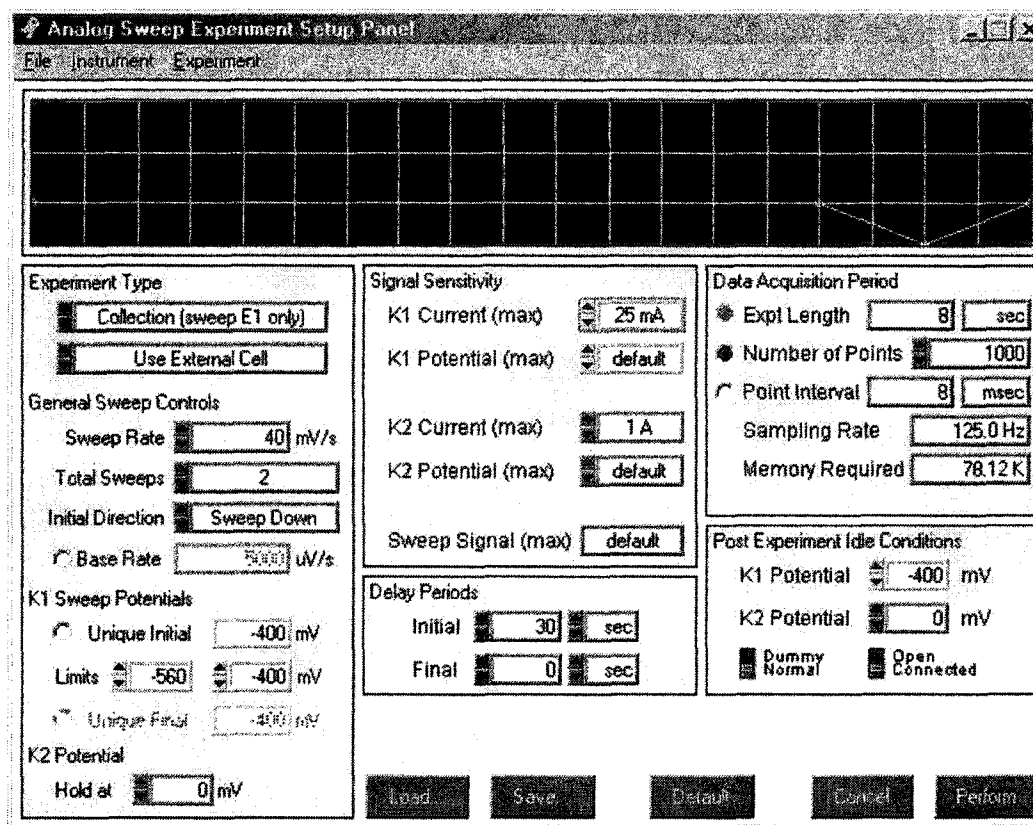


Figure 3.3 Experimental settings for cyclic voltammogram measurements

In the experiment, the system is started at an initial potential,  $-400\text{mV}$ , at which no net current passes through the working electrode. The potential is then swept negatively to generate a cathodic current. Initially, the current increases as nuclei are formed and the active growth area increases. Then the current decreases as the concentration of reactants is depleted near the electrode surface. The potential scan is reversed at  $-560\text{ mV}$ , and swept back to  $-400\text{ mV}$ . At the more positive potential some oxidation of the deposited metal occurs.

### 3.1.3 Potentiostatic Current Transient Measurement

In the potential step measurement the applied potential was stepped from the open circuit potential  $V_i$  (-465 mV for tin solution with and without thiourea, -430 mV for tin solution with thiourea and silver) to a predetermined potential  $V_f$  (-545, -550, -555, -560, -565, -570, -580 mV). The applied potentials were determined based on the results of cyclic voltammograms. The transient current was then measured as a function of time. The duration of the potential step experiments was 200 ms. Figure 3.4 shows the experimental settings.

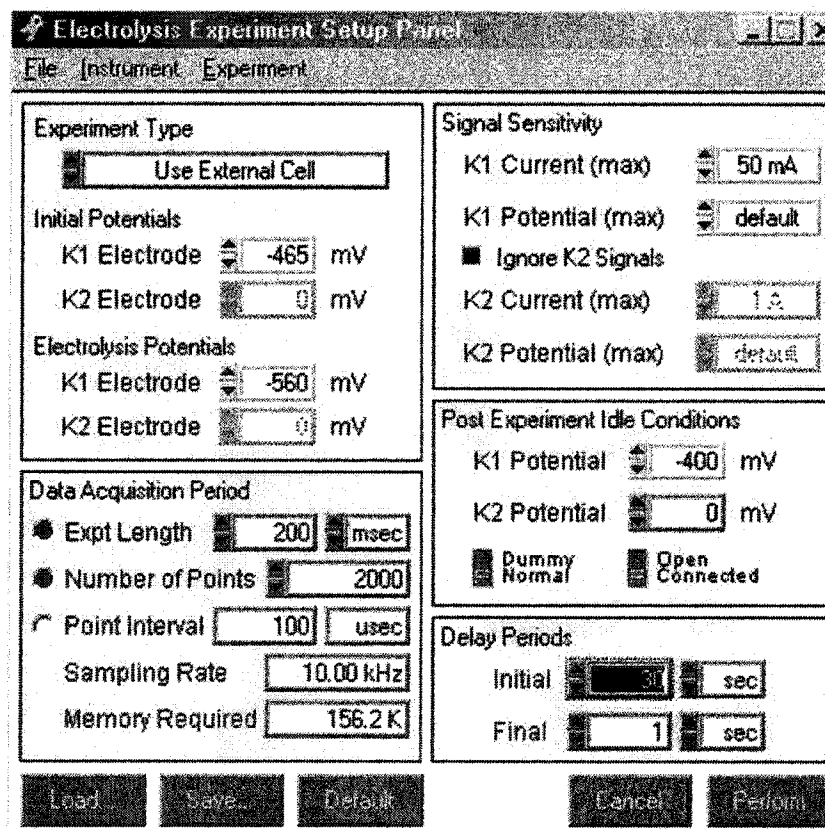


Figure 3.4 Experimental settings for potential step measurement

## **3.2 Morphology Studies of Tin and Tin-Silver Electrodeposition**

### **3.2.1 Atomic Force Microscopy**

The Atomic Force Microscope (AFM) is a mechano-optical instrument used to produce 3-D facsimiles of surface topography. The AFM used in this study produced images with a vertical resolution of about 1 nm and a horizontal resolution of a few tenths of a nanometer.

Figure 3.5 illustrates how the AFM works. The AFM utilizes a sharp tip moving over the surface of a sample in a raster scan with a feedback unit. The tip is mounted on the end of a cantilever. The cantilever provides a support for the tip and is deflected by pressure upon the tip. The tip is initially pressed onto the sample surface so it bends slightly. As the tip scans the surface of the sample, moving up and down with the contour of the surface, a laser beam is deflected off the attached cantilever onto a split photodiode. The photodiode returns a voltage describing the laser position. This voltage along with the XY coordinates of the scan is fed into a computer which produces an image. Using this method the AFM can image objects only a few tens of nanometers in dimension.

A piezoelectric scanner performs the movement of the sample. The AFM uses piezoceramics mounted in a single tube. Each tube consists of five or more independently operated piezo elements. Application of voltages to one or more of the elements causes the tube to bend or stretch, moving the sample in three dimensions.

With the electronic feedback on, the positioning piezo which moves the sample (or tip) up and down can respond to any changes in force which are detected, and alter the tip-sample separation to restore the force to a pre-determined value. This is known as

height mode (constant force), and it enables a topographical image to be obtained. If the feedback electronics are switched off, then the microscope is said to be operating in constant height or deflection mode. This is particularly useful for imaging very flat samples at high horizontal resolution.

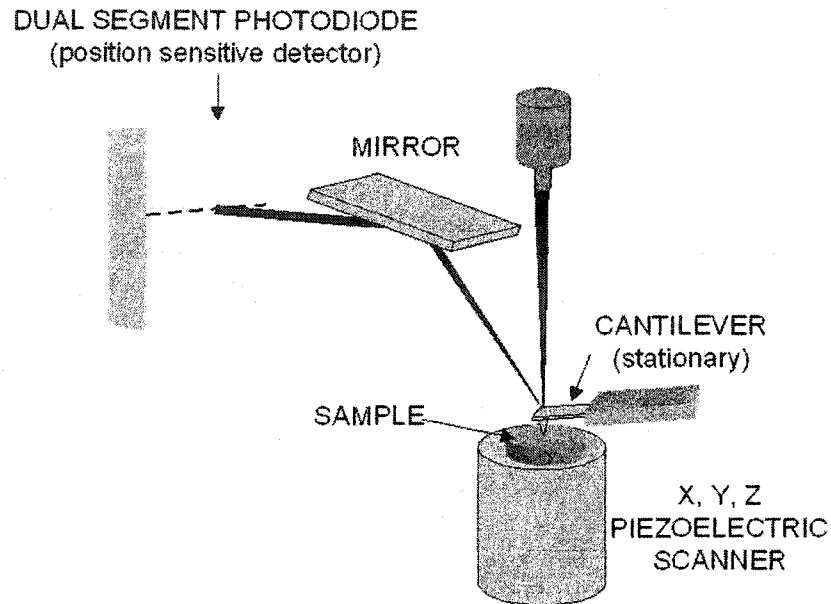


Figure 3.5 Schematic principal of AFM measurements

### 3.2.2 AFM Experiment setup

The experiments were performed with a Digital Instrument NanoScope E atomic force microscope equipped with a 12  $\mu\text{m}$  scanner. The setup is shown in Figure 3.6. The single-crystal copper disk was mounted on the scanner. The optical head, which holds the cantilever, was placed over the center of the sample disk. Head stabilizing springs were installed and the head was leveled with a set of screws. The AFM was engaged after

adjustment of the laser signal. Images were captured in height and deflection mode simultaneously.

The samples used in the AFM study were tin or tin silver alloy which was deposited on the single-crystal copper disk. Following electrochemical deposition, the samples were removed from the Teflon holder, rinsed three times with ultrapure water, and dried in air.

### **3.2.3 SEM Imaging**

The samples were prepared in the same way as for the AFM study, and delivered to the Instrumentation Center for characterizing the morphology of the different electrodeposits with SEM.

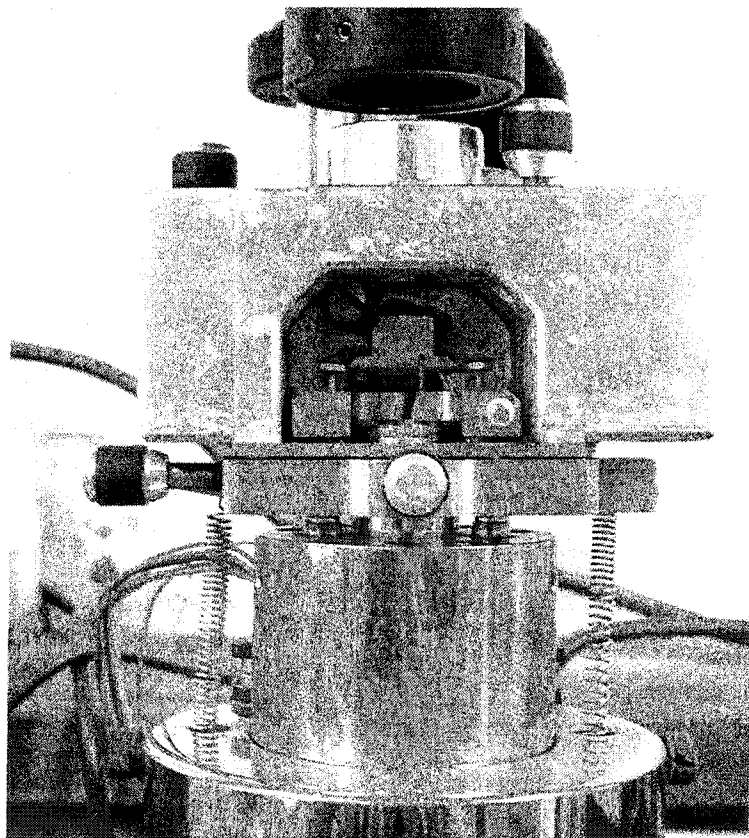
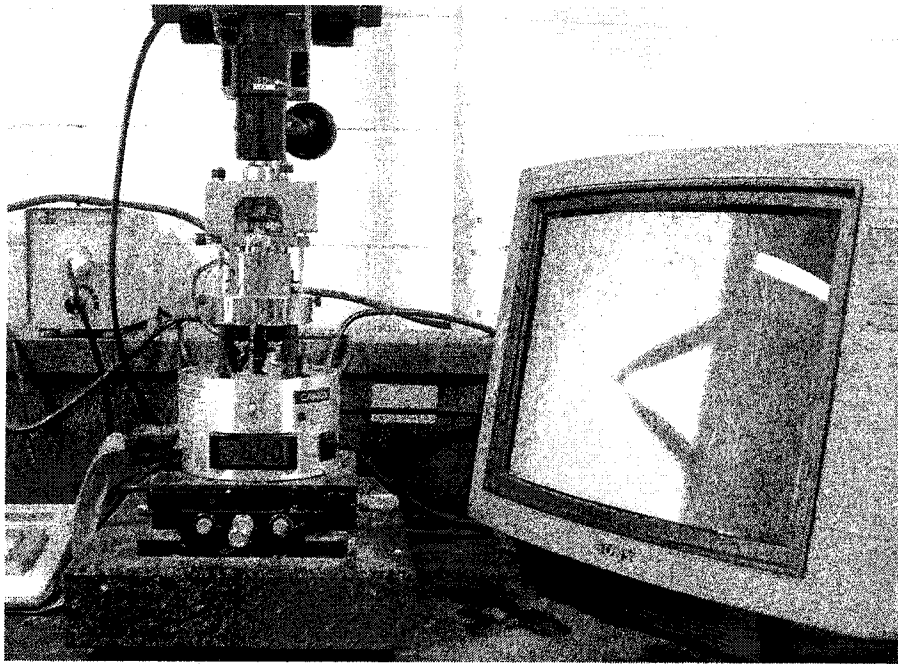


Figure 3.6 AFM experimental setup

### 3.3 Experimental Materials and Preparation

#### 3.3.1 Polishing System

Copper single-crystal disk electrodes were mechanically polished using a fine grinding-polishing system, which comprises a Struers RotoPol-11 polishing machine and a Struers RotoForce-1 rotator (Struers Inc., Westlake, OH). The preparation of a substrate required a series of polishing steps with different polishing compounds, applied force and time.

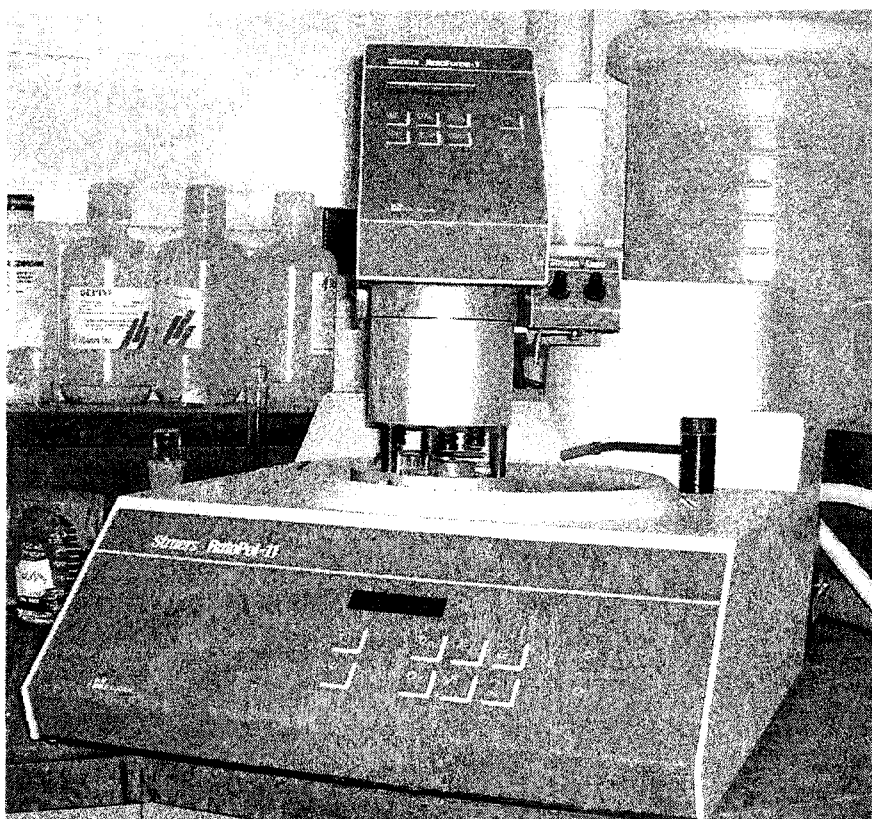


Figure 3.7 Polishing system

Figure 3.7 shows the schematic view of the polishing system. In a grinding-polishing process, a holder, which was mounted on the rotator, held the copper disk with the polished surface facing the horizontal rotating polishing wheel. On the top of the wheel is a removable abrasive cloth on which the lubricant or colloidal silica suspension is poured. The holder and wheel rotate in the same direction but with two rotating axes offset by some distance. The rotating speed of the holder and wheel and the pressure applied on the substrates can be varied by adjustment of the control panel. A lubricant delivery system was used to quantify the amount of lubricant for the polishing process.

### 3.3.2 Single-crystal copper disk Substrate Preparation

The overall polishing procedures consist of four steps, as outlined below:

- Grind the sample until the surface is uniform and perpendicular to the disk axis.
- Polish the sample until the surface is uniform and scratch free.
- Polish / etch the sample until the surface is uniform and bright.
- Clean the sample until the surface is deposit free.

Step #1: Grind sample until surface is uniform and perpendicular to disc axis

Parameters	Materials, Settings & Procedures
Rotating Speed (rpm)	300
Wheel Surface	Cloth (Struers MD-Pan)
Diamond Compound	6 $\mu\text{m}$ diamond (Struers DP-Spray)
Total Load (Newtons)	30
Lubricant	Ultrapure water
Lube Dosing	60 drops per minute
Time	4-10 minutes, depends on initial surface of substrate



Etchant	None
Clean sample	Rinse with ultrapure water

Step #2: Polish sample until surface is uniform and scratch free

Parameters	Materials, Settings & Procedures
Rotating Speed (rpm)	150
Wheel Surface	Cloth (Struers MD-Mol)
Polishing Compound	3 $\mu$ m Diamond (Struers DP-Spray)
Total Load (Newtons)	25
Lubricant	DP-Lubricant Red, HQ
Lube Dosing	25 drops per minute
Time	5 minutes
Etchant	None
Clean sample	Rinse with ultrapure water

Step #3: polish/Etch sample until surface is uniform and mirror-like

Parameters	Materials, Settings & Procedures
Rotating Speed (rpm)	150
Wheel Surface	Cloth (Struers MD-Chem)
Polishing Compound	3 $\mu$ m Diamond (Struers DP-Spray)
Total Load (Newtons)	20
Lubricant	OP-S suspension (See Etchant Recipe)
Lube /Etchant dosing	1) Wet entire disc surface prior to polish with 2 ml 2) Then dose the surface by a dropper
Time	1 minute
Clean sample	Rinse with ultrapure water
Etchant Recipe	Make etchant solution immediately before use 1) 10 ml of OP-S Suspension in 50 ml Beaker 2) Add 6 drops (0.2ml of NH <sub>4</sub> OH) to the same beaker 3) Add 9 drops (0.3ml of H <sub>2</sub> O <sub>2</sub> ) to the same beaker

Step #4: Clean sample until surface is uniform, mirror-like, and deposit free

Parameters	Materials, Settings & Procedures
Clean in ethanol (99.5%)	1) Put the disk sample polished side up into the 50ml beaker which contains 35ml ethanol. 2) Then put the beaker into the Ultrasonic cleaning apparatus, which has been $\frac{3}{4}$ filled with water and turn on for 2 minute.
Clean in ultrapure water	3) Put the disk sample polished side up into the 50ml beaker which contains 35ml ultrapure water. 4) Then put the beaker into the Ultrasonic cleaning apparatus, which has been $\frac{3}{4}$ filled with water and turn on for 2 minute.
Rinse and Dry	Rinse the sample with ultrapure water 3 times and let it dry in air.

### 3.3.3 Preparation of Bright Polycrystalline Copper Substrate and Polycrystalline Nickel Substrate

The platinum rotating disk (RDE) is a hydrodynamic working electrode used to control mass transfer to the electrode surface. The steady state hydrodynamic equations and the convective-diffusion equation have been solved, and the experimental parameters can be related to the mass transfer of reactants to the electrode surface. The RDE is constructed from a platinum disk imbedded in a rod of insulating Teflon. The electrode is attached to a motor and rotated at a controlled frequency. The movement of rotation leads to a very well defined solution flow pattern. The rotating disk acts as a pump, pulling the solution upward and then throwing it outward. Figure 3.8 shows the flow pattern of RDE.

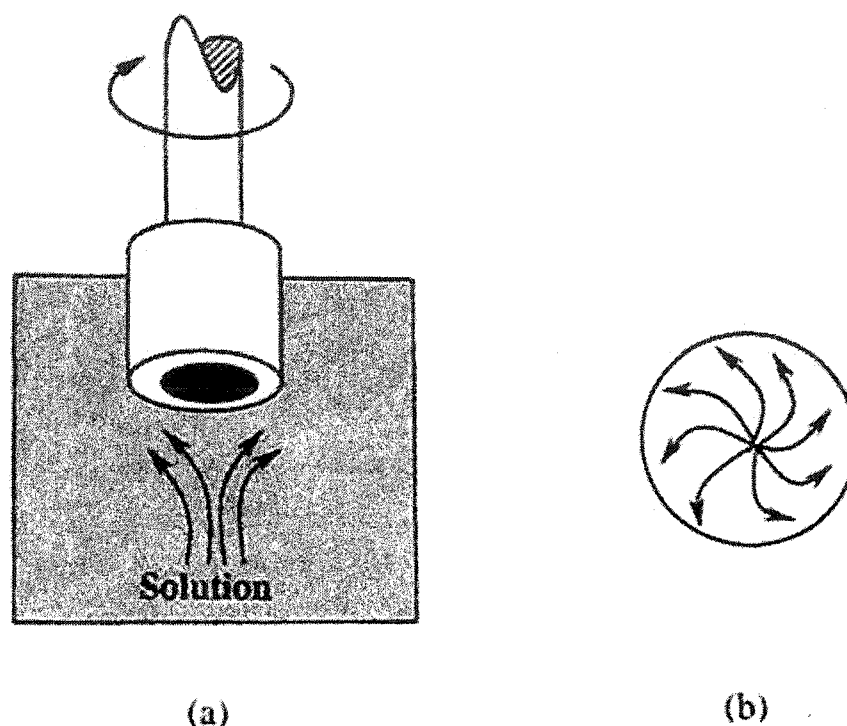


Figure 3.8. Schematic diagram of fluid flow on the RDE

In the preparation of bright polycrystalline copper substrates, galvanostatic deposition was used. The platinum rotating disk electrode with diameter of 0.4 cm as a working electrode was mounted on an EG & G PARC Model 616 rotator. Counter and reference electrodes were a copper plate. With the rotating speed set at 800 rpm, constant cathodic current (2mA) was applied to the Pt-RDE electrode for 29 min to produce a 10  $\mu\text{m}$  thick bright polycrystalline copper layer. Prior to each experiment the Pt-RDE was cleaned with  $\text{H}_2\text{O}_2\text{-H}_2\text{SO}_4$  (60:40) solution for 30 min to strip impurities completely, then rinsed three times with ultrapure water. The acidic copper sulfate solution was prepared with reagent grade chemicals and ultrapure water. The compositions were  $0.25\text{M CuSO}_4 \cdot 5\text{H}_2\text{O} / 1.8\text{M H}_2\text{SO}_4 / 1\text{mM HCl} / 300\text{mg/l PEG} / 10\mu\text{M MPSA}$ .

The polycrystalline nickel substrates were prepared in the same way as the preparation of polycrystalline copper substrates. A constant cathodic current (1.5mA) was applied to the Pt-RDE electrode for 25 min, producing a 6  $\mu\text{m}$  thick polycrystalline nickel layer. The Watts nickel bath was used, and the bath temperature was kept at  $50 \pm 0.5^\circ \text{C}$  during electroplating. The Watts nickel compositions are as follows:

- 300 g/l Nickel Sulphate,  $\text{NiSO}_4 \cdot 6\text{H}_2\text{O}$
- 50 g/l Nickel Chloride,  $\text{NiCl}_2 \cdot 6\text{H}_2\text{O}$
- 40 g/l Boric Acid,  $\text{H}_3\text{BO}_3$

The EG&G Instruments • VersaStat<sup>TM</sup> II Model 253 potentiostat was used to apply the current to the working electrode. The potentiostat was controlled by a computer (Compaq Presario 5000) via an IEEE-488 (GPIB) interface with EG & G Instruments • Virtual Potentiostat software. Figure 3.9 indicates the set-up.

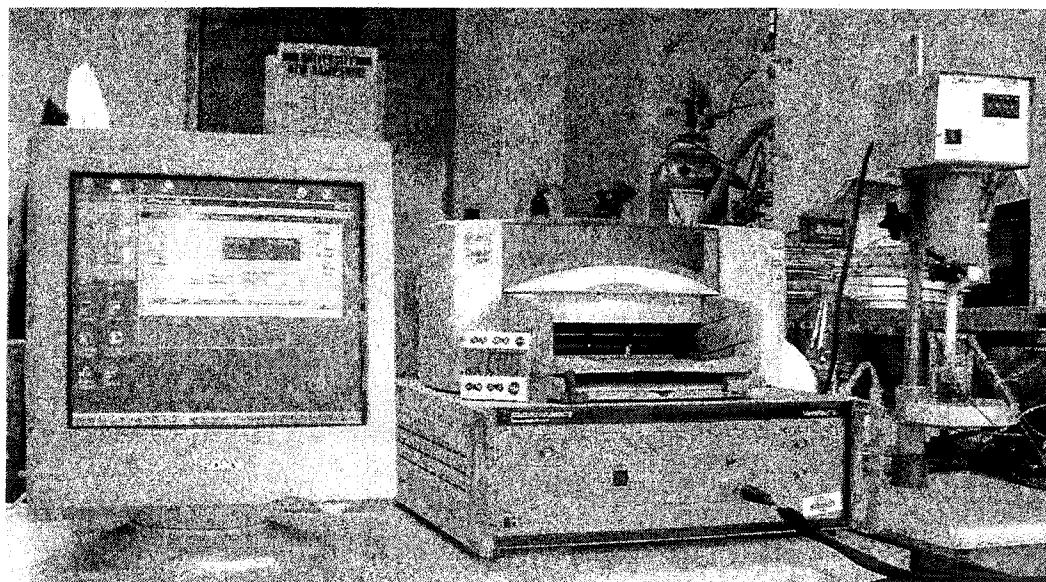


Figure 3.9 Experimental setup for electrodeposition of bright polycrystalline copper and polycrystalline nickel on the platinum rotating disc electrode.

Before each nucleation experiment, the bright polycrystalline copper and polycrystalline nickel substrates were cleaned with ethanol (99.5%), and then rinsed three times with ultrapure water.

### 3.3.4 Solution Preparation

In this study, all of the solutions were made with ultrapure water produced in a Nanopure II Ultrafiltration system. The resistivity of the water was 17-18 M $\Omega$ •cm. The chemical reagents used for the preparation of electrolyte solutions are listed in Table 3-1. The six electroplating solutions used to study the nucleation and growth kinetics are shown below.

- 0.02M SnSO<sub>4</sub> + 1.0M H<sub>2</sub>SO<sub>4</sub>
- 0.02M SnSO<sub>4</sub> + 1.0M H<sub>2</sub>SO<sub>4</sub> + 0.02MTu
- 0.02M SnSO<sub>4</sub> + 1.0M H<sub>2</sub>SO<sub>4</sub> + 0.02MTu + 2mMAgNO<sub>3</sub>
- 0.02M SnMS + 1.0M MSA
- 0.02M SnMS + 1.0M MSA + 0.02MTu
- 0.02M SnMS + 1.0M MSA + 0.02MTu + 2mMAgNO<sub>3</sub>

**Tu:** Thiourea

**MSA:** Methanesulfonic Acid

**SnMS:** Tin Methanesulfonate

Table 3-1 Chemical Reagents

Chemicals	Formula	Content(%)	Source
Sulfuric Acid	H <sub>2</sub> SO <sub>4</sub>	99.99 %	Aldrich
Methanesulfonic Acid	CH <sub>3</sub> SO <sub>3</sub> H	99.5+ %	Aldrich
Tin Sulfate	SnSO <sub>4</sub>	95+ %	Aldrich
Tin Methanesulfonate	Sn(CH <sub>3</sub> SO <sub>3</sub> ) <sub>2</sub>	50wt. %	Aldrich
Thiourea	H <sub>2</sub> NCSNH <sub>2</sub>	99+ %	Aldrich
Silver Nitrate	AgNO <sub>3</sub>	99+ %	Aldrich

### 3.3.5 Cleaning of Electrochemical Cell

A strict cleaning protocol was followed since trace amounts of impurity affect the nucleation and growth kinetics of electrodeposits. All the glassware used in the experiment was first washed with water and mild detergent, and rinsed with ultrapure water. It was then immersed into hot fuming sulfuric acid (98%) for 15 minutes, rinsed three times with ultrapure water, then boiled in ultrapure water for 15 minutes, and finally rinsed three times with ultrapure water and air-dried.

## CHAPTER 4

# NUCLEATION AND GROWTH KINETICS OF TIN AND TIN-SILVER ALLOY ELECTRODEPOSITION

To study nucleation and growth kinetics of Sn and Sn-Ag alloy, the conventional electrochemical techniques of cyclic voltammetry (CV) and chronoamperometry (CA) were used. Cyclic voltammetry was used to assess reaction mechanisms and to find a suitable potential range for electrodeposition. Chronoamperometry was used to study nucleation and growth kinetics in diffusion-controlled electrodeposition and to determine the number density of active sites and the nucleation rate constant.

In this study, three substrates (single crystal copper, bright polycrystalline copper, and polycrystalline nickel) and six electrolyte solutions were used. The solutions were:

- 0.02M SnSO<sub>4</sub> + 1.0M H<sub>2</sub>SO<sub>4</sub>
- 0.02M SnSO<sub>4</sub> + 1.0M H<sub>2</sub>SO<sub>4</sub> + 0.02MTu
- 0.02M SnSO<sub>4</sub> + 1.0M H<sub>2</sub>SO<sub>4</sub> + 0.02MThiourea + 2mMAgNO<sub>3</sub>
- 0.02M SnMS + 1.0M MSA
- 0.02M SnMS + 1.0M MSA + 0.02MTu
- 0.02M SnMS + 1.0M MSA + 0.02MTu + 2mMAgNO<sub>3</sub>

**Tu:** Thiourea; **MSA:** Methanesulfonic Acid; **SnMS:** Tin Methanesulfonate. (Refer to Table 3-1)

## 4.1 RESULTS

### 4.1.1 Cyclic Voltammetry

Cyclic voltammograms for electrodeposition of tin in sulfuric acid / stannous sulfate solution with and without additives are shown in Figure 4.1. At a scan rate of 40 mV/s, the onset of  $\text{Sn}^{2+}$  reduction current occurred at  $-495$  mV, and the cathodic current peaked at  $-525$  mV in pure tin solution without additives. With thiourea, the  $\text{Sn}^{2+}$  reduction potential shifted to more negative values. The reduction started at  $-509$  mV, and the cathodic current peak occurred at  $-535$  mV. There was a single reduction and oxidation peak for the tin solutions with and without thiourea in the cyclic voltammograms, and no diffusion limiting current plateau was observed. The presence of a single reduction current peak indicates that a single charge transfer process occurred during the reduction of  $\text{Sn}^{2+}$ .

In tin solution containing thiourea and silver, two distinct cathodic peaks were observed in the current-potential curve. The first, minor peak occurred at  $-480$  mV. The second one, much larger than the first, was situated at  $-529$  mV, which corresponds to the single peak observed in the pure tin solution. The observation of two separate peaks suggests that the silver deposits first on the single crystal copper substrate. Because the large tin peak occurs at a potential more positive than for tin/thiourea, deposited silver appears to promote the nucleation of tin.

The reversibility of electrodeposition and dissolution of tin on the single crystal copper electrode was evaluated by cyclic voltammetry. Typical results obtained at 40 mV/s for the continuous potential scans in different solutions are displayed in Figure 4.2



to 4.4. The cyclic voltammograms are completely overlapped, and a good reproducibility was also seen at different scan rates.

The scan rate dependences of the potential and current density for the cathodic peak in the cyclic voltammograms are shown in Figure 4.5 to 4.7. The peak potential shifted more negative, and the current function, i.e. the peak current density divided by the square root of scan rate, decreased as the scan rate increased. These results which are shown in Table 4-1, imply that the electrodeposition of tin at the single crystal copper electrode is a quasi-reversible process.

Table 4-1 The cathodic peak current and current function in sulfuric acid solution

Scan Rate (v)	Pure tin solution		With Thiourea		with thiourea and silver	
	Cathodic Peak ( $i_p$ )	$i_p/v^{1/2}$	Cathodic Peak ( $i_p$ )	$i_p/v^{1/2}$	Cathodic Peak ( $i_p$ )	$i_p/v^{1/2}$
20	6.45	45.6	8.43	59.6	6.92	48.9
40	8.66	43.3	11.0	54.9	9.25	46.3
60	10.3	42.0	13.0	53.2	10.8	44.3
80	11.7	41.4	14.5	51.4	12.2	43.2
100	12.9	40.6	15.8	49.9	13.3	41.9

The electrochemical behavior of  $\text{Sn}^{2+}$  reduction on the bright polycrystalline copper and polycrystalline nickel substrates is shown in Figure 4.8 and 4.9, respectively. The effect of substrate on the cyclic voltammogram is shown in Figure 4.10 and 4.11. Whether the working electrode was single crystal copper, polycrystalline copper or polycrystalline nickel, the curves exhibit similar shapes. But for tin electrodeposition on polycrystalline nickel without additives (Figure 4.10), the onset of  $\text{Sn}^{2+}$  reduction current

occurred at  $-490$  mV,  $5$  mV more positive than on copper substrates. A small current occurs at potentials more positive than the open-circuit potential. This current probably is due to underpotential deposition. In the other cases, the corresponding reduction current occurred at about the same potential.

Typical cyclic voltammograms for the reduction of tin in methanesulfonic acid solution are shown in Figure 4.12. The same electrochemical behaviors of  $\text{Sn}^{2+}$  reduction as in sulfuric acid solution are observed, and the polarization curves exhibit similar shapes. In comparison with sulfuric acidic solution, the reduction current occurs at a slightly more positive potential. It is located at  $-477$  mV without additives.

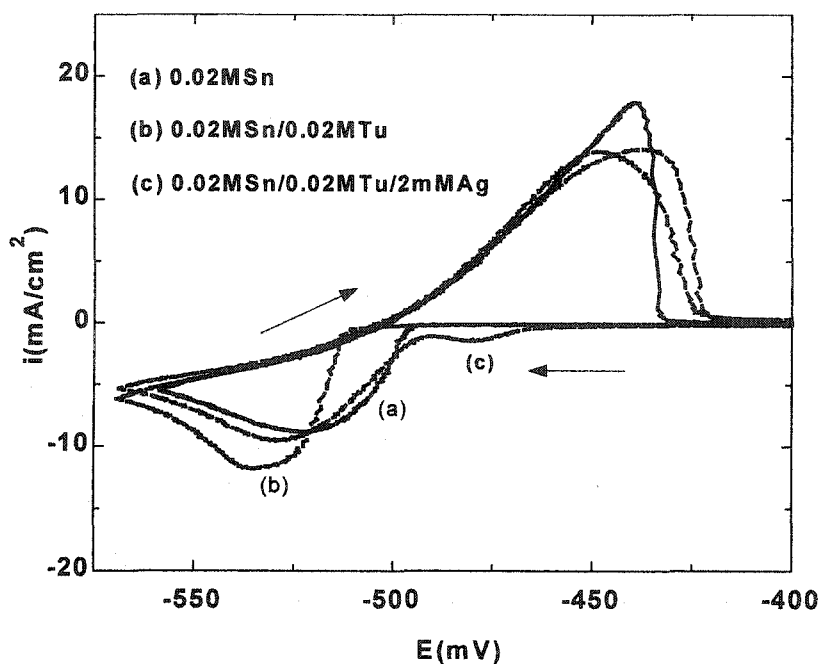


Figure 4.1 Cyclic voltammograms of tin electrodeposition on single crystal copper in: (a) 0.02M SnSO<sub>4</sub> /1.0M H<sub>2</sub>SO<sub>4</sub>, (b) 0.02M SnSO<sub>4</sub> /1.0M H<sub>2</sub>SO<sub>4</sub> /0.02M Tu, (c) 0.02M SnSO<sub>4</sub> /1.0M H<sub>2</sub>SO<sub>4</sub> /0.02M Tu /2mM AgNO<sub>3</sub>. All at a sweep rate of 40 mV/s.

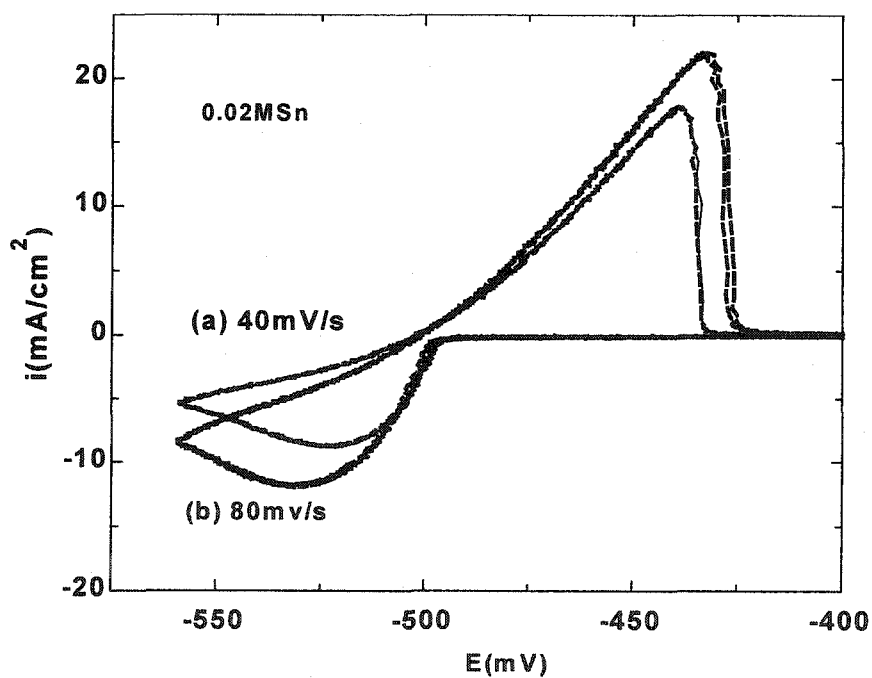


Figure 4.2 The fifth and tenth cyclic voltammograms of tin electrodeposition on single crystal copper in 0.02M SnSO<sub>4</sub> /1.0M H<sub>2</sub>SO<sub>4</sub> solution. The scan rate: (a) 40, (b) 80 mV/s.

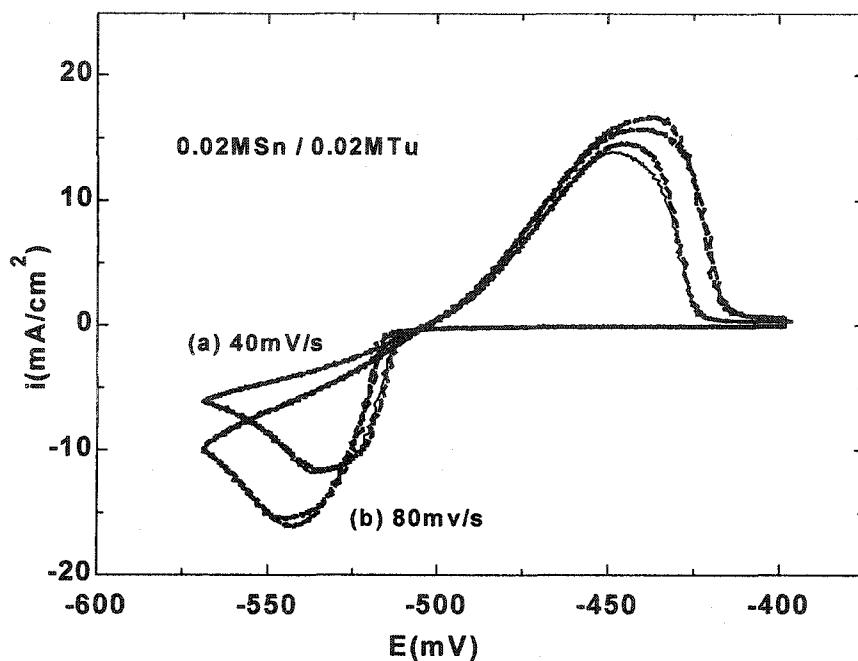


Figure 4.3 The fifth and tenth cyclic voltammograms of tin electrodeposition on single crystal copper in 0.02M SnSO<sub>4</sub> /1.0M H<sub>2</sub>SO<sub>4</sub> /0.02M Tu solution. The scan rate: (a) 40 mV/s, (b) 80 mV/s.

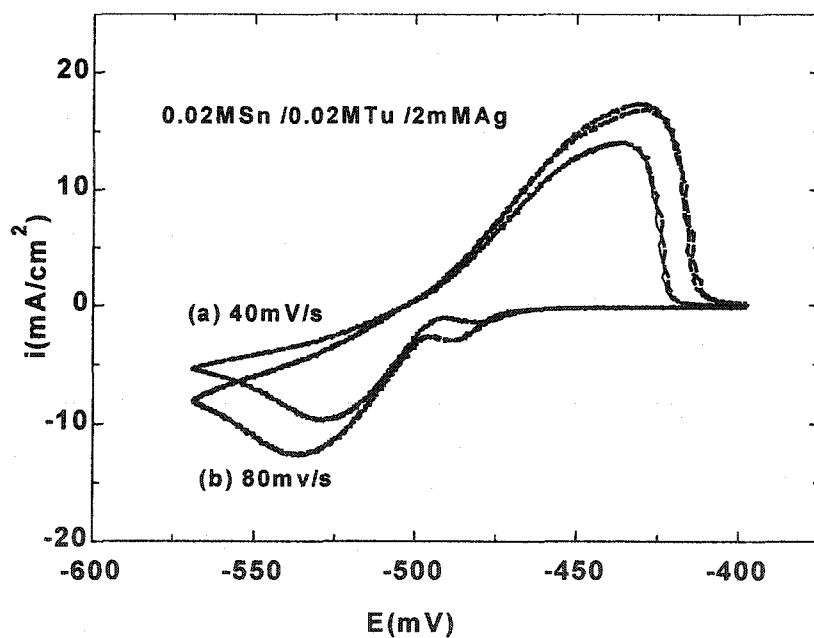


Figure 4.4 The fifth and tenth cyclic voltammograms of tin electrodeposition on single crystal copper in 0.02M SnSO<sub>4</sub> /1.0M H<sub>2</sub>SO<sub>4</sub> /0.02M Tu /2mM AgNO<sub>3</sub> solution. The scan rate: (a) 40 mV/s, (b) 80 mV/s.

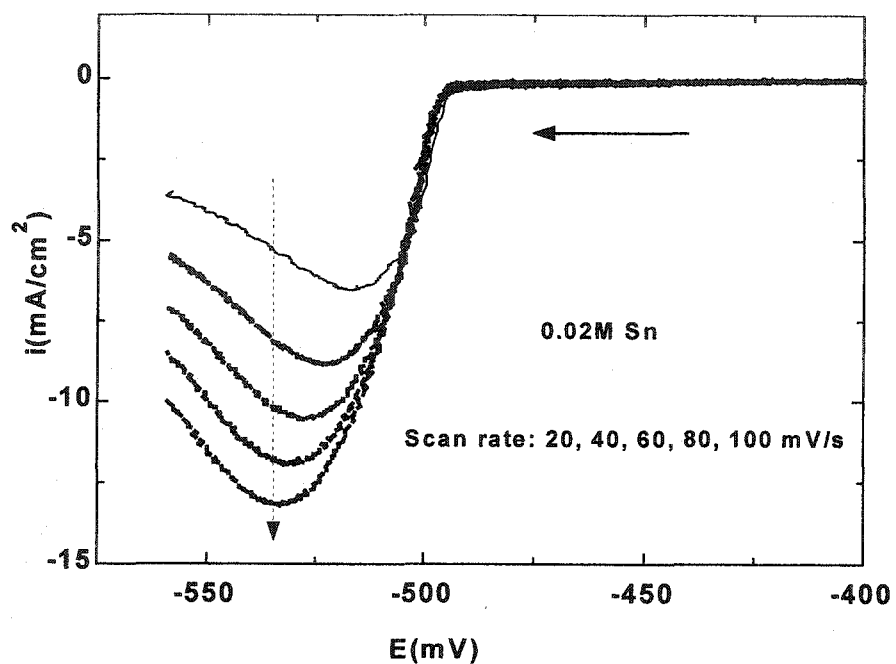


Figure 4.5 Cyclic voltammograms of tin electrodeposition on single crystal copper in 0.02M SnSO<sub>4</sub> / 1.0M H<sub>2</sub>SO<sub>4</sub> solution. The scan rate from 20 to 100 mV/s.

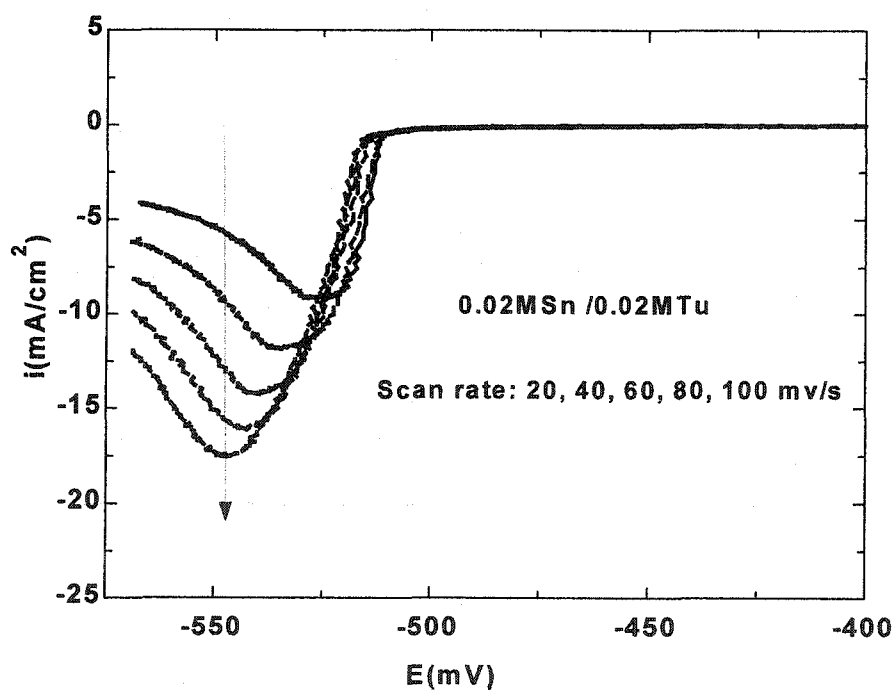


Figure 4.6 Cyclic voltammograms of tin electrodeposition on single crystal copper in 0.02M SnSO<sub>4</sub> / 1.0M H<sub>2</sub>SO<sub>4</sub> / 0.02M Tu solution. The scan rate from 20 to 100 mV/s.

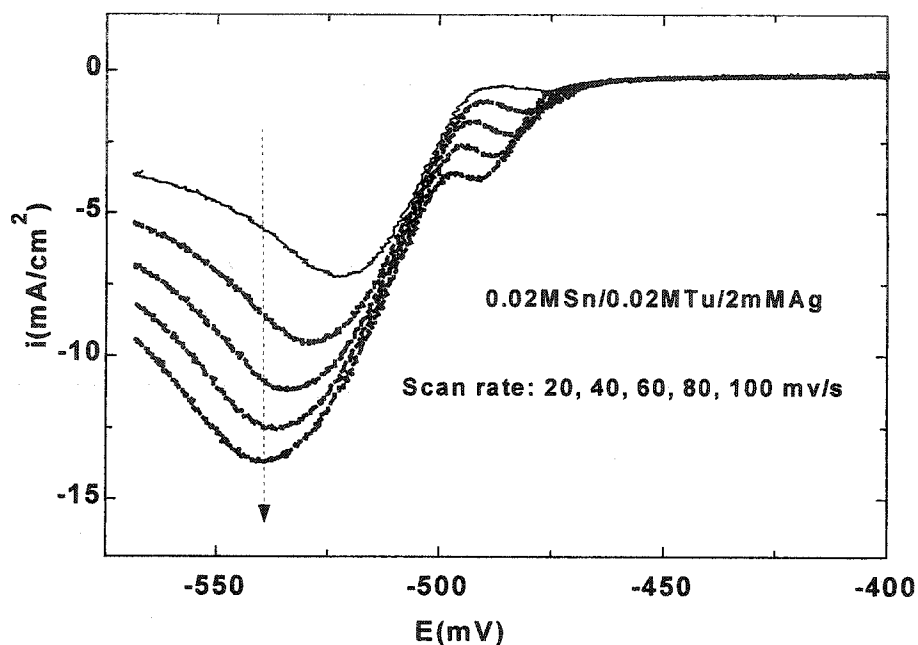


Figure 4.7 Cyclic voltammograms of tin electrodeposition on single crystal copper in  $0.02\text{M SnSO}_4 / 1.0\text{M H}_2\text{SO}_4 / 0.02\text{M Tu} / 2\text{mM AgNO}_3$  solution. The scan rate from 20 to 100  $\text{mV}/\text{s}$ .

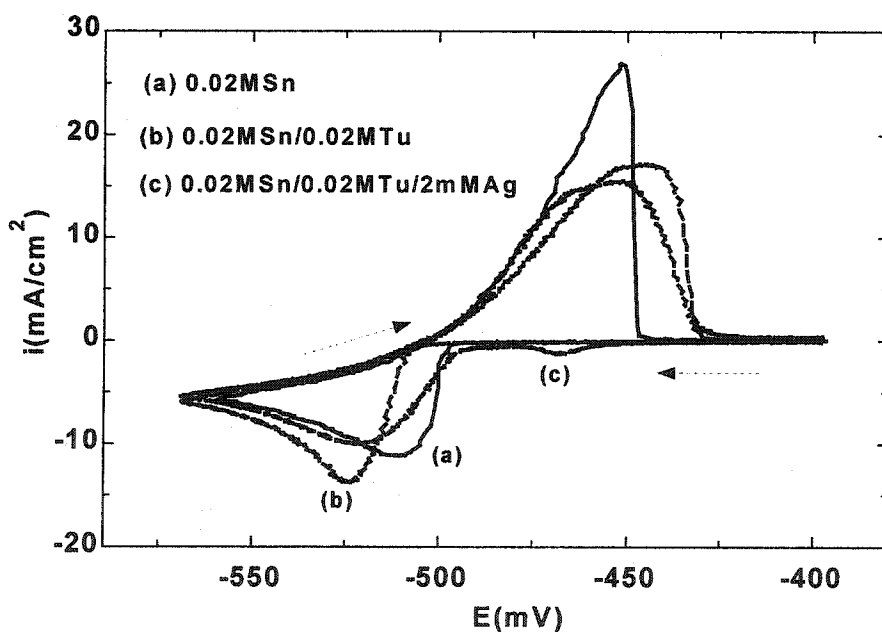


Figure 4.8 Cyclic voltammograms of tin electrodeposition on bright polycrystalline copper in (a)  $0.02\text{M SnSO}_4 / 1.0\text{M H}_2\text{SO}_4$ , (b)  $0.02\text{M SnSO}_4 / 1.0\text{M H}_2\text{SO}_4 / 0.02\text{M Tu}$ , (c)  $0.02\text{M SnSO}_4 / 1.0\text{M H}_2\text{SO}_4 / 0.02\text{M Tu} / 2\text{mM AgNO}_3$ . All at the sweep rate of 40  $\text{mV}/\text{s}$ .

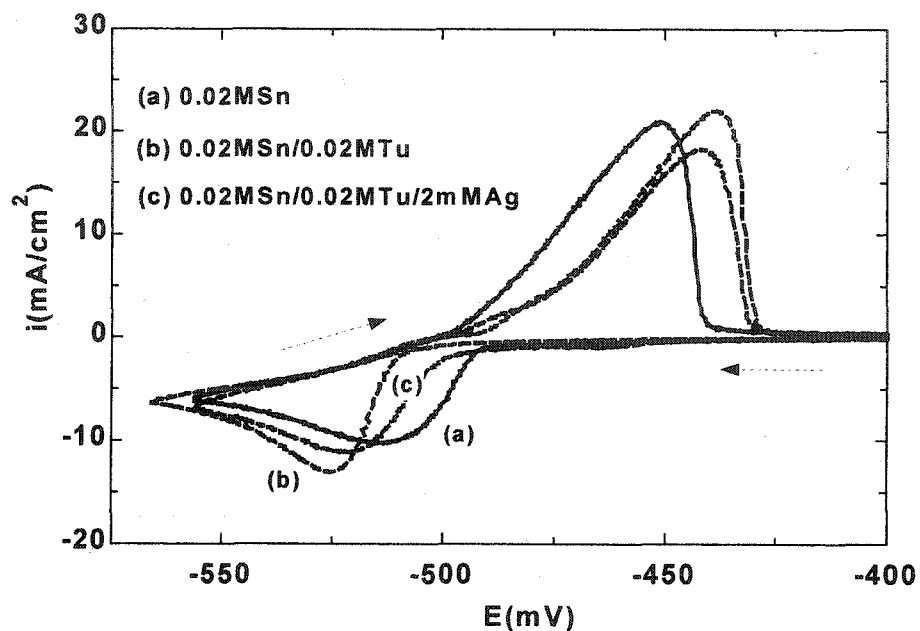


Figure 4.9 Cyclic voltammograms of tin electrodeposition on polycrystalline nickel in (a) 0.02M SnSO<sub>4</sub> /1.0M H<sub>2</sub>SO<sub>4</sub>, (b) 0.02M SnSO<sub>4</sub> /1.0M H<sub>2</sub>SO<sub>4</sub> /0.02M Tu, (c) 0.02M SnSO<sub>4</sub> /1.0M H<sub>2</sub>SO<sub>4</sub> /0.02M Tu /2mM AgNO<sub>3</sub>. All at the sweep rate of 40 mV/s.

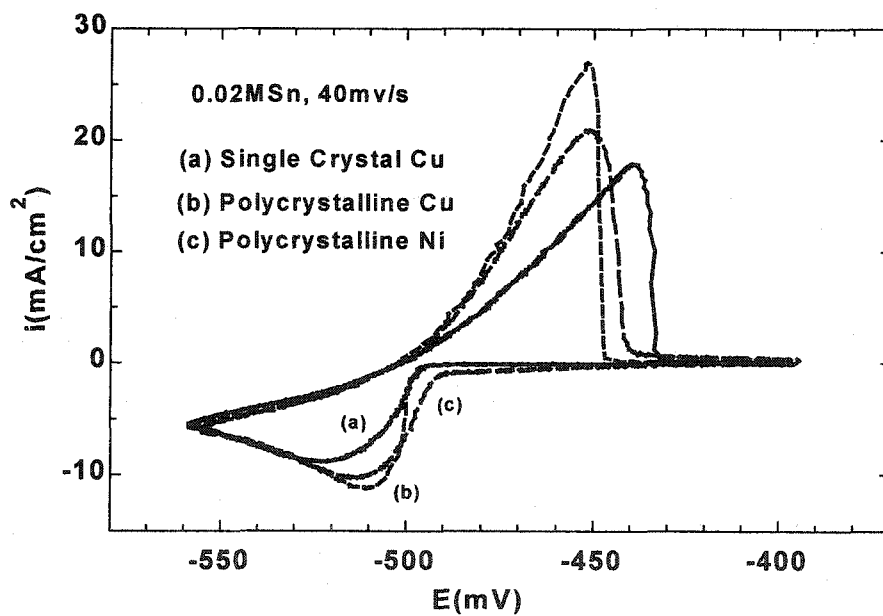


Figure 4.10 Cyclic voltammograms in 0.02M SnSO<sub>4</sub> /1.0M H<sub>2</sub>SO<sub>4</sub> solution at scan rate of 40 mV/s. The working electrodes are (a) Single crystal copper, (b) polycrystalline copper, (c) polycrystalline nickel.

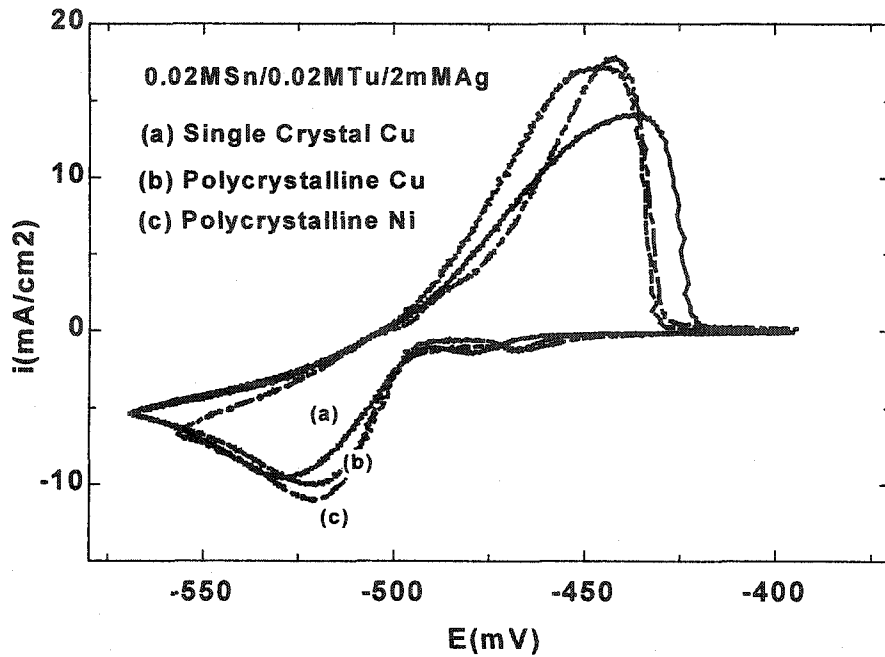


Figure 4.11 Cyclic voltammograms in 0.02M SnSO<sub>4</sub> /1.0M H<sub>2</sub>SO<sub>4</sub> /0.02M Tu /2mMAgNO<sub>3</sub> solution at scan rate of 40 mV/s. The working electrodes are (a) Single crystal copper, (b) polycrystalline copper, (c) polycrystalline nickel.

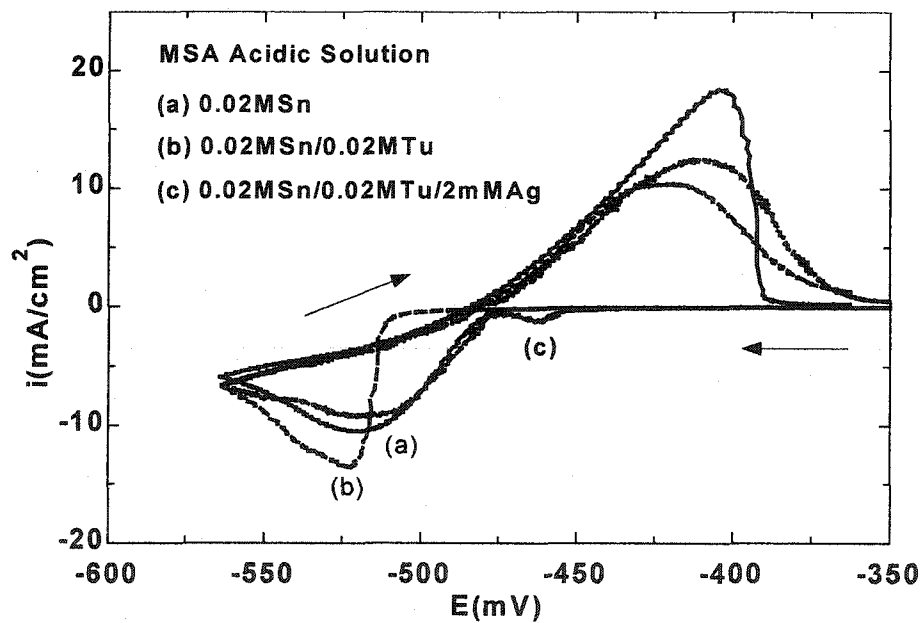


Figure 4.12 Cyclic voltammograms of tin electrodeposition on a single crystal copper in various solutions: (a) 0.02M SnMS /1.0M MSA, (b) 0.02M SnMS /1.0M MSA /0.02M Tu, (c) 0.02M SnMS /1.0M MSA /0.02M Tu /2mMAgMS. All at a scan rate of 40 mV/s.



## 4.1.2 Diffusion Coefficient Measurement

The diffusion coefficient of  $\text{Sn}^{2+}$  in acidic solution with or without additives was determined with the Cottrell equation and with the Randles –Sevcik equation. Potential step experiments to a diffusion-controlled region provide a means of measuring the diffusion coefficient for the  $\text{Sn}^{2+}$  species. In a planar electrode and a motionless solution system, the concentration profile of  $\text{Sn}^{2+}$  is expressed by the linear diffusion equation

$$\frac{\partial C}{\partial t} = D \frac{\partial^2 C}{\partial x^2} \quad (4.1)$$

Based on mass balance, the reaction rate is expressed as

$$r_A = \frac{i(t)}{nFA} = D \left[ \frac{\partial C}{\partial x} \right]_{x=0} \quad (4.2)$$

These equations can be solved to yield

$$i_d = \frac{zFSD^{1/2}C_b}{\pi^{1/2}t^{1/2}} \quad (4.3)$$

where  $z$  is the number of electrons transferred,  $F$  is Faraday's constant (96486 Coulomb / mole),  $S$  is the surface area of the electrode ( $\text{cm}^2$ ), and  $C_b$  and  $D$  are the bulk concentration ( $\text{mol}/\text{cm}^3$ ) and diffusion coefficient ( $\text{cm}^2/\text{s}$ ) of the depositing metal ions.

Equation (4.3) is known as the Cottrell equation. Under diffusion control, there is a linear relationship between the current and the reciprocal of the square root of time. A plot of  $i$  versus  $t^{-1/2}$  is often referred to as the Cottrell plot. For the transient current in the mass transfer control region, the Cottrell plot yields a straight line. The diffusion coefficient for the  $\text{Sn}^{2+}$  species can be calculated from the slope as shown in Table 4-2. Figure 4.13 shows current curves for different electrolyte solutions, and Figure 4.14

illustrates Cottrell plots for these solutions. The linearity of the plots confirms that the reduction process of  $\text{Sn}^{2+}$  was diffusion controlled.

The linear sweep voltammogram provides another way to estimate the diffusion coefficient of the electroactive  $\text{Sn}^{2+}$  species. In a reversible process, the maximum cathodic current or cathodic peak current is described by the Randles-Sevcik equation

$$i_p = 0.4463zFSC_b \left( \frac{nF}{RT} \right)^{1/2} v^{1/2} D^{1/2} \quad (4.4)$$

where  $v$  is scan rate (v/s).

This equation predicts that the peak current should be proportional to the square root of the sweep rate under reversible electrochemical reaction. The plot of peak current versus the square root of sweep rate yields a straight line. The diffusion coefficient of the electroactive  $\text{Sn}^{2+}$  species is obtained from the slope of the Randle-Sevcik equation as shown in Table 4-2. The value of the diffusion coefficient for  $\text{Sn}^{2+}$  in the solution with thiourea is a little higher. Figure 4.5 to 4.7 present a series of voltammograms in different electrolyte solutions, and Figure 4.15 illustrates Randle-Sevcik plots for these solutions. The value of the diffusion coefficient for  $\text{Sn}^{2+}$  is in good agreement with values reported by Tzeng<sup>[18]</sup>.

Table 4-2 The apparent diffusion coefficient of  $\text{Sn}^{2+}$  in different electrolyte solutions

Tin Solution	Additives	Diffusion Coefficient ( $\text{cm}^2 \text{s}^{-1}$ )	
		Cottrell equation	Randle-Sevcik Equation
Sulfuric acid	No additives	$6.19 \times 10^{-6}$	$5.78 \times 10^{-6}$
	With Tu	$6.68 \times 10^{-6}$	$7.69 \times 10^{-6}$
	With Tu & Ag	$6.42 \times 10^{-6}$	$5.68 \times 10^{-6}$

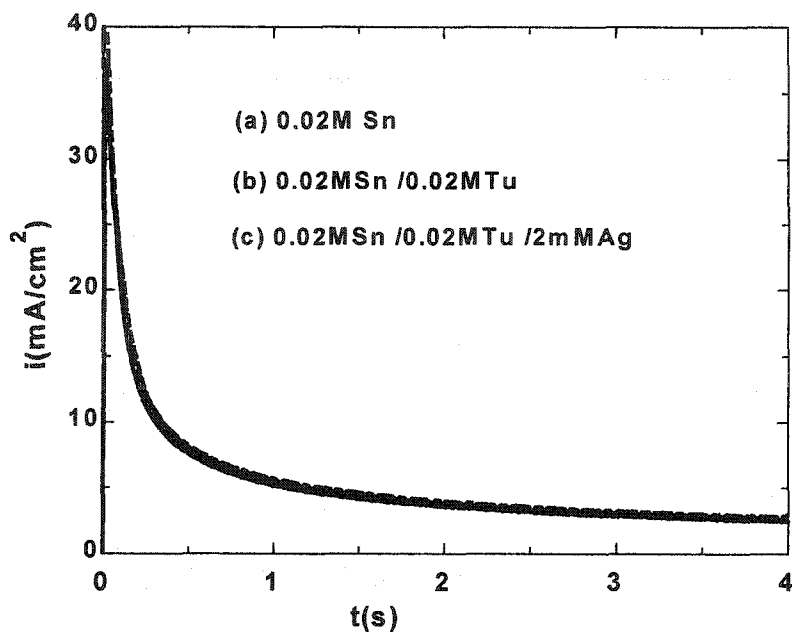


Figure 4.13 Current transients for tin electrodeposition on single crystal copper in various solutions. (a) 0.02M SnSO<sub>4</sub> /1.0M H<sub>2</sub>SO<sub>4</sub>, (b) 0.02M SnSO<sub>4</sub> /1.0M H<sub>2</sub>SO<sub>4</sub> /0.02M Tu, (c) 0.02M SnSO<sub>4</sub> /1.0M H<sub>2</sub>SO<sub>4</sub> /0.02M Tu /2mMAgNO<sub>3</sub>. The potential was -580 mV.

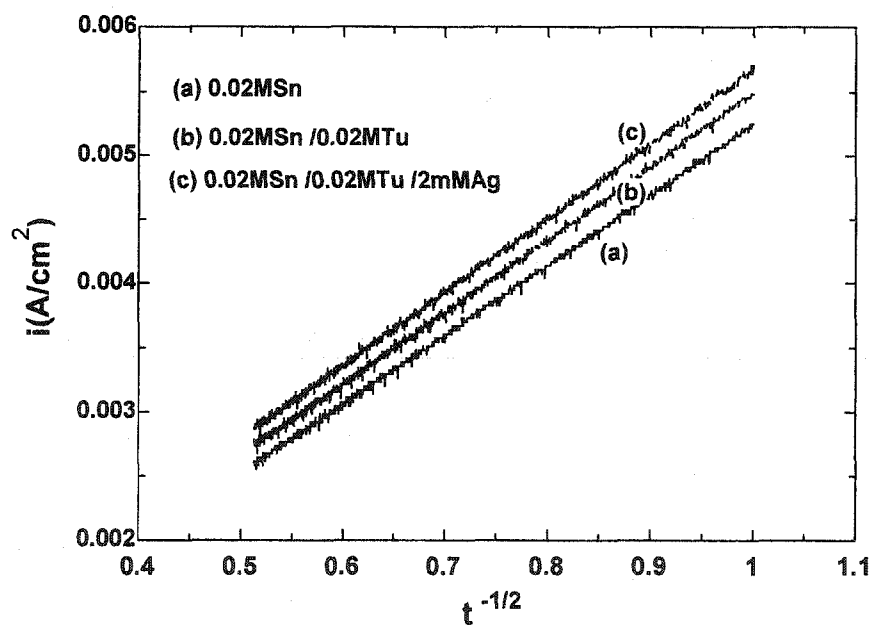


Figure 4.14 Cottrell plots for tin electrodeposition on single crystal copper in various solutions. (a) 0.02M SnSO<sub>4</sub> /1.0M H<sub>2</sub>SO<sub>4</sub>, (b) 0.02M SnSO<sub>4</sub> /1.0M H<sub>2</sub>SO<sub>4</sub> /0.02M Tu, (c) 0.02M SnSO<sub>4</sub> /1.0M H<sub>2</sub>SO<sub>4</sub> /0.02M Tu /2mMAgNO<sub>3</sub>

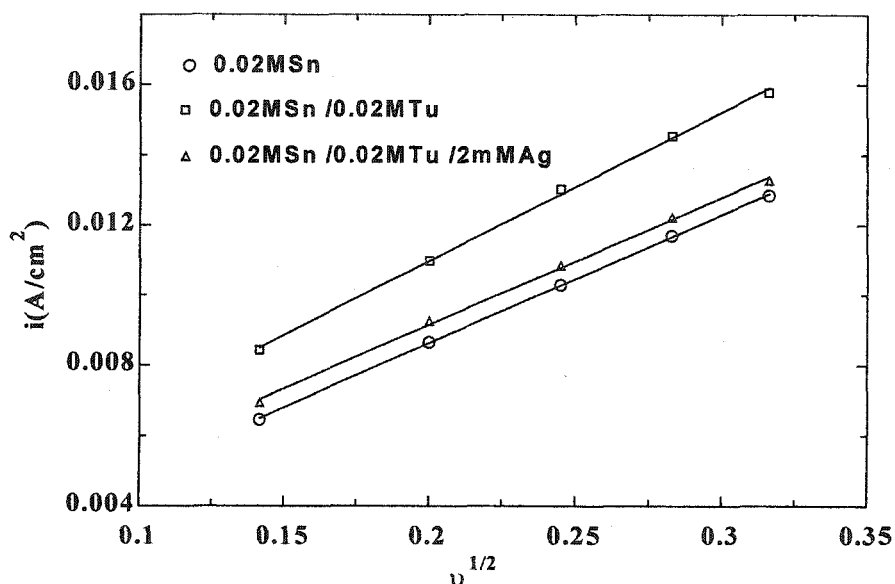


Figure 4.15 Randle-Sevcik plots for tin electrodeposition on single crystal copper in various solutions: (a) 0.02M SnSO<sub>4</sub> /1.0M H<sub>2</sub>SO<sub>4</sub>, (b) 0.02M SnSO<sub>4</sub> /1.0M H<sub>2</sub>SO<sub>4</sub> /0.02M Tu, (c) 0.02M SnSO<sub>4</sub> /1.0M H<sub>2</sub>SO<sub>4</sub> /0.02M Tu /2mMAgNO<sub>3</sub>. The scan rate from 20 to 100 mV/s

### 4.1.3 Potential Step Measurement (Chronoamperometry)

One fundamental process in electrodeposition is the initial stage of phase formation, usually called electrocrystallization. Chronoamperometry is commonly used to study the electrochemical nucleation mechanism of metal and alloy electrodeposition. Based on the transients, Scharifker and Mostany<sup>[86]</sup> derived mathematical models that describe the nucleation mechanisms. The nucleation mechanism has two limiting forms: (a) instantaneous nucleation, when all nuclei are formed immediately after the application of an overpotential, or (b) progressive nucleation, when the nuclei are formed in a continuous fashion following first order kinetics after the potential step.

In chronoamperometry experiments, the potential is stepped from the open circuit potential to a potential at which the deposition of tin or tin-silver alloy occurs. The current rises instantaneously after the potential jump as nuclei are formed, and then decays as a function of time until the transient current reaches a steady state value where diffusion is the rate limiting process. The steady state current transient can be described by the Cottrell Equation. Using nucleation theory, the number density of active sites ( $N_0$ ), the nucleation rate constant ( $A$ ), the critical Gibbs free energy ( $\Delta G_{crit}$ ) and the number of atoms ( $n_{crit}$ ) forming critical nucleus are obtained from the current transients.

#### **4.1.3.1 Tin Electrodeposition in 0.02M SnSO<sub>4</sub> /1.0M H<sub>2</sub>SO<sub>4</sub> Solution**

##### **A). Nucleation rate constant and the number density of active sites**

A family of current transients obtained at different potentials during tin electrodeposition on single and polycrystalline copper substrates and polycrystalline nickel substrate are shown in Figure 4.16 to 4.18, respectively. In all cases, the electrode potential was stepped from  $-465$  mV to a final value in the range  $-545$  to  $-580$  mV. The holding time at the initial potential ( $-465$  mV) was 30s. In the case of polycrystalline nickel substrate, Figure 4.18 shows that no maximum currents are observed. The current density and time maxima are indicative of electrochemical growth of a solid phase [19]. Therefore, the process occurring at polycrystalline nickel electrode from additive-free tin solution is uniform electrodeposition of tin.

In the cases of single crystal and polycrystalline copper substrates, data follows nucleation-controlled behavior. Initially, the current transients increases as the electroactive area increases, either as each independent nucleus grows in size or the

number of nuclei increases. The transients then decrease as the concentration of reactants is depleted near the electrode surface. For longer times, the transients merge into a common curve which is caused by planar diffusion control and described by the Cottrell equation.

The characteristic parameters obtained from these current transients are presented in Table 4-3. The variations of  $t_{\max}$  and  $I_{\max}$  with the final potential show that the characteristic peaks corresponding to the nucleation and growth process move to shorter times and higher currents as the potential is made more negative. At a given potential, on the single crystal copper substrate  $t_{\max}$  is significantly larger and  $I_{\max}$  is much smaller than those on polycrystalline copper substrate, which indicates a higher nucleation rate on the polycrystalline copper substrate.

Analysis of these transients using the theoretical model proposed by Scharifker and Mostany (SM model) <sup>[86]</sup>, the nucleation parameters of  $A$  (nucleation rate constant) and  $N_0$  (number density of active sites) are obtained and listed in Table 4-4. As can be seen, the two systems have high nucleation rates, and the nucleation rate and number density of active sites on polycrystalline copper are much higher than that on single crystal copper. The value of the diffusion coefficient ( $5.72 \times 10^{-6}$ ) that was obtained during the evaluation of  $A$  and  $N_0$  by SM model is in good agreement with the values reported in section 4.1.2. Based on nucleation theory, this is instantaneous nucleation. All nuclei are formed immediately after the potential step is applied, and their number remains constant during the growth process.

Figure 4.19 shows a comparison of the experimental data and theoretical current transients obtained from the Scharifker and Mostany (SM) model, using the values of 'A'

and 'No' obtained from analysis of the current maxima. From this figure it is clear that SM theoretical model adequately describes the experimental data in both single crystal and polycrystalline copper systems. The calculated transients are in good agreement with the experimental rising part corresponding to nucleation process are obtained, although after the peak current, a deviation from the model in the region controlled by diffusion was observed. This positive deviation may be the result of nuclei projecting into the diffusion layer. The SM model is based on nuclei that are co-planar with the substrate.

Figure 4.20 shows the dependence of the number density of active sites for the nucleation of tin on a single crystal and polycrystalline copper with overpotentials. The number density of nucleation sites strongly depends on the final potential. In both cases, the number density of active sites ( $N_0$ ) increases exponentially as the potential changes to more negative values. The exponential dependence of the nucleus density on potential suggests that thermal activation of nucleation sites is consistent with classical nucleation models. The number of active sites was correlated in a qualitative way with *ex-situ* AFM and SEM analysis in the section 5.1.

Table 4-3 Parameters extracted from the current transients for tin electrodeposition on single crystal and polycrystalline copper substrates.

Potential (mV)	Single Crystal Copper (Cu-S)		Polycrystalline Copper (Cu-P)	
	Max time (ms)	Max current (mA/cm <sup>2</sup> )	Max time (ms)	Max current (mA/cm <sup>2</sup> )
-545	16.95	26.8	4.45	60.7
-550	13.95	29.7	3.70	66.9
-555	11.55	32.9	3.00	72.8
-560	10.20	35.6	2.70	79.2
-565	9.15	38.2	2.25	85.9
-570	7.95	40.9	1.95	92.5
-580	6.75	45.4	1.60	106.6

Table 4-4 Nucleation parameters resulting from Scharifker and Mostany's model for tin electrodeposition on single crystal and polycrystalline copper substrates at  $\alpha = 0.001$ .

Potential (mV)	Single Crystal Copper (Cu-S) ( $\alpha = 0.001$ )		Polycrystalline Copper (Cu-P) ( $\alpha = 0.001$ )	
	$10^{-5}A(1/s)$	$10^{-8}No (1/cm^2)$	$10^{-5}A(1/s)$	$10^{-8}No (1/cm^2)$
-545	0.730	0.511	2.83	1.47
-550	0.902	0.625	3.40	1.75
-555	1.09	0.744	4.20	2.25
-560	1.23	0.816	4.66	2.35
-565	1.38	0.881	5.59	2.88
-570	1.58	1.02	6.46	3.30
-580	1.87	1.15	7.87	3.70



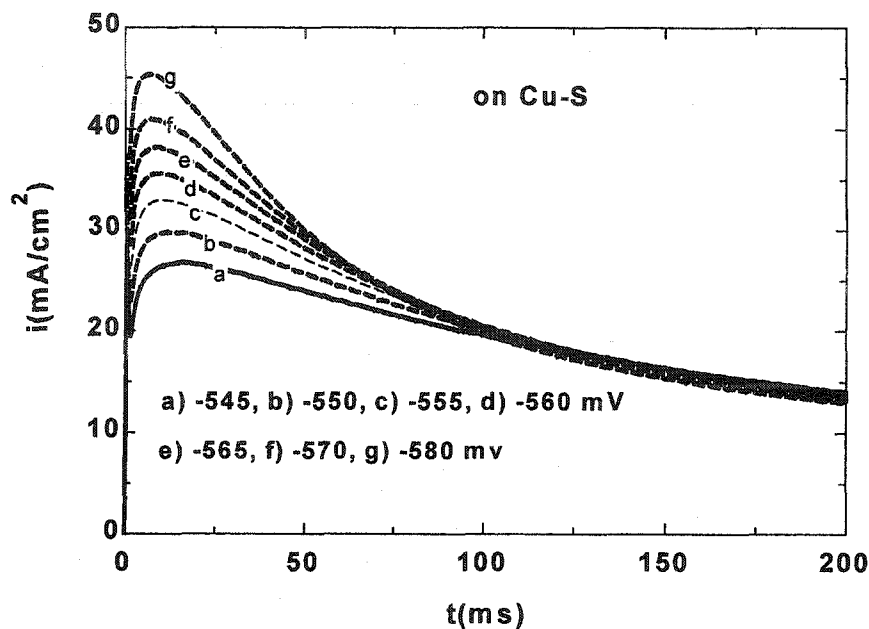


Figure 4.16 Current transients for tin electrodeposition on single crystal copper (Cu-S) substrate at the indicated final potentials in 0.02M SnSO<sub>4</sub>/1.0M H<sub>2</sub>SO<sub>4</sub> solution. The initial potential is -465mV.

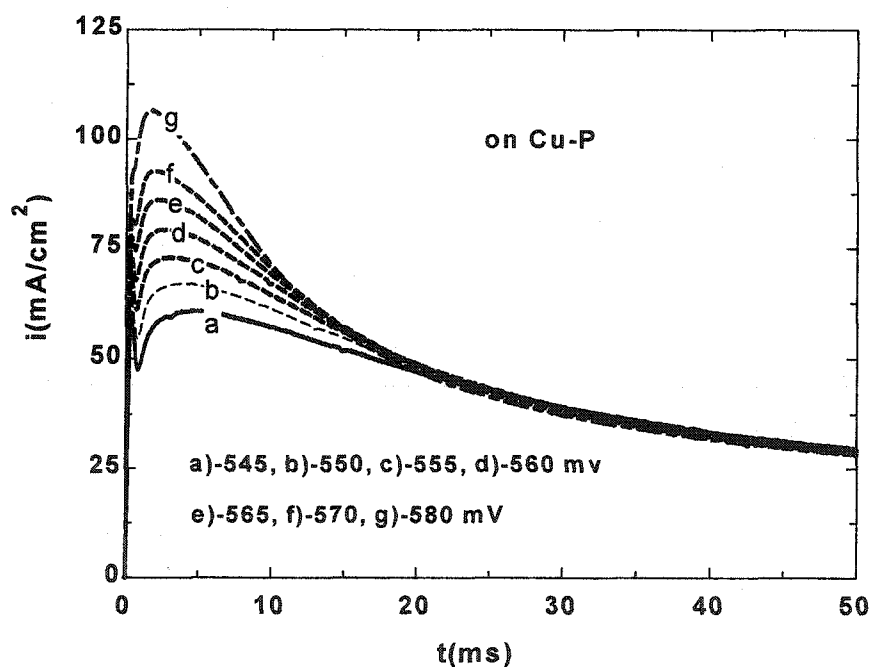


Figure 4.17 Current transients for tin electrodeposition on the polycrystalline copper (Cu-P) substrate at the indicated overpotentials potentials in 0.02M SnSO<sub>4</sub> /1.0M H<sub>2</sub>SO<sub>4</sub> solution. The initial potential is -465mV.

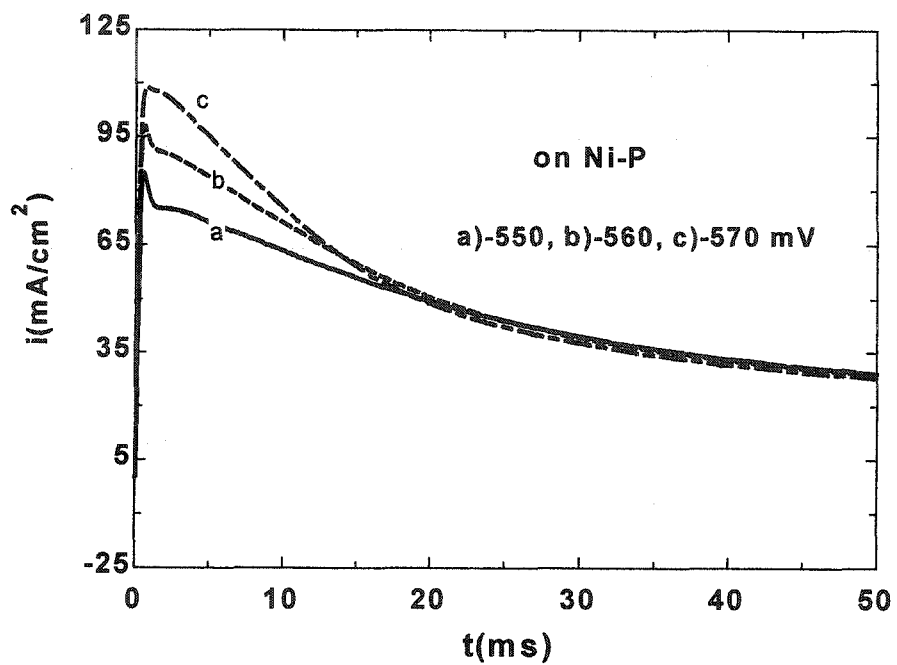


Figure 4.18 Current transients for tin electrodeposition on the polycrystalline nickel (Ni-P) substrate at the indicated overpotentials in 0.02M SnSO<sub>4</sub> /1.0M H<sub>2</sub>SO<sub>4</sub> solution. The initial potential is -465mV.

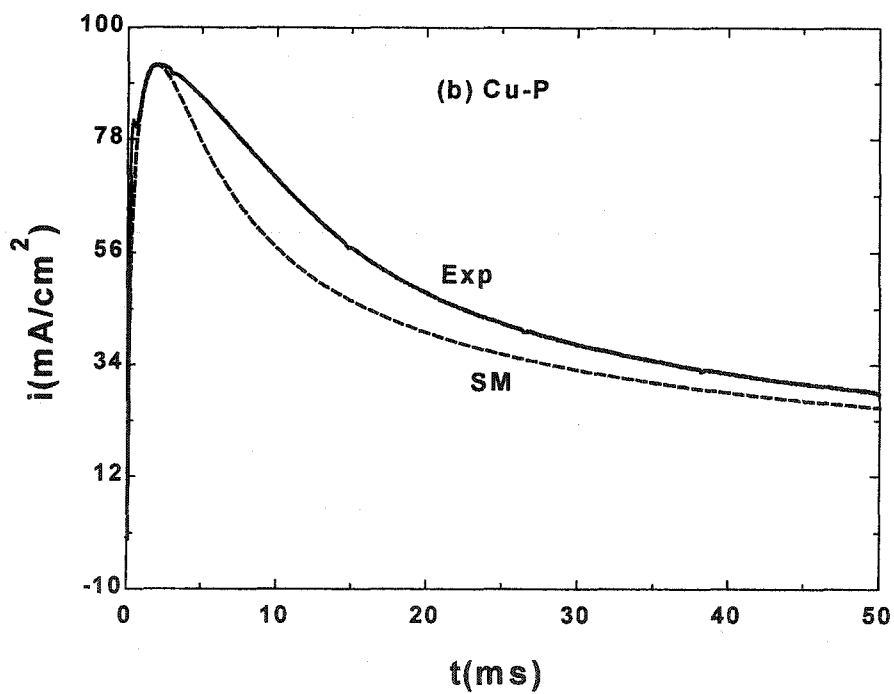
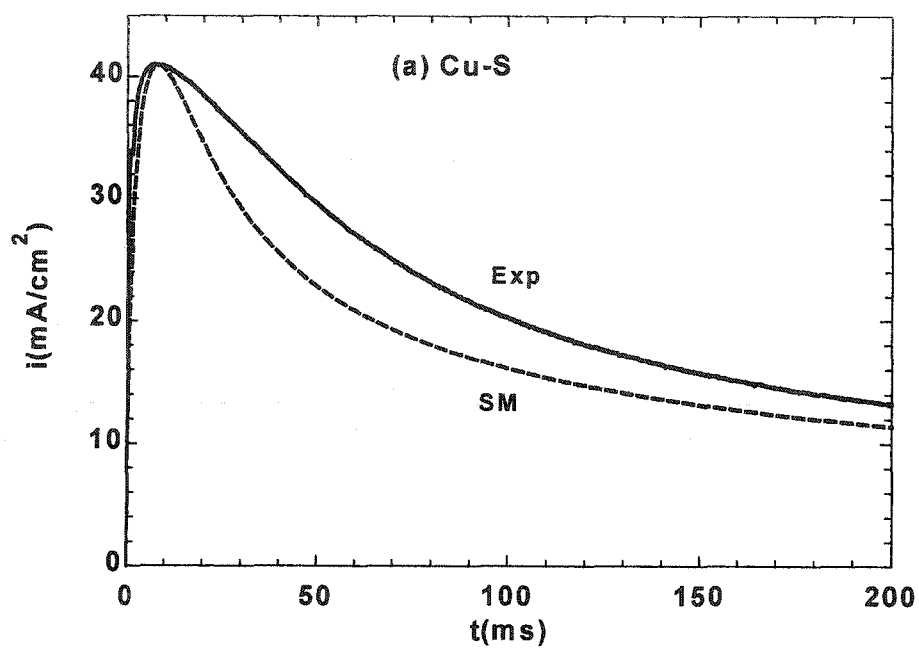


Figure 4.19 Comparison of theoretical (SM line) and experimental (Exp line) current transients. Tin was electrodeposited on: (a) single crystal copper (Cu-S), (b) polycrystalline copper (Cu-P), at  $-570\text{mV}$ .

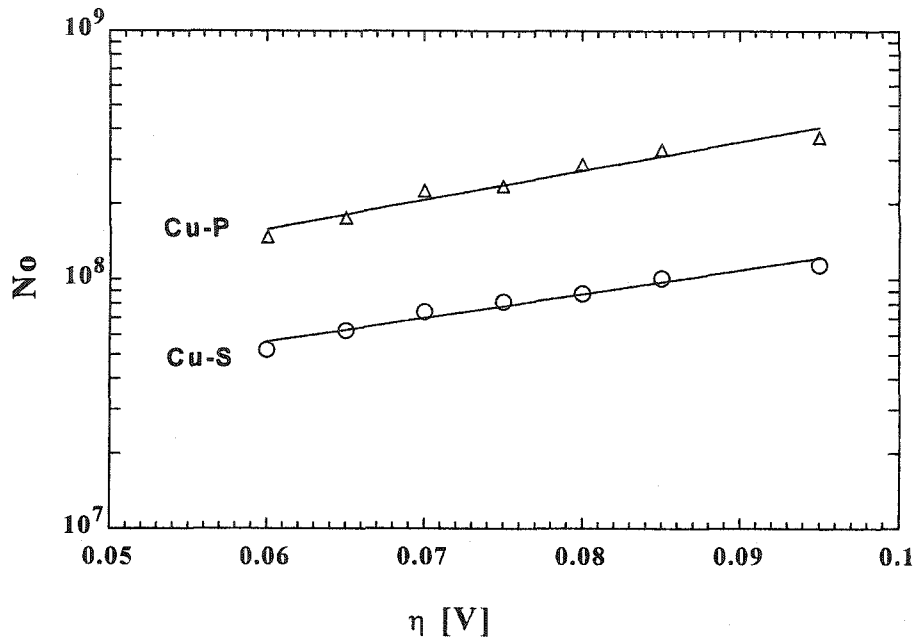


Figure 4.20 Dependence of the number density of active sites ( $N_o$ ) with overpotentials for tin electrodeposition on (a) single crystal copper (Cu-S), (b) polycrystalline copper (Cu-P), in 0.02M  $\text{SnSO}_4$  / 1.0M  $\text{H}_2\text{SO}_4$  solution.

### B). Critical nucleus size

The overpotential dependence of the nucleation rate may be interpreted on the basis of either the classical or the atomistic theory of nucleation. According to the classical theory,

$$J_{st} = K \exp\left(-\frac{4BV_m^2\sigma^3}{27(ze\eta)^2 kT}\right). \quad (2.33)$$

Simplify

$$\ln(AN_o) = -\frac{K'}{\eta^2} + \ln(K). \quad (4.5)$$

On the other hand, the atomistic theory of nucleation yields a straight line in the plot of  $\ln(\text{ANo})$  verse  $\eta$ .

$$J_{st} = A(N_o, n_{crit}) \exp\left(\frac{\beta^* ze \eta}{kT}\right) \exp\left(\frac{n_{crit} ze \eta}{kT}\right). \quad (2.34)$$

The equation (2.34) is simplified to become

$$\ln(\text{AN}_o) = K'' \eta + \ln(A') \quad (4.6)$$

where:  $K'' = \left(\beta^* + n_{crit}\right) \frac{ze}{kT}$ .

Figure 4.21 and 4.22 present the dependence of nucleation rate ( $\text{ANo}$ ) on  $1/\eta^2$  and  $\eta$  on single crystal and polycrystalline copper substrates, respectively. As shown in Figure 4.21, the apparently straight line observed indicates a three-dimensional metal phase formation via nucleation and nucleus growth on both substrates. Based on analysis of the data according to the classical approach, the critical nucleation energy ( $\Delta G_{crit}$ ) and the number of atoms forming the critical nucleus ( $N_{crit}$ ) are obtained and listed in Table 4-5. It is clear that the critical nucleus size consists of 0-2 atoms, both on the single crystal and polycrystalline copper substrate. This suggests that both substrates have nucleation sites with similar activities.

Figure 4.22 illustrates the linear dependence of  $\ln(\text{ANo})$  on  $\eta$ . According to the small cluster model of the atomistic approach, assuming  $\alpha = 0.5$ , the number of atoms in the critical nucleus is 0-2 over the whole range of investigated overpotentials. The critical nucleus sizes obtained from the classical and atomistic theory agree very well.

Table 4-5 Critical Gibbs free energy of 3D nucleation and critical nucleus size for electrodeposition of tin on single crystal and polycrystalline copper substrates based on classical approach.

Overpotential (mV)	Single Crystal Copper (Cu-S)		Polycrystalline Copper (Cu-P)	
	$10^{20}\Delta G_{crit}$ (J)	$N_{crit}$ (atoms)	$10^{20}\Delta G_{crit}$ (J)	$N_{crit}$ (atoms)
60	1.15	1.20	1.34	1.40
65	0.983	0.943	1.14	1.10
70	0.847	0.755	0.987	0.880
75	0.738	0.614	0.859	0.715
80	0.649	0.506	0.755	0.589
85	0.575	0.422	0.669	0.491
95	0.460	0.302	0.536	0.352

The result  $N_{crit} = 0$  is not a rare event in the case of electrochemical nucleation on a foreign substrate. At high overpotentials such a result was obtained also for the nucleation of silver on glassy carbon, copper on palladium and copper on platinum substrate <sup>[116]</sup>, and silver deposition on a boron-dropped diamond (BDD) substrate <sup>[134]</sup>, aluminum on amorphous carbon substrate <sup>[135]</sup>, zinc on polycrystalline tungsten, nickel and glassy carbon substrates <sup>[136]</sup>. In terms of the atomistic theory of phase formation, a “zero atomic” critical nucleus means that the active site itself plays the role of a critical nucleus. The small size of critical nuclei obtained suggests a strong bond energy between tin atoms and the copper substrate. Under the experimental conditions a single adatom or an adatom pair represents a stable cluster which can grow spontaneously.

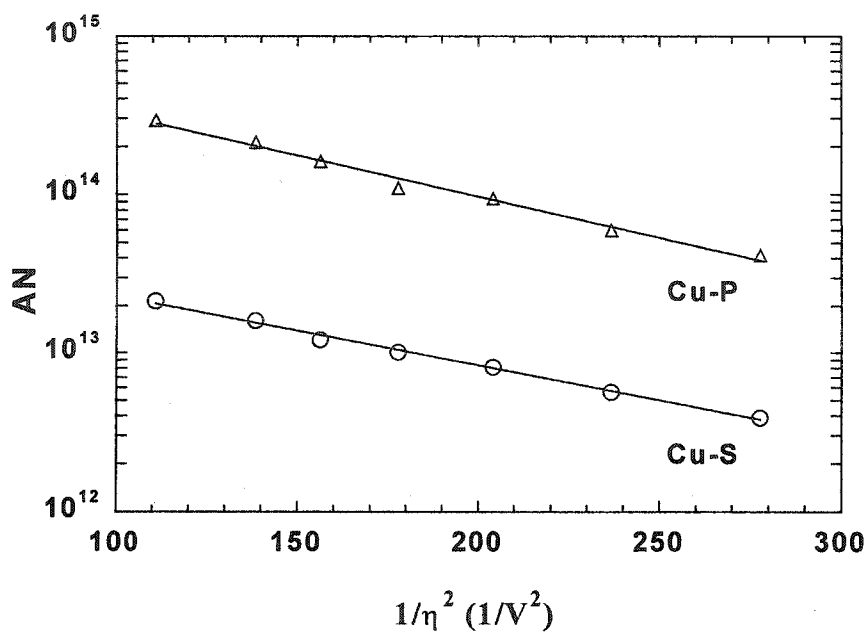


Figure 4.21 Nucleation rate as a function of  $1/\eta^2$  for tin electrodeposition on (a) single crystal copper (Cu-S), (b) polycrystalline copper (Cu-P), in 0.02M SnSO<sub>4</sub> /1.0M H<sub>2</sub>SO<sub>4</sub> solution.

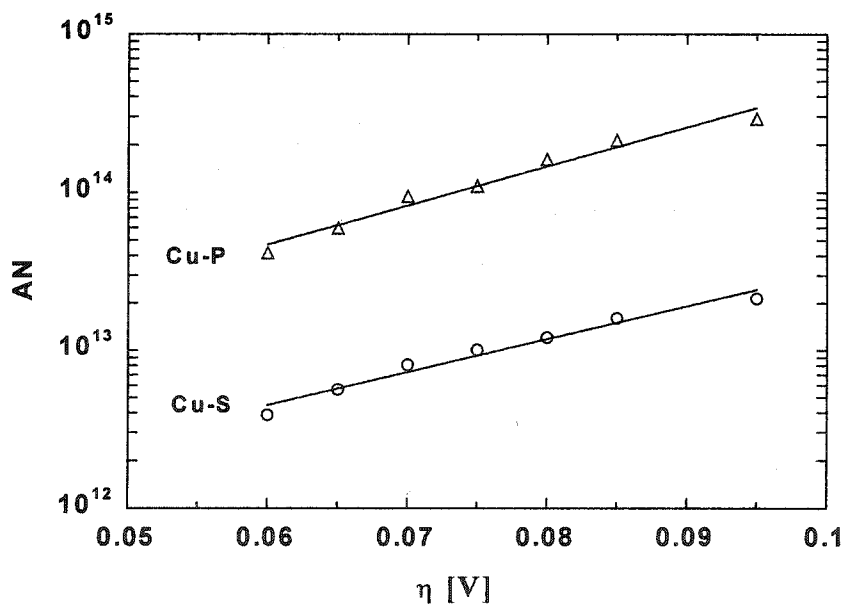


Figure 4.22 Dependence of nucleation rate with overpotentials for tin electrodeposition on (a) single crystal copper (Cu-S), (b) polycrystalline copper (Cu-P), in 0.02M SnSO<sub>4</sub> /1.0M H<sub>2</sub>SO<sub>4</sub> solution.

#### 4.1.3.2 Tin Electrodeposition in 0.02M SnSO<sub>4</sub> / 1.0M H<sub>2</sub>SO<sub>4</sub> / 0.02M Tu

##### Solution

A series of current transients obtained at different potentials during tin electrodeposition on single crystal copper, polycrystalline copper, and polycrystalline nickel substrates are shown in Figure 4.23 to 4.25. In all cases, the transients have the same features. The initial current increases due to nucleation and three-dimensional diffusion-limited growth of isolated nuclei. At longer times the currents decay due to the transition from three-dimensional to one-dimensional diffusion-limited growth. The characteristic parameters (maximum current density and corresponding time) obtained from these transients are presented in Table 4-6. In these cases, the current transients cannot be fitted using the usual nucleation models (such as the SM model) for electrochemical nucleation and diffusion controlled growth, and the interpretation of these results is therefore only qualitative.

As can be seen from these figures, the current transients strongly depend on the final potentials. The transient peak increases and the corresponding time becomes shorter as the potential is made more negative. For deposition on single crystal copper substrate,  $t_{\max}$  is larger and  $i_{\max}$  is smaller than for the other substrate at the same potential. Comparing the values of  $t_{\max}$  and  $i_{\max}$  with those obtained from additive-free tin solution, the current maximum appears at a longer time, and the maximum peak decreases with addition of thiourea. Evidently, nucleation is inhibited by thiourea. It is also noted that the value of  $i_{\max}$  for tin electrodeposition on polycrystalline copper is higher than on polycrystalline nickel. This indicates the electrochemical activity of polycrystalline copper is higher, and the surface has more active sites for nucleation.



Table 4-6 Parameters extracted from the current transients for tin electrodeposition on single crystal and polycrystalline copper, polycrystalline nickel substrates, from 0.02M SnSO<sub>4</sub> /1.0M H<sub>2</sub>SO<sub>4</sub> /0.02M Tu solution.

Potential (mV)	Single Crystal Copper		Polycrystalline Copper		Polycrystalline Nickel	
	t <sub>max</sub> (ms)	i <sub>max</sub> (mA/cm <sup>2</sup> )	t <sub>max</sub> (ms)	i <sub>max</sub> (mA/cm <sup>2</sup> )	t <sub>max</sub> (ms)	i <sub>max</sub> (mA/cm <sup>2</sup> )
-550	56.8	20.6	13.3	48.4	15.6	38.9
-555	48.8	23.2	10.2	52.8	-	-
-560	38.8	26.3	8.4	58.1	12	45.2
-565	33.6	28.6	7.8	64.6	9.8	51.7
-570	27.2	31.1	6.4	69.4	7.5	57.8
-580	21.2	36.9	4.6	80.6	4.9	71.2

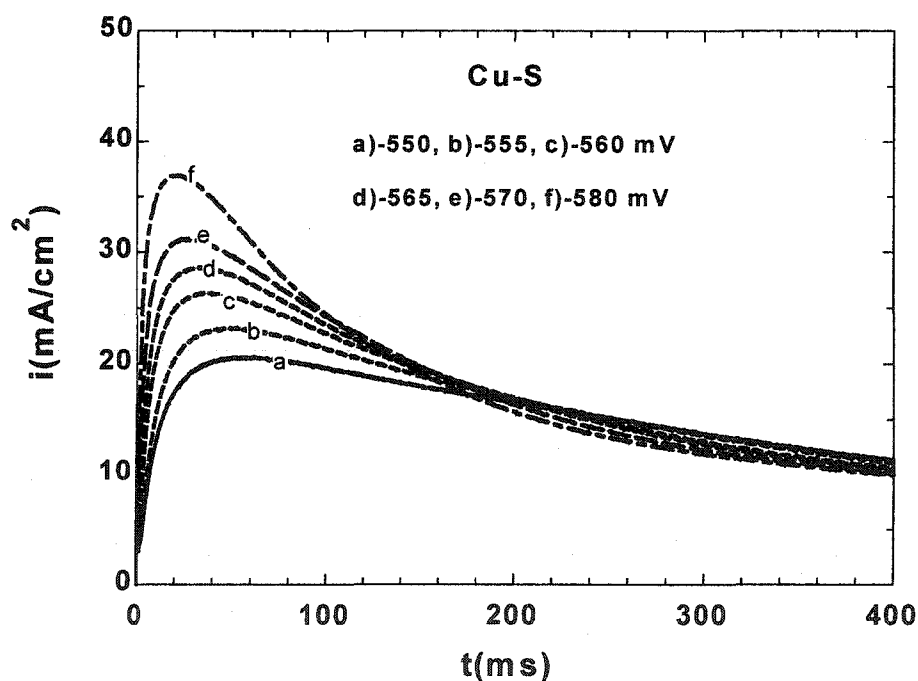


Figure 4.23 Current transients for tin electrodeposition on single crystal copper (Cu-S) in 0.02M SnSO<sub>4</sub> / 1.0M H<sub>2</sub>SO<sub>4</sub> / 0.02MTu Solution at the indicated final potentials. The initial potential is -465mV.

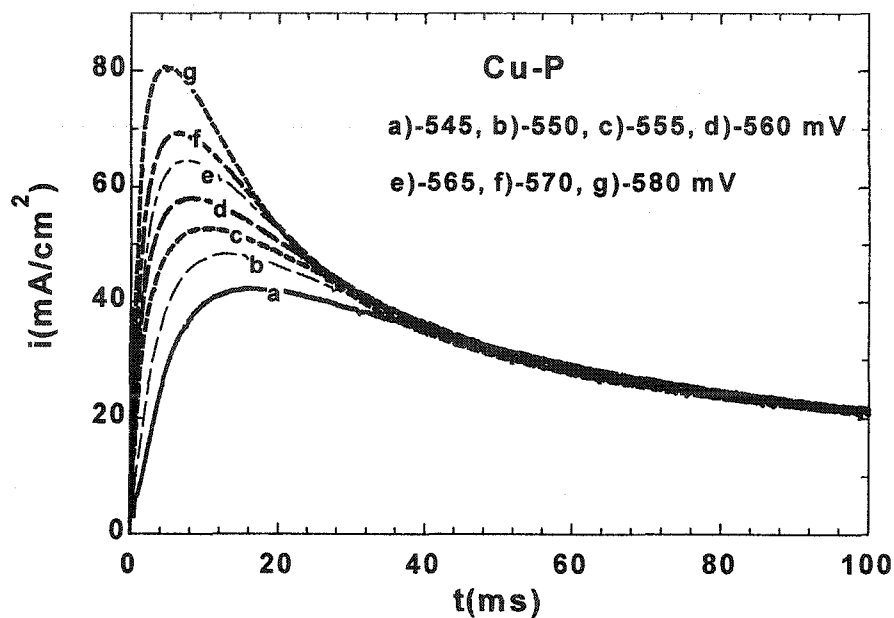


Figure 4.24 Current transients for tin electrodeposition on the polycrystalline copper substrate (Cu-P) in 0.02M SnSO<sub>4</sub> / 1.0M H<sub>2</sub>SO<sub>4</sub> / 0.02MTu Solution at the indicated potentials. The initial potential is -465 mV.

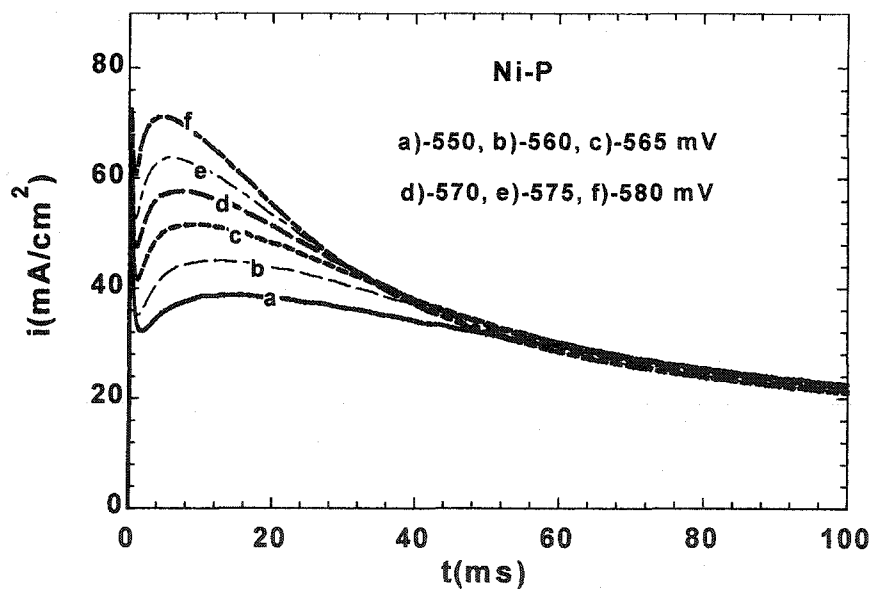


Figure 4.25 Current transients for tin electrodeposition on the polycrystalline nickel substrate (Ni-P) in 0.02M SnSO<sub>4</sub> / 1.0M H<sub>2</sub>SO<sub>4</sub> / 0.02MTu Solution at the indicated potentials. The initial potential is -465 mV.

#### 4.1.3.3 Tin Electrodeposition in 0.02M SnSO<sub>4</sub> /1.0M H<sub>2</sub>SO<sub>4</sub> /0.02M Tu / 2mM AgNO<sub>3</sub> Solution

##### A). Nucleation rate constant and the number density of active sites

A family of typical current transients obtained at different potentials during tin electrodeposition on single crystal, polycrystalline copper, and polycrystalline nickel substrates are shown in Figure 4.26 to 4.28. In the experiments, the potential was stepped from -425 mV, where no deposition is observed, to a final value in the range -545 to -580 mV. The holding time at the initial potential (-425 mV) was 30s. In all cases, the transients exhibit maximum currents which indicate new phase formation by multiple nucleation with mass transfer controlled growth in the electrodeposition process. The characteristic parameters obtained from these current transients are presented in Table 4-7. The transient peak increases and the corresponding time becomes shorter as the potential is made more negative. For tin deposition on single crystal copper,  $t_{max}$  is larger and  $i_{max}$  is smaller than for the other substrates at the same potential. Comparing values of  $t_{max}$  and  $i_{max}$  with tin acid solution containing thiourea, it is clear that with addition of silver, the current maximum appears at a shorter time, and the maximum peak increases. These values are similar to those obtained from pure tin solution without additives.

Under these conditions, it was not possible to categorize the nucleation mechanism as instantaneous or progressive, since an intermediate behavior was observed at all studied potentials. Quantitative analysis of experimental transients was performed on the basis of the theory developed by Scharifker and Mostany (SM model) <sup>[86]</sup>. The nucleation parameters of A and No are obtained and listed in Table 4-8.

As can be seen, these three systems have high number density of active sites, and the density of tin nuclei deposited on single crystal copper is significantly lower than that deposited on polycrystalline copper or nickel substrates at the same deposition potential. In comparison with  $A$  and  $N_0$  obtained from pure tin solution without additives, in the case of tin solution containing thiourea-silver, the nucleation rate constant ( $A$ ) is significantly smaller, but the number density of active nucleation sites is much higher.

Figure 4.29 shows a comparison of the experimental data and theoretical current transients obtained from the SM model for the three cases, using the values of  $A$ ,  $N_0$  and  $D$  obtained from analysis of the current maxima. There is good agreement between the calculated and experimental transients for tin deposition on polycrystalline copper and polycrystalline nickel. Agreement is not as good for single crystal copper. Deviation from model in the diffusion-controlled region was observed after the peak current in all cases.

Figure 4.30 shows the dependence of the number density of active sites for tin nucleation on a single crystal, polycrystalline copper, and polycrystalline nickel as a function of overpotential. The number density of active sites strongly depends on the final potential. The nucleus density on polycrystalline copper is much larger than that on single crystal copper, and also higher than that on polycrystalline nickel. As expected, in all cases, the number density of active sites ( $N_0$ ) increases exponentially as the potential changes to more negative values, the same feature as in the pure tin solution without additives.

Table 4-7 Parameters extracted from the current transients for tin electrodeposition on single crystal, polycrystalline copper, and polycrystalline nickel substrates, in 0.02M SnSO<sub>4</sub> /1.0M H<sub>2</sub>SO<sub>4</sub>/0.02M Tu /2mM AgNO<sub>3</sub> solution.

Potential (mV)	Single Crystal Copper		Polycrystalline Copper		Polycrystalline Nickel	
	t <sub>max</sub> (ms)	i <sub>max</sub> (mA/cm <sup>2</sup> )	t <sub>max</sub> (ms)	i <sub>max</sub> (mA/cm <sup>2</sup> )	t <sub>max</sub> (ms)	i <sub>max</sub> (mA/cm <sup>2</sup> )
-545	-	-	-	-	4.60	62.1
-550	15.60	32.7	3.20	80.5	3.80	67.9
-555	13.65	35.5	2.80	89.5	3.10	74.5
-560	11.70	38.4	2.40	98.2	2.70	81.1
-565	10.05	41.2	2.05	106.2	2.40	87.7
-570	8.15	46.9	1.85	115.9	2.15	90.4
-580	6.60	52.5	1.65	124.6	1.80	97.9

Table 4-8 Nucleation parameters resulting from SM model at  $\alpha = 0.5$  for tin electrodeposition on single crystal, polycrystalline copper, and polycrystalline nickel substrates, in 0.02M SnSO<sub>4</sub> /1.0M H<sub>2</sub>SO<sub>4</sub>/0.02M Tu /2mM AgNO<sub>3</sub> solution.

Potential (mV)	Single Crystal Copper ( $\alpha = 0.5$ )		Polycrystalline Copper ( $\alpha = 5$ )		Polycrystalline Nickel ( $\alpha = 0.2$ )	
	A(1/s)	10 <sup>-8</sup> No (1/cm <sup>2</sup> )	A(1/s)	10 <sup>-8</sup> No (1/cm <sup>2</sup> )	A(1/s)	10 <sup>-8</sup> No (1/cm <sup>2</sup> )
-545	-	-	-	-	1527	2.18
-550	275	0.90	337	10.4	1848	2.66
-555	315	1.00	385	11.0	2265	3.32
-560	367	1.16	449	12.5	2601	3.70
-565	428	1.37	526	14.6	2926	4.00
-570	527	1.61	583	15.0	3266	4.69
-580	651	1.95	654	16.4	3902	5.71

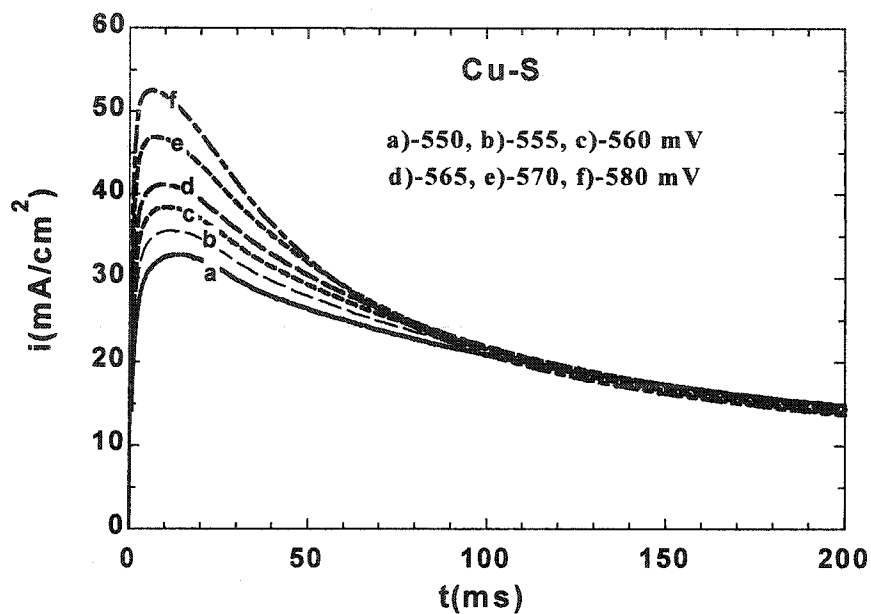


Figure 4.26 Current transients for tin electrodeposition on single crystal copper (Cu-S) in 0.02M SnSO<sub>4</sub> /1.0M H<sub>2</sub>SO<sub>4</sub>/0.02M Tu /2mM AgNO<sub>3</sub> solution at the indicated final potentials. The initial potential is -420 mV.

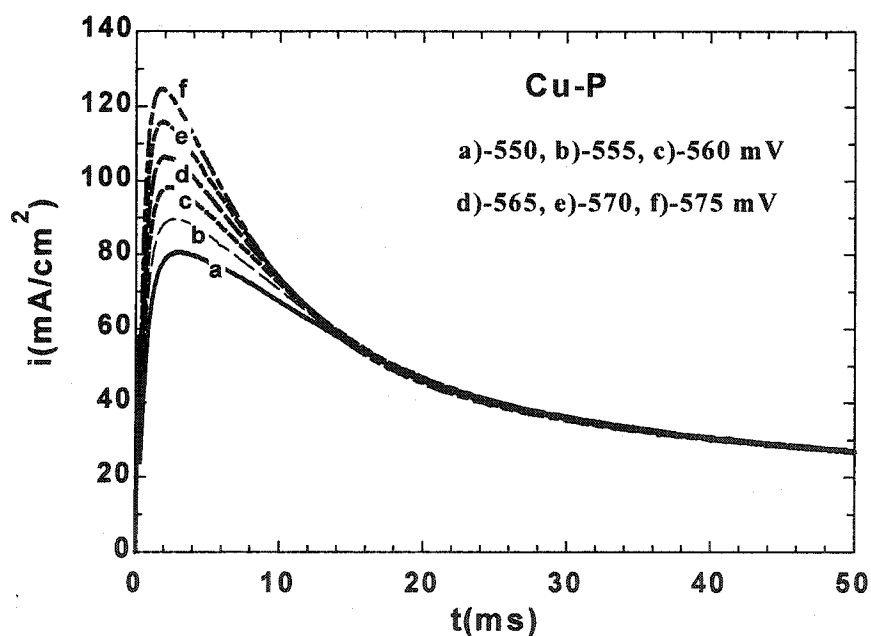


Figure 4.27 Current transients for tin electrodeposition on polycrystalline copper (Cu-P) in 0.02M SnSO<sub>4</sub> /1.0M H<sub>2</sub>SO<sub>4</sub>/0.02M Tu /2mM AgNO<sub>3</sub> solution at the indicated final potentials. The initial potential is -420 mV.

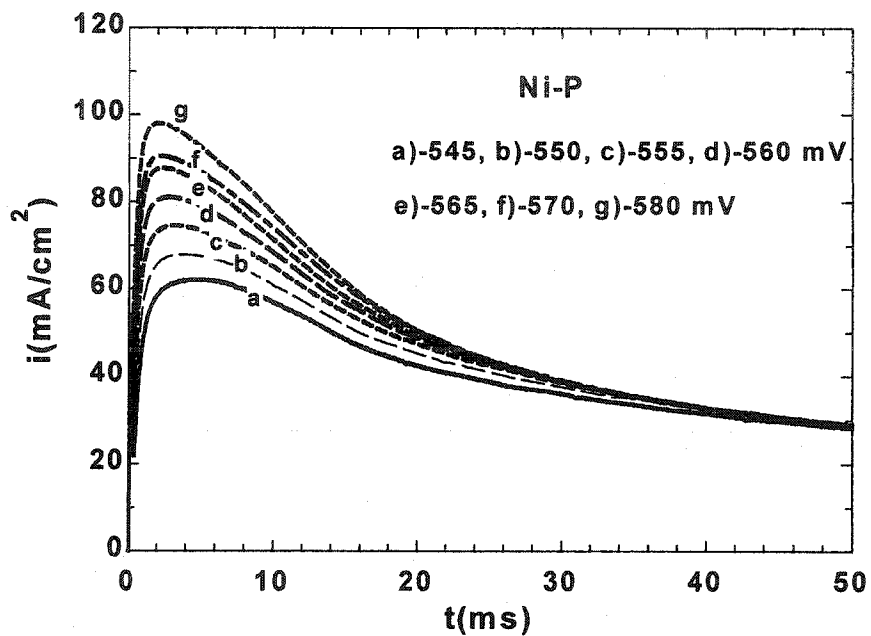


Figure 4.28 Current transients for tin electrodeposition on polycrystalline Nickel (Ni-P) in 0.02M SnSO<sub>4</sub> /1.0M H<sub>2</sub>SO<sub>4</sub>/0.02M Tu /2mM AgNO<sub>3</sub> solution at the indicated final potentials. The initial potential is -420 mV.

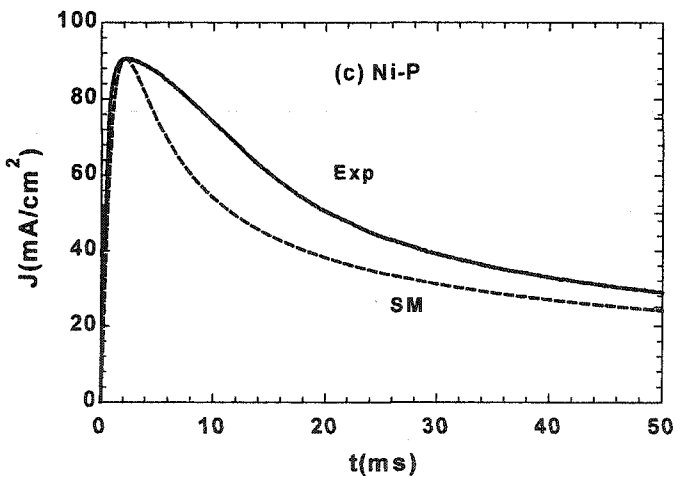
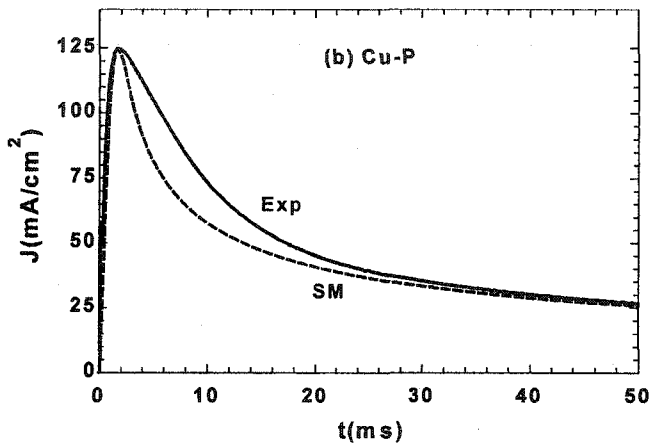
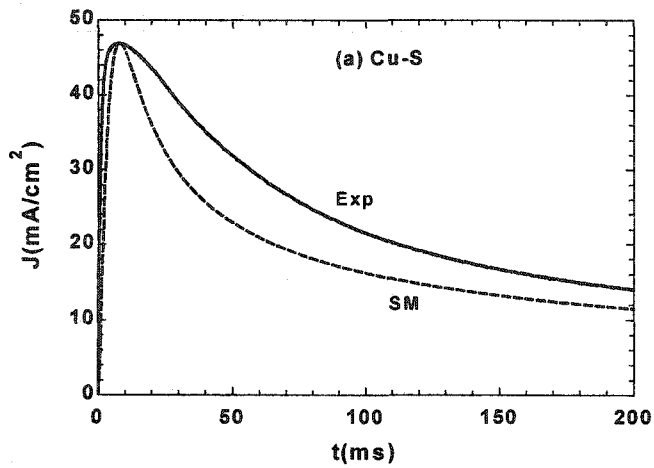


Figure 4.29 Comparison of theoretical (SM line) and experimental (Exp line) transients for tin deposition: (a) single crystal copper (Cu-S), (b) polycrystalline copper (Cu-P), (c) polycrystalline nickel, at  $-570\text{mV}$ , in tin solution with thiourea-silver.



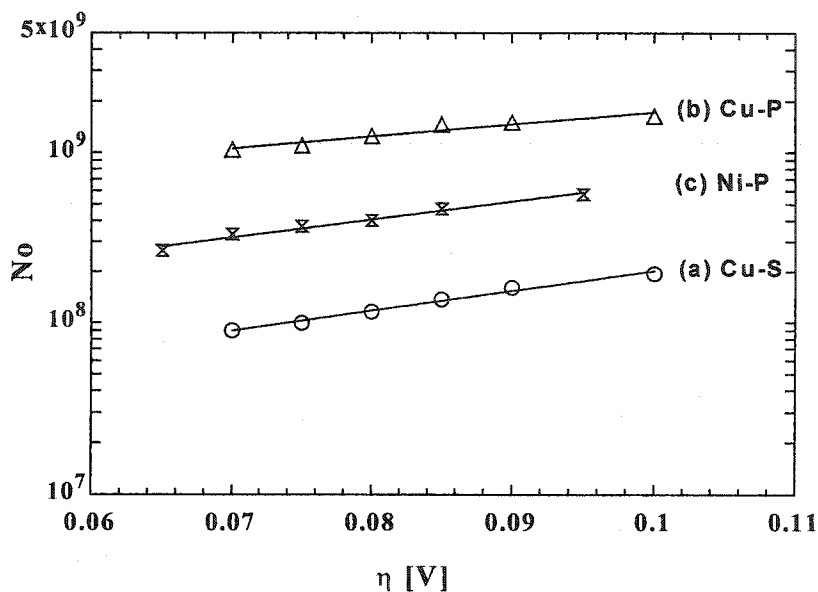


Figure 4.30 Dependence of the number density of active sites with overpotentials for tin electrodeposition on: (a) single crystal copper (Cu-S), (b) polycrystalline copper (Cu-P), (c) polycrystalline nickel (Ni-P), in 0.02M SnSO<sub>4</sub> /1.0M H<sub>2</sub>SO<sub>4</sub> /0.02M Tu /2mM AgNO<sub>3</sub> solution .

### B). Critical nucleus size

The relationship between nucleation rate and  $1/\eta^2$  or  $\eta$  is shown in Figure 4.31 and 4.32 for single crystal copper, polycrystalline copper, and polycrystalline nickel substrates, according to classical theory and atomistic theory of nucleation. As can be seen in Fig 4.31, straight lines are obtained. This indicates that tin electrodeposition proceeds by three-dimensional metal phase formation on these substrates at the initial stage. Analysis of the data according to classical approach (equations 2.22 to 2.26), the critical nucleation energy ( $\Delta G_{crit}$ ) and the number of atoms forming the critical nucleus ( $N_{crit}$ ) are obtained and listed in Table 4-9. It is seen that the critical nucleus size consists

of 0-2 atoms on these three substrates. This suggests that the three substrates have nucleation sites with similar activities.

Figure 4.32 illustrates linear relationship between  $\ln(A\eta)$  and  $\eta$ . According to the atomistic approach, assuming  $\alpha = 0.5$ , the number of atoms in the critical nucleus is 0-2 over the whole range of investigated overpotentials on copper and nickel substrates. The value of critical nucleus size is in very good agreement with the value obtained from classical theory. Comparing the critical nucleus size in Table 4-5 and Table 4-9, similar values are obtained for tin solution systems with and without thiourea-silver, which suggests each active site already acts as a critical nucleus at these substrates.

Table 4-9 Critical Gibbs free energy of 3D nucleation and critical nucleus size for the electrodeposition of tin on single crystal and polycrystalline copper, from 0.02M SnSO<sub>4</sub> /1.0M H<sub>2</sub>SO<sub>4</sub> /0.02M Tu /2mM AgNO<sub>3</sub> solution.

Over-Potential (mV)	Single Crystal Copper		Polycrystalline Copper		Polycrystalline Nickel	
	$\Delta G_{crit}$ 10 <sup>20</sup> (J)	N <sub>crit</sub> (atoms)	$\Delta G_{crit}$ 10 <sup>20</sup> (J)	N <sub>crit</sub> (atoms)	$\Delta G_{crit}$ 10 <sup>20</sup> (J)	N <sub>crit</sub> (atoms)
65	-	-	-	-	1.27	1.32
70	1.34	1.20	0.98	0.87	1.08	1.04
75	1.17	0.97	0.85	0.71	0.94	0.834
80	1.03	0.80	0.75	0.58	0.82	0.678
85	0.91	0.67	0.66	0.49	0.72	0.560
90	0.81	0.56	0.59	0.41	0.64	0.467
100	0.66	0.41	0.48	0.30	0.51	0.334

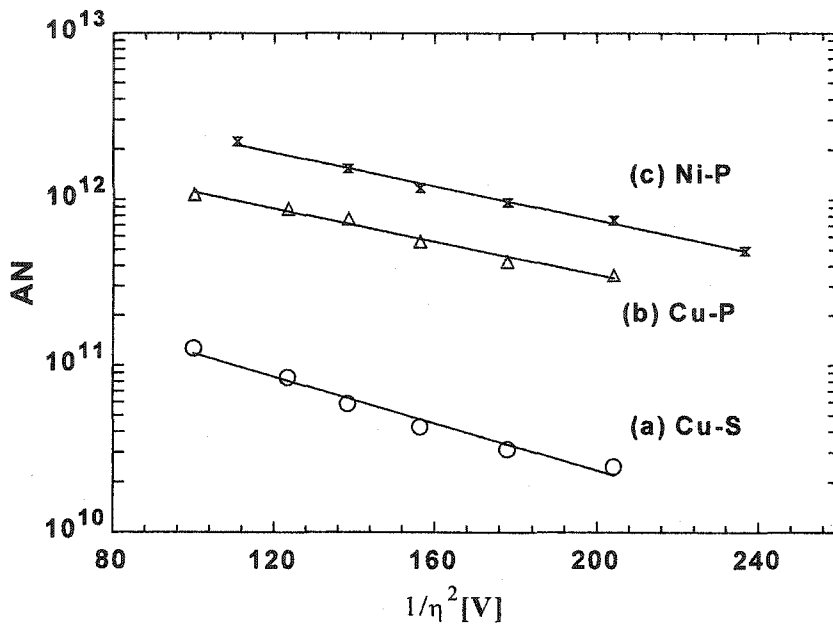


Figure 4.31 Nucleation rate as a function of  $1/\eta^2$  for tin electrodeposition on (a) single crystal copper (Cu-S), (b) polycrystalline copper (Cu-P), (c) polycrystalline nickel, in 0.02M  $\text{SnSO}_4$  /1.0M  $\text{H}_2\text{SO}_4$ /0.02M Tu /2mM  $\text{AgNO}_3$  solution.

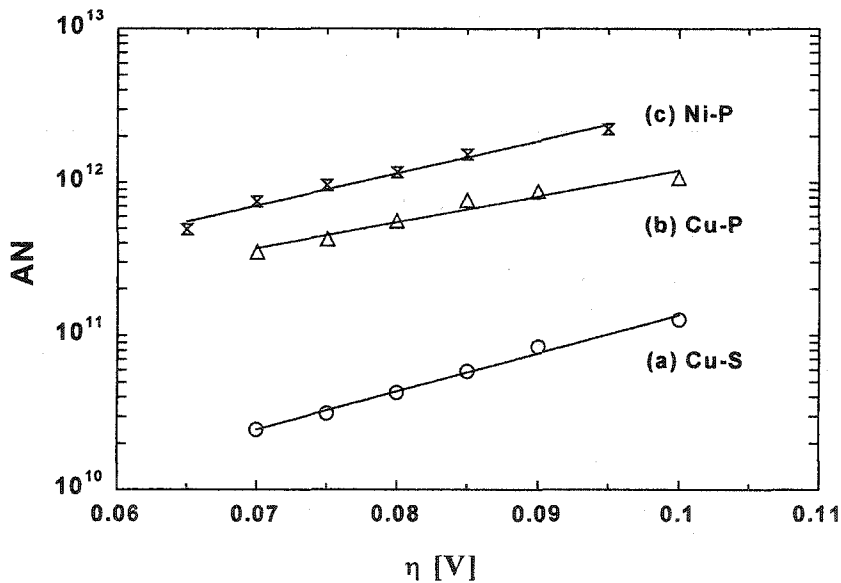


Figure 4.32 Dependence of nucleation rate with overpotentials for tin electrodeposition on (a) single crystal copper (Cu-S), (b) polycrystalline copper (Cu-P), (c) polycrystalline nickel, in 0.02M  $\text{SnSO}_4$  /1.0M  $\text{H}_2\text{SO}_4$ /0.02M Tu /2mM  $\text{AgNO}_3$  solution.

#### 4.1.3.4 Tin Electrodeposition from 0.02SnMS /1.0M MSA Solution

##### A). Nucleation rate constant and the number density of active sites

Current transients obtained at different deposition potentials for tin electrodeposition on single crystal copper are shown in Figure 4.33. The shape of these transients is typical of a diffusion-limited electrochemical reaction for nucleation and growth of a metal deposition on a foreign substrate. The time ( $t_{\max}$ ) to the current maximum depends on the overpotential and decreases as the applied potential is made more negative. In the experiments, the electrode potential was stepped from  $-450$  Mv, where no tin deposition takes place, to a final value in the range  $-570$  to  $-620$  Mv, where the nucleation and growth process occurs. The holding time at the initial potential ( $-450$  Mv) was 30s. The characteristic parameters obtained from these current transients are presented in Table 4-10.

The nucleation parameters  $A$  (nucleation rate constant) and  $N_0$  (number density of active sites) were calculated with the SM Model (see Table 4-11). As can be seen, this system has a high nucleation rate and number density of active sites, and nucleation is instantaneous. All nuclei are formed immediately after the potential step is applied, and the number of nuclei remains constant during the growth process. In comparison with tin sulfate solution without additives, it is readily seen that the two systems produced instantaneous nucleation on a single crystal copper substrate, but in methansulfonate solution, a greater overpotential is required to obtain a similar current-time profile. Probably the organic electrolyte anion inhibits the nucleation process, as discussed in section 4.2.4 below.

Table 4-10 Parameters extracted from the current transients for tin electrodeposition on single crystal copper substrates, from 0.02M SnMS /1.0M MSA solution.

Potential (mV)	Single Crystal Copper (Cu-S)	
	Max time (ms)	Max current (Ma/cm <sup>2</sup> )
-580	10.3	36.0
-590	8.6	39.8
-600	6.1	48.7
-610	5.2	53.0
-620	4.6	57.9

Table 4-11 Nucleation parameters resulting from Scharifker and Mostany's model for tin electrodeposition on single crystal copper substrates, from 0.02M SnMS /1.0M MSA solution.

Potential (mV)	Single Crystal Copper (Cu-S) ( $\alpha = 0.001$ )	
	$10^{-5}A(1/s)$	$10^{-8}No (1/cm^2)$
-580	1.22	0.78
-590	1.46	0.92
-600	2.06	1.22
-610	2.42	1.41
-620	2.73	1.52

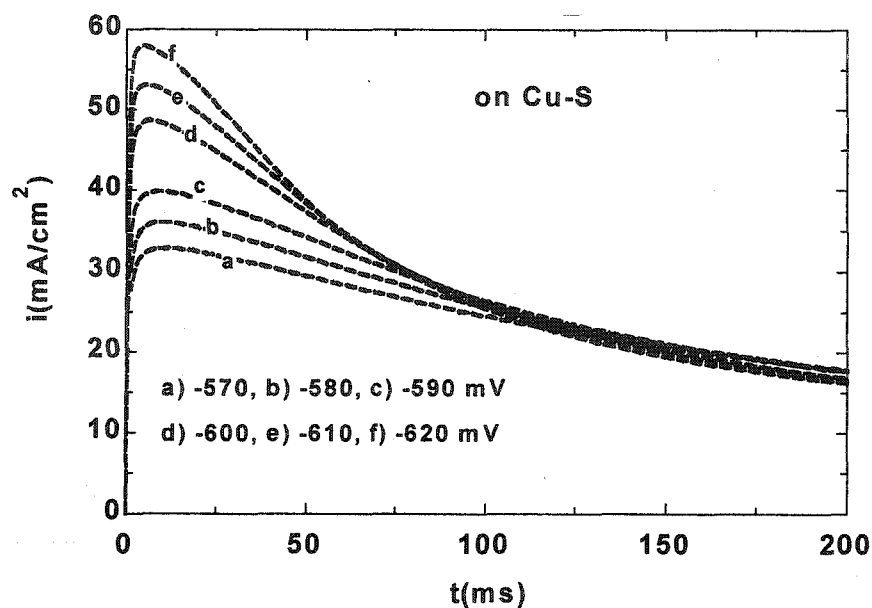


Figure 4.33 Current transients for tin electrodeposition on single crystal copper (Cu-S) in 0.02M SnMS /1.0M MSA solution at the indicated final potentials. The initial potential is  $-450$  Mv.

### B). Critical nucleus size

According to the classical theory,  $\ln(ANo)$  should have a linear relationship with  $1/\eta^2$ . As shown in Figure 4.34, the apparently straight line observed indicates a three-dimensional metal phase formation via nucleation and nucleus growth. Based on analysis of the data according to the classical approach, the critical nucleation energy ( $\Delta G_{crit}$ ) and the critical nucleus number ( $N_{crit}$ ) are obtained and listed in Table 4-12. It is clear that the critical nucleus size consists of 0-1 atoms.

Figure 4.35 illustrates the linear dependence of  $\ln(ANo)$  on  $\eta$ . According to the small cluster model of the atomistic approach, assuming  $\alpha = 0.5$ , it turned out the number of atoms in the critical nucleus is 0-1 over the entire range of investigated overpotentials.

The critical nucleus size obtained from the classical theory is in good agreement with atomistic theory.

Table 4-12 Critical Gibbs free energy of 3D nucleation and critical nucleus size for electrodeposition of tin on single crystal copper substrates

Overpotential (mV)	Single Crystal Copper (Cu-S)	
	$10^{20} \Delta G_{\text{crit}}$ (J)	$N_{\text{crit}}$ (atoms)
105	1.33	0.79
115	1.11	0.60
125	0.94	0.47
135	0.81	0.37
145	0.99	0.30

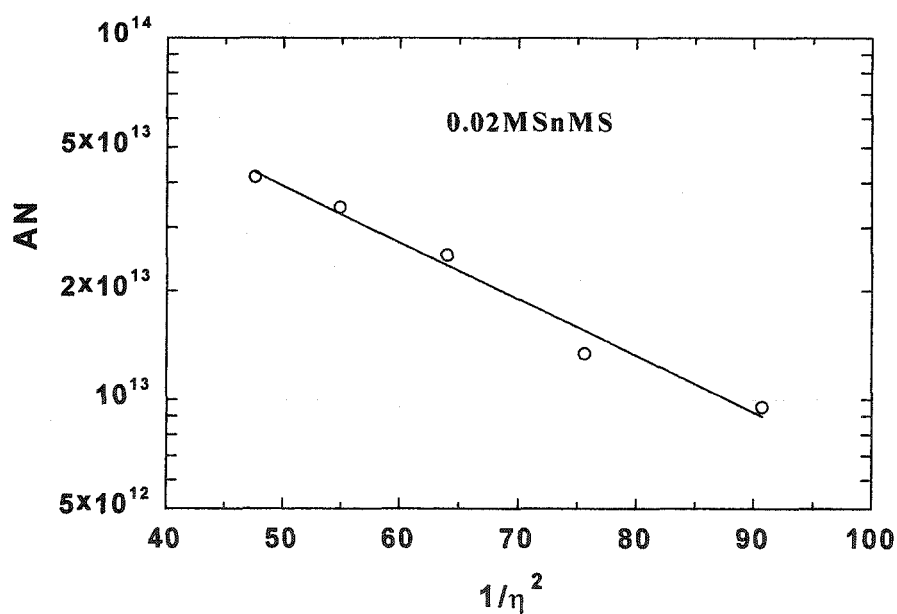


Figure 4.34 Nucleation rate as a function of  $1/\eta^2$  for tin electrodeposition on single crystal copper (Cu-S), in 0.02M SnMS /1.0M MSA solution.

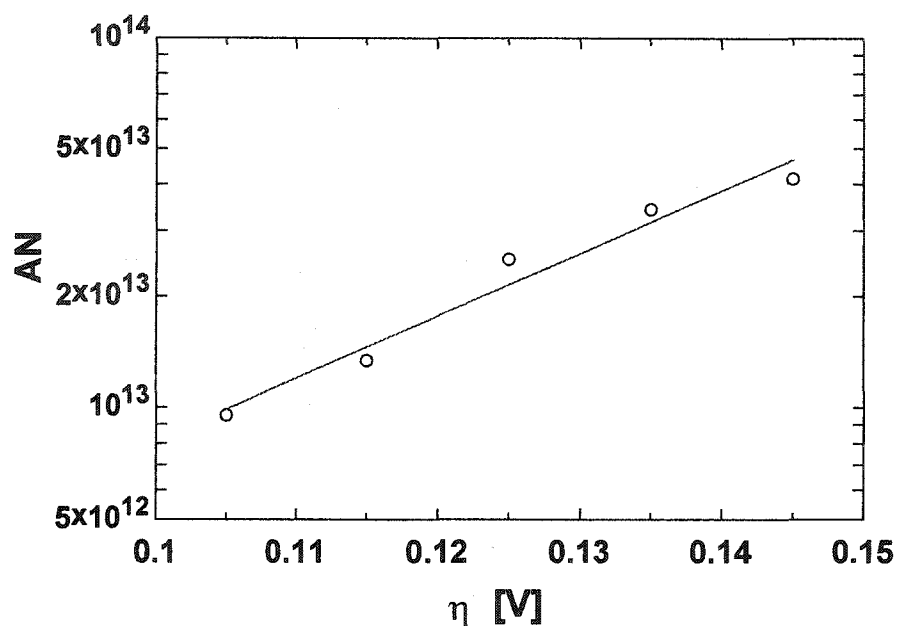


Figure 4.35 Dependence of nucleation rate with overpotentials for tin electrodeposition on single crystal copper (Cu-S), in 0.02M SnMS /1.0M MSA solution.

## 4.2 Discussion

### 4.2.1 Effects of Thiourea on Tin Nucleation and Growth Kinetics

Organic additives have substantial effects on the nucleation and growth kinetics of tin electrodeposition. In tin electrodeposition, the charge transfer step is fast and the rate of growth is controlled by mass transfer of tin ions to the growing centers. From cyclic voltammetric studies (Figure 4.1, 4.8, 4.9), in the presence of thiourea, the onset of tin electrodeposition is shifted negative, followed by rapid increase in current to a peak current density. The reductive current peaks appear to be higher than the peaks obtained from the acid tin solution without additives, indicating that thiourea adsorbs on the substrate surface, blocking the onset of tin deposition. At more negative potentials,



thiourea is desorbed from the surface and rapid deposition occurs, resulting in an increase in the peak current density.

From the chronoamperometric studies, addition of thiourea to the acid tin solution changes the nucleation process from instantaneous to progressive. This change can be explained by an increased number of nucleation sites at the substrate surface. This was verified by AFM and SEM measurements. Figure 4.36 shows that in the absence of thiourea, the current transients are much sharper and narrower. The characteristic maximum current density ( $i_{\max}$ ) is higher and corresponding time ( $t_{\max}$ ) is smaller in comparison with addition of thiourea, suggesting that nucleation of tin is retarded by thiourea. According to nucleation models <sup>[85, 86]</sup> for three-dimensional nucleation with diffusion-controlled growth, tin electrodeposition from additive-free solution produced instantaneous nucleation. Thus the surface is left with a relatively small number of nuclei producing a grainy deposit. With addition of thiourea, the quality of deposits was improved. More and relatively small nuclei of tin were obtained. Although the current transients cannot be fitted with nucleation models for tin deposition from the tin solution with thiourea, AFM and SEM analysis reveals that nucleation and growth of tin become progressive, in agreement with the fact that the organic additive initially inhibits nucleation.

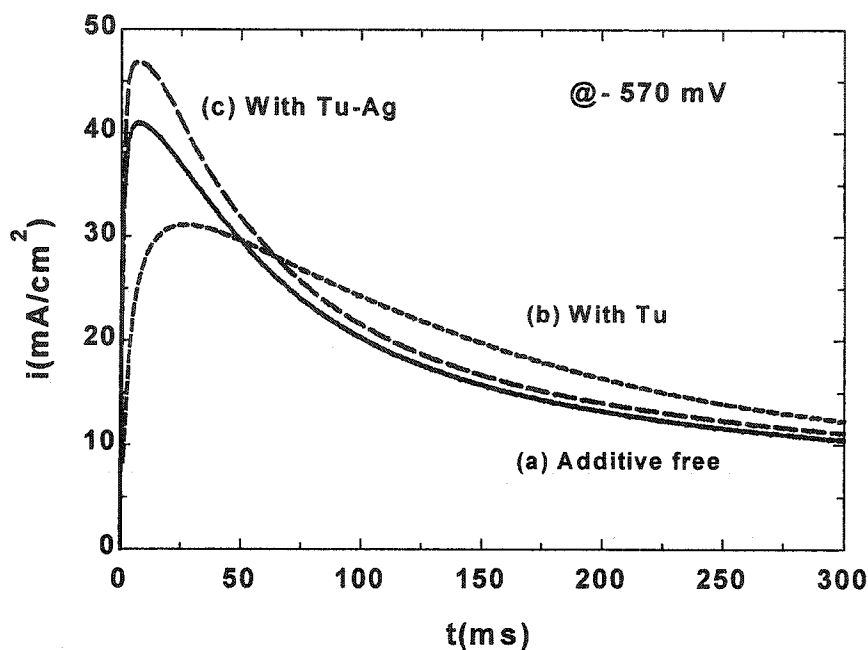


Figure 4.36 Current transients for tin electrodeposition on single crystal copper in acidic tin solutions containing: (a) Additive free, (b) thiourea, (c) thiourea-silver.

The adsorption of thiourea on copper electrode surfaces has been studied by surface enhanced Raman spectroscopy (SERS) <sup>[117-119]</sup>, radiometry <sup>[120]</sup>, and infrared spectroscopy (IR) <sup>[121]</sup>. The results showed that thiourea is adsorbed on the copper electrode surface via the sulfur atom, and the adsorption process is reversible at constant potential. Thiourea does not participate in the copper plating reaction, and there is no evidence of incorporation of thiourea into copper electrodeposits <sup>[122]</sup>.

Adsorbed thiourea may affect nucleation and growth kinetics by changing the concentration of adions on the electrode surface and the activation energy of surface diffusion of adions. In the presence of adsorbed thiourea the mean free path for lateral diffusion of adions is diminished, which is equivalent to a decrease in surface diffusion coefficient of adions. This decrease in surface diffusion may result in an increase in adion

concentration at steady state and thus an increase in the number of nucleation sites. But the effective coverage is relatively low. Thus in this case, fine-grained uniform tin deposits cannot be formed.

#### 4.2.2 Effects of Thiourea-Silver Complex on Tin Nucleation and Growth Kinetics

The standard potentials of the metals tin, copper, silver, zinc, lead and bismuth (Figure 4.37) cover a wide range. The reduction potential of silver ions is much more positive than that of tin ions. To reach a stable alloy composition, it is necessary to add suitable complexing agents for minimizing the difference in the standard potentials.

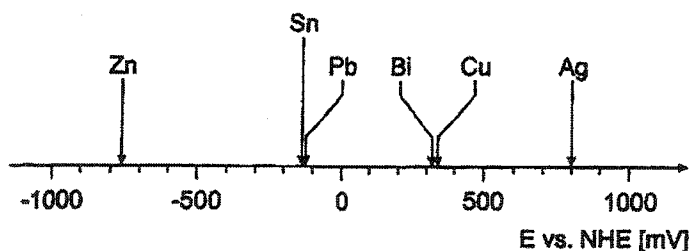
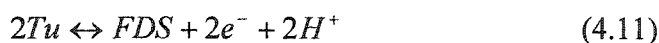
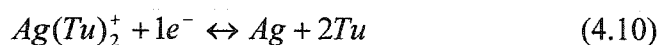
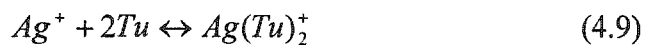
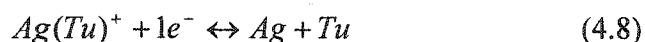


Figure 4.37 Relative position of the standard potentials of the metals, which are possible partners for leadfree tin alloys.

It is known that thiourea is a complexing agent for silver ions, which changes the reduction reaction from simple silver ions to a silver complex with an equilibrium potential close to that of tin. As thiourea complexes with  $Ag^+$  ions, the following chemical equilibria in solution and redox reactions should be taken into account <sup>[123]</sup>:





where Tu is thiourea, FDS is formandine disulfide.

When the ratio of  $C_{Tu}/C_{Ag^+}$  is equal to or larger than 5.0, the amount of free  $Ag^+$  ions is negligible <sup>[123]</sup>, and all of the silver complexes  $[Ag(Tu)_xNO_3]$  ( $x=1$  to 4) exist and the maximum ligand number ( $x$ ) of thiourea which can coordinate with each silver ion is four <sup>[124]</sup>. As the concentration of thiourea increases, the concentration of silver complexes with higher ligand number also increases.

In the presence of thiourea-silver complex, the process of nucleation and growth for tin electrodeposition cannot be classified into either instantaneous or progressive mechanism, because an intermediate behavior was observed at all studied potentials. The current transients (Figure 4.36) clearly show that for tin electrodeposition from the solution containing thiourea-silver complexes, at the same deposition potential, the value of  $i_{max}$  is larger and  $t_{max}$  is smaller than that in the case of tin acid solution with thiourea, but similar to that obtained in tin acid solution without additives.

Since the number density of nuclei is a measure of the smoothness of the surface it is of great interest to calculate its value in deposits obtained without and with thiourea-silver at various deposition potentials. Analysis of the experimental current transients by SM model, the nucleation parameters obtained are listed in Table 4-4 and 4-8. From the tables, it is seen that in the case of tin deposition from tin acid solution with thiourea-silver, the number density of active sites ( $N_0$ ) is significantly higher, and the critical

Gibbs free energy ( $\Delta G_{\text{crit}}$ ) is slightly larger than that obtained from the solution without additives.

Tin ions in acid aqueous solution are complexed by water molecules or other ligands. In the electrodeposition process, all of these ligands must be removed as the ion enters the electric double layer, then discharged and adsorbed onto the electrode surface as an adatom. The adatom diffuses across the electrode surface to a nucleation site, and becomes incorporated into the growing crystal lattice of the deposit.

The effects of thiourea-silver complexes on tin nucleation and growth kinetics can be explained by an induced adsorption and ion-bridging mechanism [42, 125]. It is well known that thiourea is strongly adsorbed on copper [117-122] and silver electrodes [118, 126-129]. Therefore, the thiourea-silver complexes are more readily adsorbed on copper and silver substrates than uncomplexed tin ions. It is postulated that the adsorbed thiourea-silver complex ions are discharged and deposited, forming nucleation sites for tin deposition. As the reduction of silver and tin ions proceeds, the thiourea has been postulated to adsorb on the high spots (newly formed nucleation sites), blocking further deposition on these points. The newly formed nuclei are unable to grow, forcing the formation of new nuclei, leading to more even deposits.

In the ion-bridging mechanism, it is assumed that the thiourea-silver complex acts as an electron bridge and accelerates the rate of electron flow from the electrode to the metal ions. The ion-bridging catalysis increases the rate of deposition of the metal, causing a shift of the reduction potential to less negative values and an increase in current efficiency.

### 4.2.3 Effects of Substrate on Nucleation and Growth Kinetics of Tin and Tin-Silver Alloy

Nucleation and growth kinetics of metal electrodeposition are also strongly affected by the surface properties of substrates. The electrochemical activity of substrates depends on their surface structure. Figure 4.38 shows that at the same electrodeposition potential, the value of  $i_{\max}$  is largest for tin electrodeposition on polycrystalline copper, and smallest for tin electrodeposition on single crystal copper. Based on the SM model, there are greater differences in number density of active sites among these substrates. In the case of tin electrodeposition on single crystal copper, the number density of nuclei is significantly smaller compared to deposition on polycrystalline substrates. For deposition on polycrystalline substrates, the number density of nuclei on copper is higher than on nickel (see Table 4-8). According to atomistic theory, critical Gibbs free energy of 3D nucleation and critical nucleus size follow the sequence: Cu-S > Ni-P > Cu-P, which is consistent with the number density of active sites on the substrate surface.

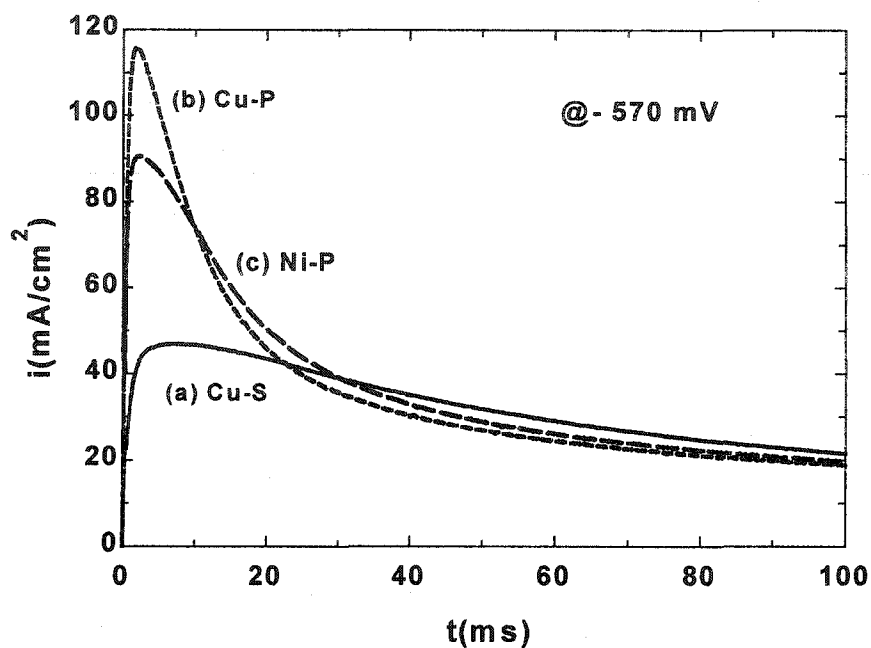


Figure 4.38 Current transients for tin electrodeposition on various substrates in  $0.02\text{M SnSO}_4 / 1\text{M H}_2\text{SO}_4 / 0.02\text{M Tu} / 2\text{mM AgNO}_3$ , (a) single crystal Cu, (b) polycrystalline Cu, (c) polycrystalline Ni.

#### 4.2.4 Effects of Electrolyte Anion on Nucleation and Growth Kinetics of Tin Electrodeposition

Tin electrodeposition on single crystal copper in various acidic electrolyte solutions was studied. Figure 4.39 clearly shows that tin electrodeposition from MSA solution requires a greater overpotential to obtain a current–time profile similar to that in sulfuric acid solution. The shape of transients obtained from MSA solution is wider and decay is slower. The nucleation is more difficult in MSA solution because a higher overpotential is needed to obtain three-dimensional diffusion-controlled nucleation and growth of tin.

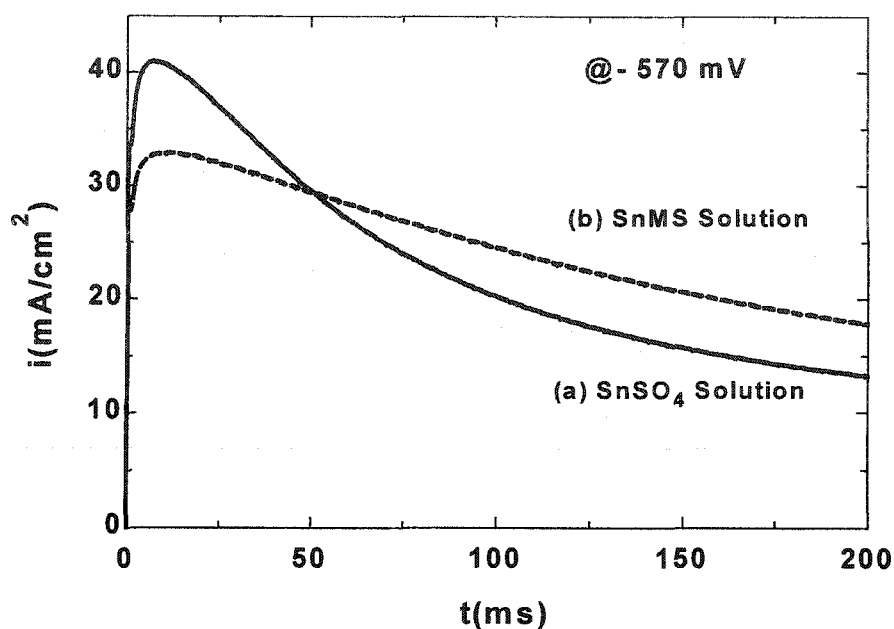


Figure 4.39 Current transients for tin electrodeposition on single crystal copper in solutions: (a) 0.02M SnSO<sub>4</sub> /1M H<sub>2</sub>SO<sub>4</sub>, (b) 0.02M SnMS /1M MSA, at -570 mV.

The results suggest that organic anions hinders tin nucleation. Probably the methanesulfonate anions more easily adsorb on the substrate surface than sulfate anions. The activation energy for charge transfer in an organic acid is usually higher <sup>[3]</sup>. The adsorption of anions (such as sulfate, pyrophosphate, cyanide anions) at the electrode surface has been verified <sup>[130-132]</sup>. It was also noticed that sulfate anions display a potential-dependent adsorption behavior at the electrode surface: adsorption was enhanced at more negative potentials <sup>[130]</sup>. In Hardesty's <sup>[133]</sup> study, the shape of anions has significant effect on metal deposition. The replacement of an oxygen atom in sulfate ion by the amido group (NH<sub>2</sub><sup>-</sup>) enhanced adsorption. Thus there is reason to believe that replacement of an oxygen atom in sulfate ion by the methyl group (CH<sub>3</sub><sup>-</sup>) makes the anion less regular and more polarizable. This organic anion easily adsorbs on the



electrode surface, which increases the effective surface coverage, and favors the formation of a uniform deposits.

## CHAPTER 5

# MORPHOLOGY OF TIN AND TIN-SILVER ALLOY IN THE INITIAL STAGES OF ELECTRODEPOSITION

The morphology of tin electrodeposition on single crystal copper in the early stages was analyzed by Scanning Electron Microscopy (SEM) and Atomic Force Microscopy (AFM) to provide information about the shape and topography of the crystallites. SEM and AFM were used to observe the structure and distribution of nuclei, and to determine the number density of nuclei. The stability of the deposited metal allows the use of ex situ measurements without loss in quality.

In the experiments, the samples for morphology studies were prepared by the electrodeposition of tin on a single crystal copper substrate from several electrolyte solutions under potentiostatic conditions. The deposition time in the potential step was chosen to obtain visible and stable nuclei and minimize coalescence of nuclei. After finishing electrodeposition, the sample was quickly removed from the electroplating bath, rinsed in a stream of pure water, and dried in air.

## 5.1 Effect of Deposition Potential on Tin Deposit Morphology

It is well known that deposition potential strongly affects nucleation and growth kinetics of metal deposition. This is partially due to the fact that tin electrodeposition from dilute electrolyte is a diffusion-limited process. Based on the nucleation theory, the nucleation rate has an exponential dependence on overpotential, and the number density of nuclei varies exponentially with deposition potential. Figure 5.1 to 5.2 show SEM micrographs of tin deposits obtained from acid sulfate solutions without additives under different deposition potentials. At low deposition potential ( $-520$  mV), only a few well defined crystallites were observed. The tin crystallites had a tetragonal shape. A large ratio of free area to covered area on the sample surface is provided by deposition of a small number of nucleation sites. The grains grew perpendicularly to the substrate surface and formed dendrites (see Figure 5.3). The formation of dendrites in the electrodeposition process shows fast electron-transfer and diffusion control of the growth process. At higher deposition potential ( $-560$  mV), the number of nuclei increased considerably, as shown in Figure 5.2. The crystallites displayed multiple shapes, and no well-defined crystals were obtained under these conditions.

To quantify the grain size and the number density of nuclei and correlate the morphological information with nucleation mechanism and growth kinetics of tin electrodeposition, AFM was used. Figure 5.4 to 5.6 demonstrate that the nucleus densities increases as deposition potentials are made more negative. From the AFM images, 3D structure of the nuclei was clearly observed. The nucleus size was almost the same, and no other small nuclei can be observed at high resolution, indicating instantaneous nucleation, in agreement with the chronoamperometric analysis.

The number density of nuclei in the AFM images was measured by means of Digital Instrumental Nanoscope Image Analysis software. At low potential ( -530 mV, Figure 5.4), the measured number of nuclei per unit area is  $5.72 \times 10^7 \text{ cm}^{-2}$ . The mean nucleus height was 146 nm, and the mean diameter 654 nm. At a deposition potential of -550 mV (Figure 5.5), the measured number of nuclei was  $1.01 \times 10^8 \text{ cm}^{-2}$ . The mean nucleus height was 70 nm, and mean diameter 466 nm. When deposits were obtained at more negative potential (-570 mV), the number density of nuclei increased significantly, as shown in Figure 5.6. The measured number of nuclei per unit area was  $2.55 \times 10^8 \text{ cm}^{-2}$ , mean height was 28 nm, and mean diameter is 353 nm.

It is notable that at high overpotential, the surface with the highest nucleus density has the smallest nucleus size. This is because high overpotential lowers the surface energy of the substrate, and makes more active sites available for nucleation. On the other hand, more tin ions are driven to the electrode surface to form nuclei. At low overpotential, the rate of growth of nuclei is more than the rate at which new nuclei are formed, resulting in large void areas and dendrites. But at very high overpotential, evolution of hydrogen occurs, and bubble formation leads to porous and spongy deposits.

The dependence of the number density of active sites on overpotential is also predicted by the SM model. The calculated and measured nucleus densities are given in Table 5-1.

Table 5-1 shows that both calculated and measured nucleus densities increase as deposition potential is made more negative. At low deposition potential, the difference in nucleus density between the calculated and measured value is small. But at more negative deposition potential, the measured value is significantly higher. At -570 mV, the

measured nucleus density is 2.5 times as great as the calculated value. The possible explanation for the difference could be the inability of the mathematical model to distinguish nucleation phenomena that could occur within the diffusion zone, e.g. more than one nucleus within a single diffusion zone [74].

Table 5-1 Calculated and measured nucleus density deposited from various tin electrolyte solutions.

Tin Solution	Additives	Potential	Nucleus Density (cm <sup>-2</sup> )	
			Calculated	Measured
Sulfate	No additives	-530	-	0.572 × 10 <sup>8</sup>
		-550	0.624 × 10 <sup>8</sup>	1.01 × 10 <sup>8</sup>
		-570	1.02 × 10 <sup>8</sup>	2.55 × 10 <sup>8</sup>
	Thiourea	-550	-	1.87 × 10 <sup>8</sup>
	Thiourea-silver	-550	0.905 × 10 <sup>8</sup>	6.16 × 10 <sup>8</sup>
Methanesulfonate	No additives	-550	-	0.873 × 10 <sup>8</sup>
		-580	0.78 × 10 <sup>8</sup>	-

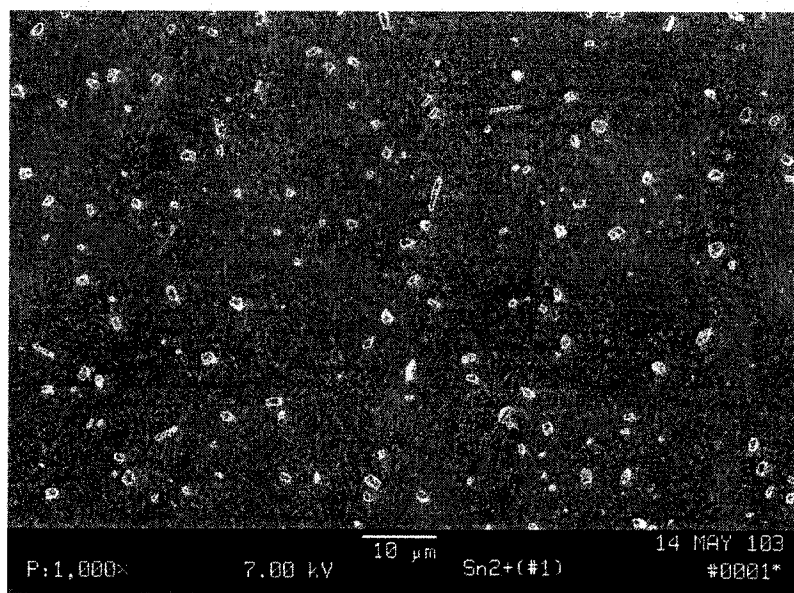


Figure 5.1 SEM micrograph of tin deposit obtained at  $-520$  mV for 4 sec in  $0.02\text{M SnSO}_4 / 1.0\text{M H}_2\text{SO}_4$  solution.

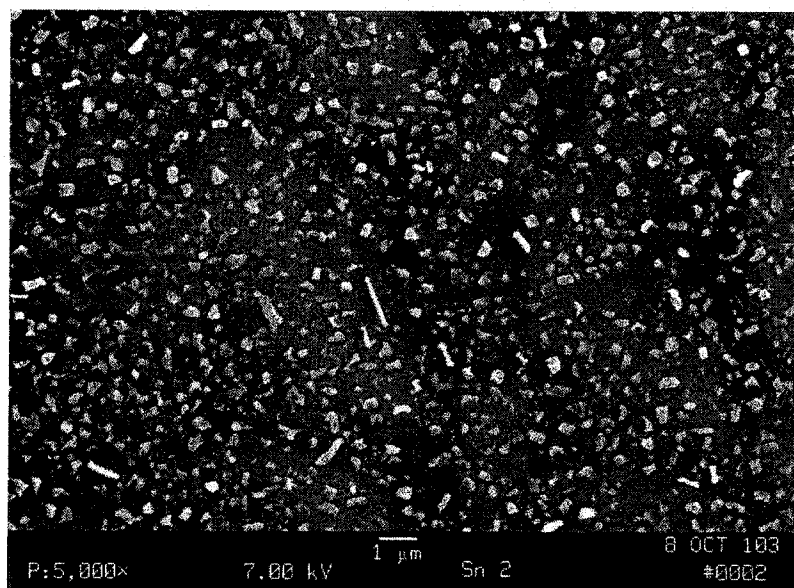


Figure 5.2 SEM micrograph of tin deposit obtained at  $-550$  mV for 4 sec in  $0.02\text{M SnSO}_4 / 1.0\text{M H}_2\text{SO}_4$  solution

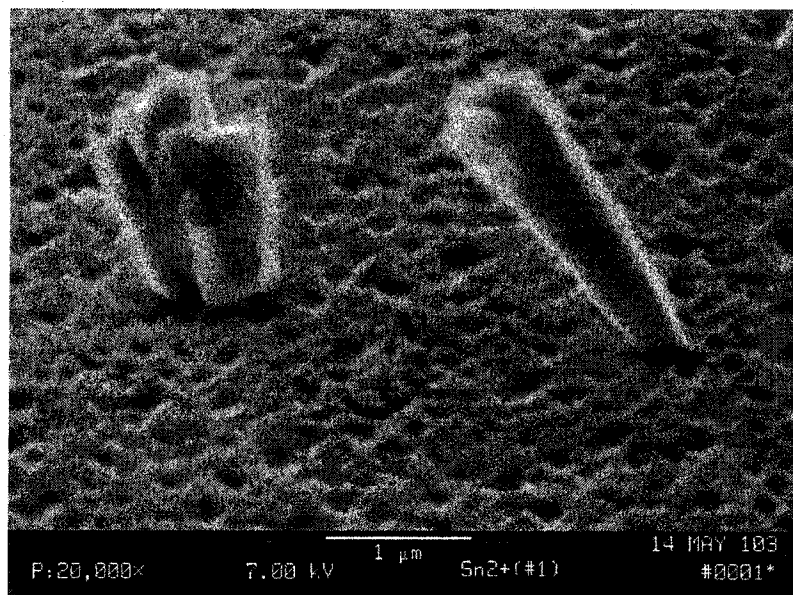


Figure 5.3 SEM micrograph of tin deposit obtained at  $-520$  mV for 4 sec in  $0.02\text{M}\text{SnSO}_4 / 1.0\text{M}\text{H}_2\text{SO}_4$  solution.

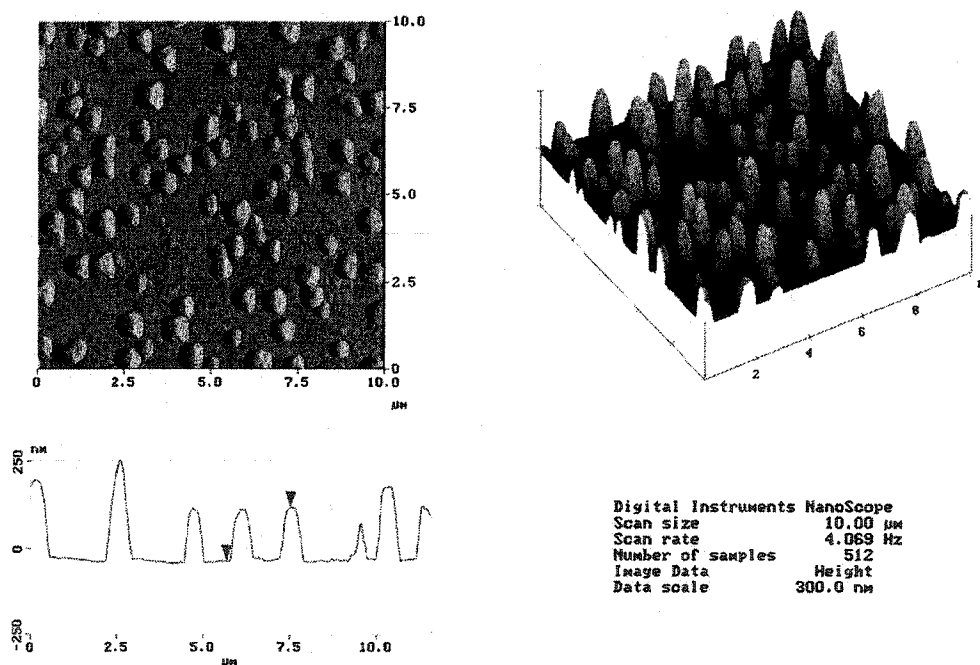


Figure 5.4 AFM images of tin deposits obtained at  $-530$  mV for 4 sec in  $0.02\text{M}\text{SnSO}_4 / 1.0\text{M}\text{H}_2\text{SO}_4$  solution.

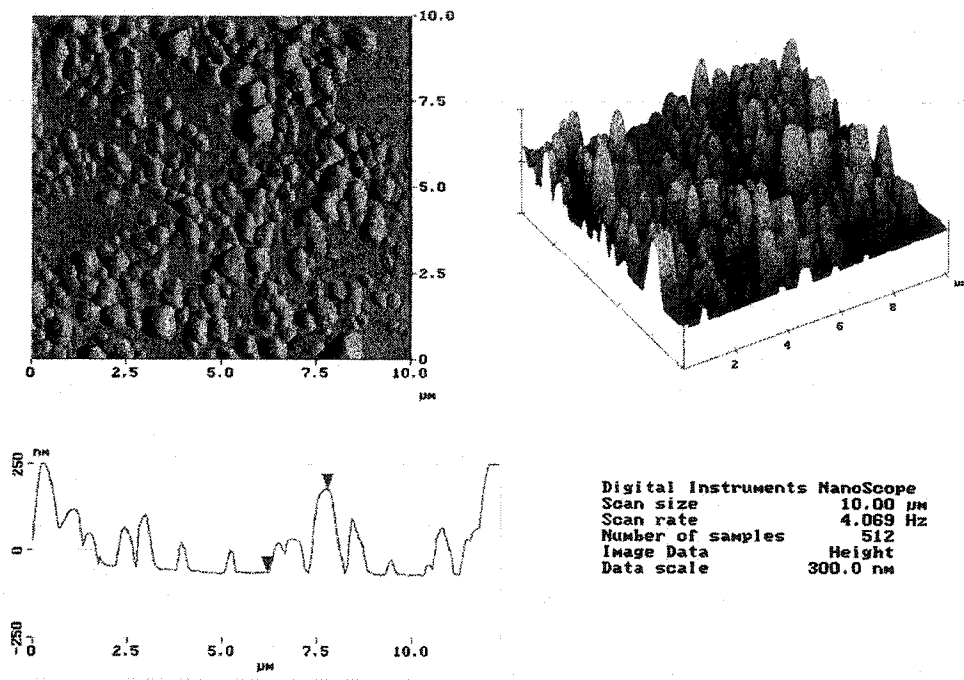


Figure 5.5 AFM images of tin deposits obtained at  $-550$  mV for 4 sec in  $0.02\text{M SnSO}_4 / 1.0\text{M H}_2\text{SO}_4$  solution.

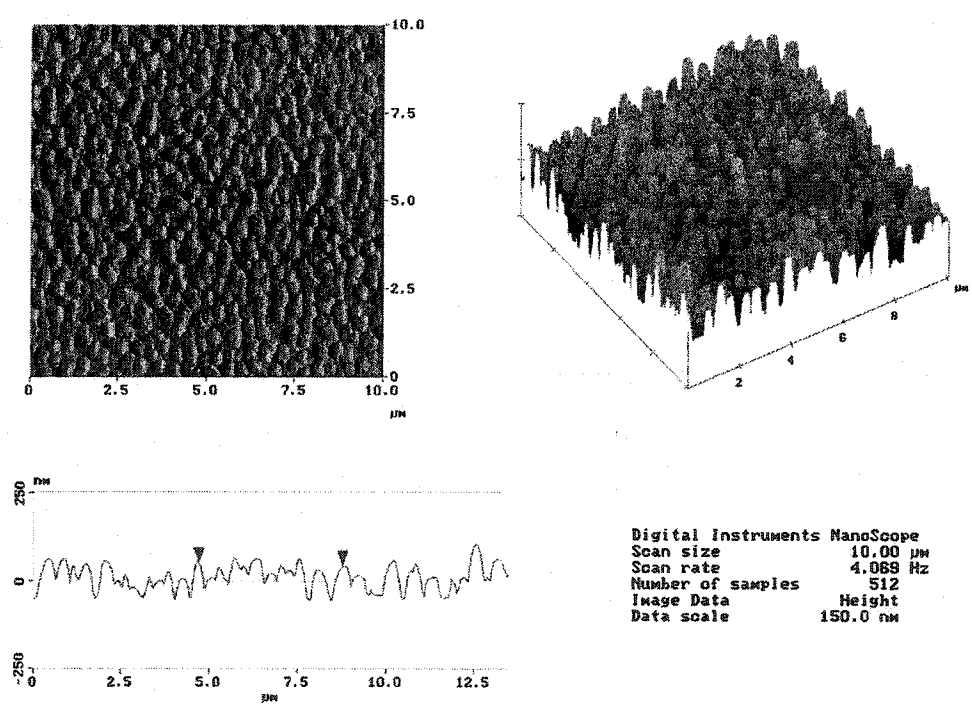


Figure 5.6 AFM images of tin deposits obtained at  $-570$  mV for 3 sec in  $0.02\text{M SnSO}_4 / 1.0\text{M H}_2\text{SO}_4$  solution.



## 5.2 Effect of Additives on Deposit Morphology

The effects of thiourea and thiourea-silver on the morphology of nuclei were also investigated by SEM and AFM. Figures 5.2, 5.7 and 5.8 show SEM micrographs of tin deposits obtained from acid sulfate solutions without and with additives under potentiostatic conditions. In the absence of additives, non-homogeneous and island-like crystallites are observed. The grain sizes are big, and a large free area remains on the surface. In the presence of thiourea (Figure 5.7), more nuclei are obtained. The grain sizes are small, and nuclei overlap. The increase in nuclei is expected because of the blocking effect of thiourea that causes a reduction in the nucleation rate constant. Free areas remain on the surface of the single crystal copper substrate, and compact electrodeposits of tin could not be obtained. With addition of thiourea-silver, a dense, smooth, and fine-grained tin deposit is obtained, as shown in Figure 5.8. The grain boundaries merge, the nuclei overlap, and the distinct geometries disappear.

To gain a better insight into the profile of tin deposit structures, AFM was used. Figure 5.4, 5.9 and 5.10 show AFM images of tin deposits obtained in acid tin sulfate solutions with and without additives. The AFM images confirm the topographic view obtained in the SEM and allow some quantifications. In the case of additive free solution, peaks with an average height of 146 nm, and 3D island growth are observed. The nucleus size observed in Figure 5.4 is almost uniform, which indicates instantaneous nucleation. The measured number of nuclei per unit area was  $5.72 \times 10^7 \text{ cm}^{-2}$ , the mean height was 146 nm and the mean diameter 654 nm. In the presence of thiourea, Figure 5.9 shows that most of the tin deposits present a globular morphology which can be attributed to a growing spherical nucleus under diffusion control. As also can be seen, a wide

distribution of nucleus sizes confirms that the initial deposition of tin can be described by a progressive nucleation mechanism, which is consistent with the chronoamperometric analysis. The measured number of nuclei was  $1.87 \times 10^8 \text{ cm}^{-2}$ , the mean height was 35 nm and the mean diameter 345 nm. These results confirm that the surface coverage is improved by addition of thiourea to the solution. In the presence of thiourea-silver, Figure 5.10 clearly shows that the nucleus size is much smaller, and the number density of nuclei is significantly higher. The measured number density of nuclei was  $6.16 \times 10^8 \text{ cm}^{-2}$ , which is about one order of magnitude higher than that obtained from additive free acid sulfate solution. The mean nucleus height was 17 nm, and the mean nucleus diameter was 198 nm. The nuclei start to coalesce to produce uniform and smooth deposit, and also display a small range of nucleus sizes. This indicates that tin nucleation has intermediate behavior under this condition.

The evolution of tin electrodeposits in acid sulfate solution containing thiourea-silver was investigated at fixed potential (-550 mV) and different deposition times. Figure 5.10, taken at 6s and 28 mC/cm<sup>2</sup> of total charge, shows a random distribution of nuclei with a density of  $6.16 \times 10^8$ . Figure 5.11 shows coalescence of the nuclei for 30s deposition time and 73 mC/cm<sup>2</sup> total charge. The nuclei grow to larger sizes and overlap. For a longer deposition time, 300s and a total charge of 410 mC/cm<sup>2</sup>, Figure 5.12 shows that a compact, uniform and smooth surface are obtained. It also reveals that many new nuclei of small sizes are formed on the deposit surface. The results show that a large density of nuclei is needed and that the rate of growth should be kinetically limited in order for the nuclei to coalesce to form a smooth surface.

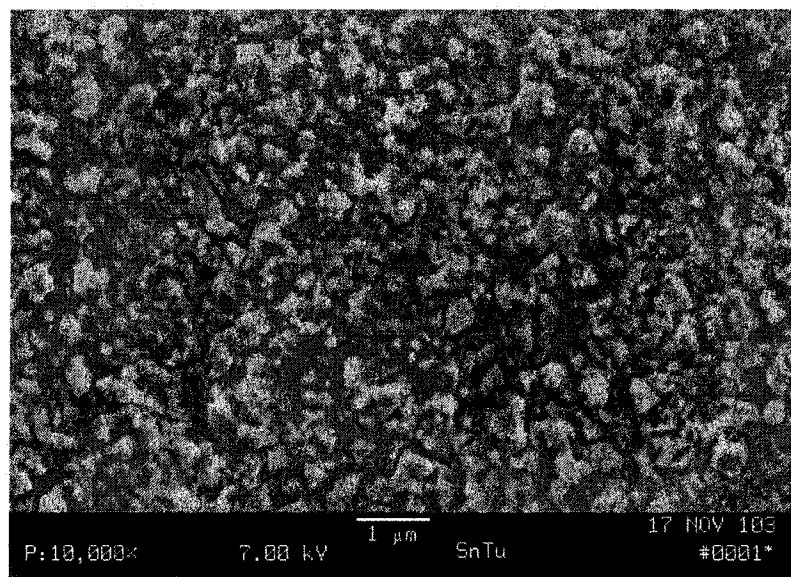


Figure 5.7 SEM micrograph of tin deposit obtained at  $-550$  mV for 8 sec in  $0.02\text{M SnSO}_4$  /  $1.0\text{M H}_2\text{SO}_4$  /  $0.02\text{M Thiourea}$  solution.

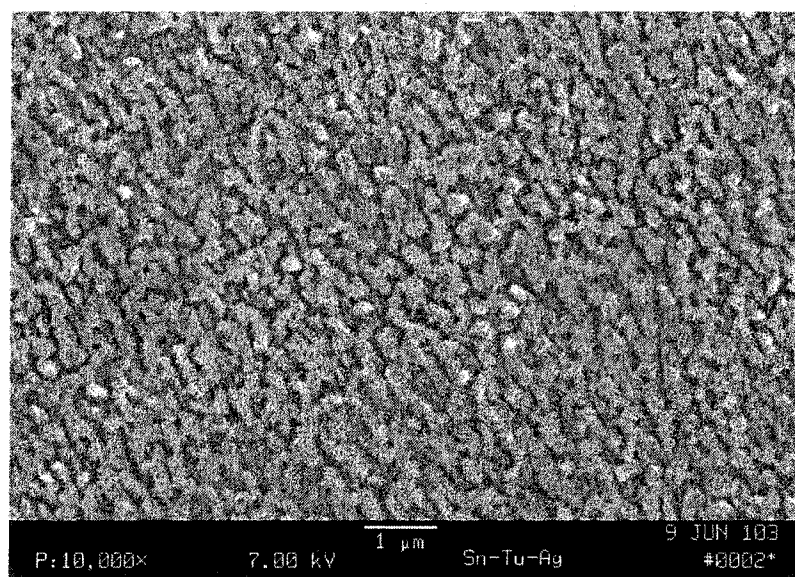


Figure 5.8 SEM micrograph of tin deposit obtained at  $-550$  mV for 6 sec in  $0.02\text{M SnSO}_4$  /  $1.0\text{M H}_2\text{SO}_4$  /  $0.02\text{M Thiourea}$  /  $2\text{mM AgNO}_3$  solution.

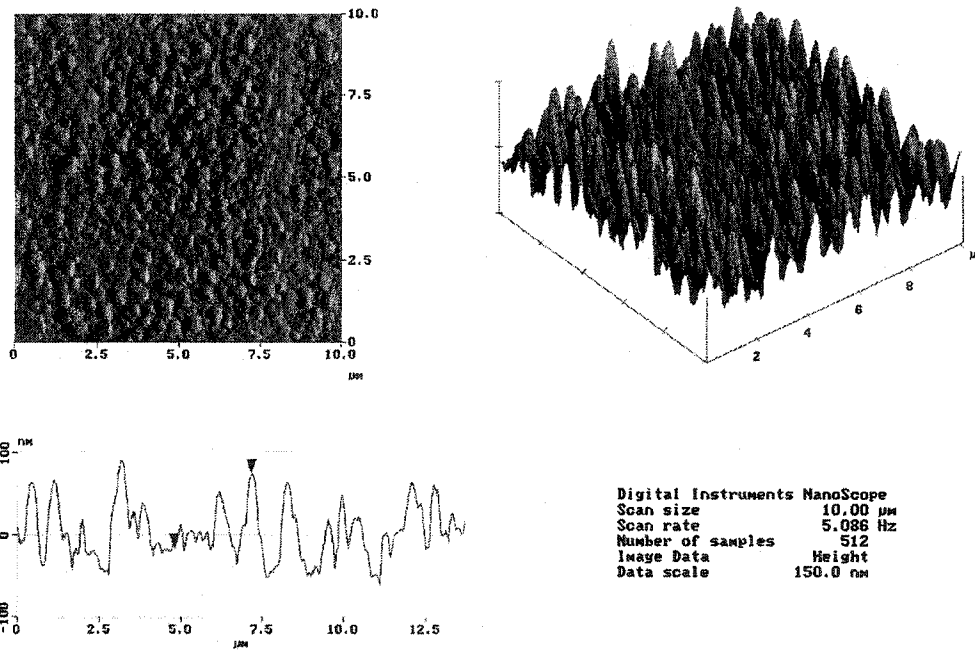


Figure 5.9 AFM images of tin deposit obtained at  $-550$  mV for 8 sec in  $0.02\text{M SnSO}_4 / 1.0\text{M H}_2\text{SO}_4 / 0.02\text{M Thiourea}$  solution.

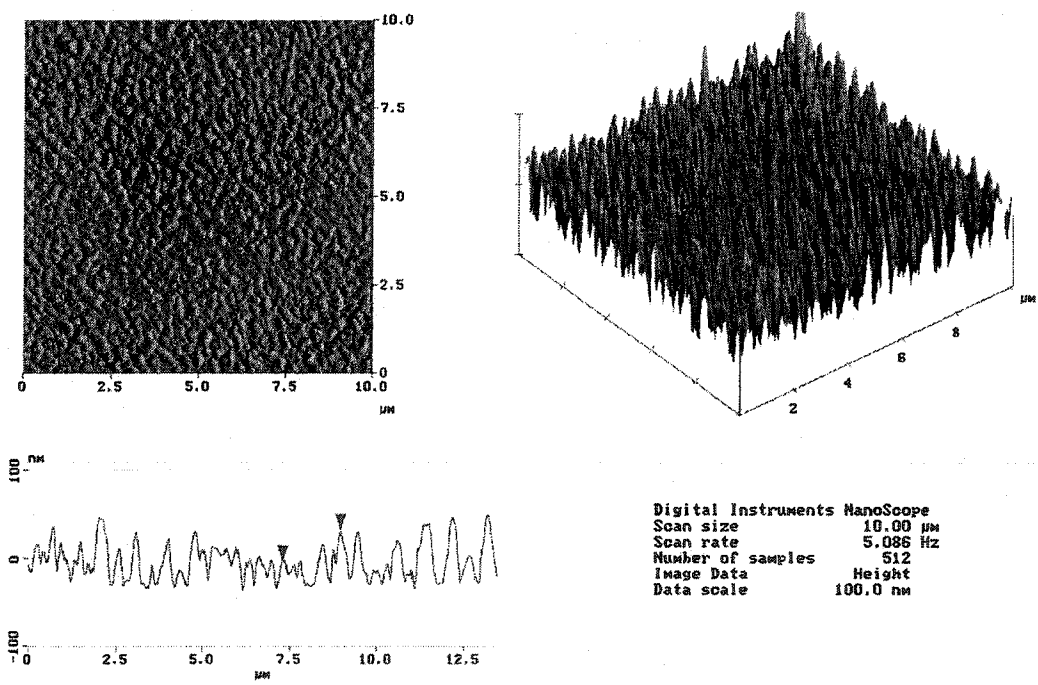


Figure 5.10 AFM images of tin deposit obtained at  $-550$  mV for 6 sec in  $0.02\text{M SnSO}_4 / 1.0\text{M H}_2\text{SO}_4 / 0.02\text{M Thiourea} / 2\text{mM AgNO}_3$  solution.

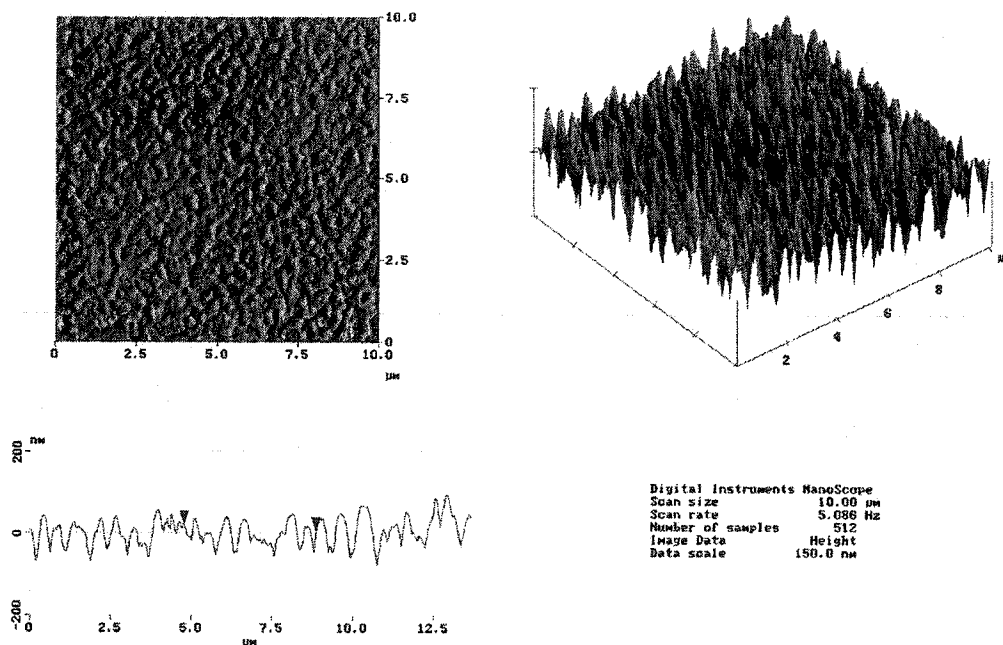


Figure 5.11 AFM images of tin deposit obtained at  $-550$  mV for 30 sec in  $0.02\text{M SnSO}_4 / 1.0\text{M H}_2\text{SO}_4 / 0.02\text{M Thiourea} / 2\text{mM AgNO}_3$  solution.

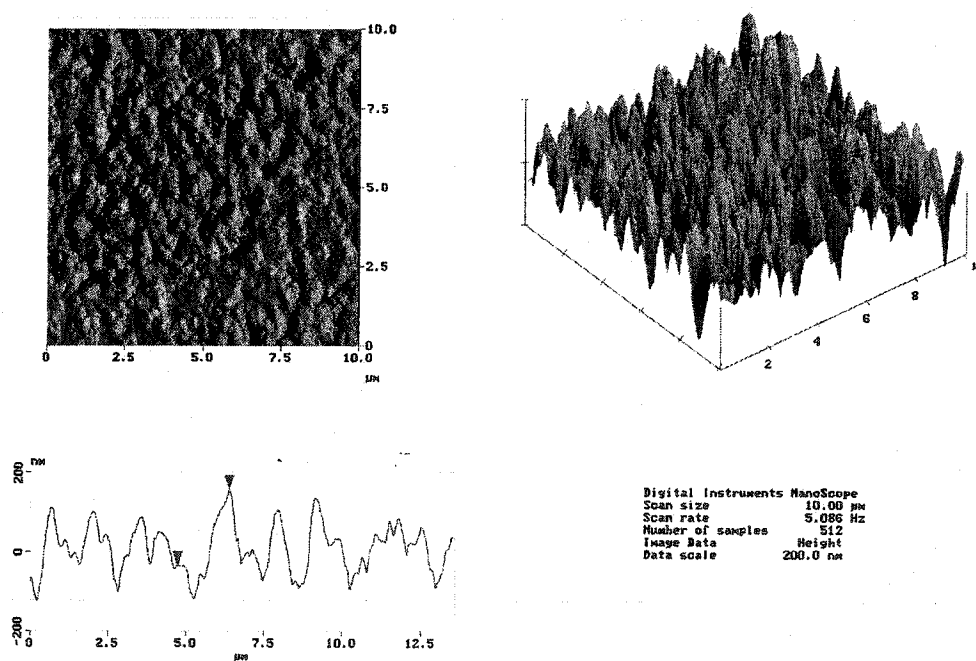


Figure 5.12 AFM images of tin deposit obtained at  $-550$  mV for 300 sec in  $0.02\text{M SnSO}_4 / 1.0\text{M H}_2\text{SO}_4 / 0.02\text{M Thiourea} / 2\text{mM AgNO}_3$  solution.

### 5.3 Effect of Electrolyte Anion on Tin Deposit Morphology

The surface morphology of tin deposits obtained from sulfate and methanesulfonate electrolytes was analyzed by SEM to determine influence of the anion on the morphology in the initial deposition stages. Figure 5.7 to 5.8 and 5.13 to 5.14 demonstrate that the morphology and grain size are both dependent on electrolyte anions. In the presence of thiourea, both tin deposits from acid sulfate and methanesulfonate solutions have a wide range of grain size. The surface structure of tin deposit obtained from sulfate solution is rough and grain size is large in comparison with one obtained from the methansulfonate solution (Figure 5.7 and 5.13). In the presence of thiourea-silver (Figure 5.8 and 5.14), the surface morphology was very smooth and had a fine structure. Comparison of these morphologies shows that relatively smaller crystals and more dense and compact electrodeposits are obtained from acid methanesulfonate solutions.

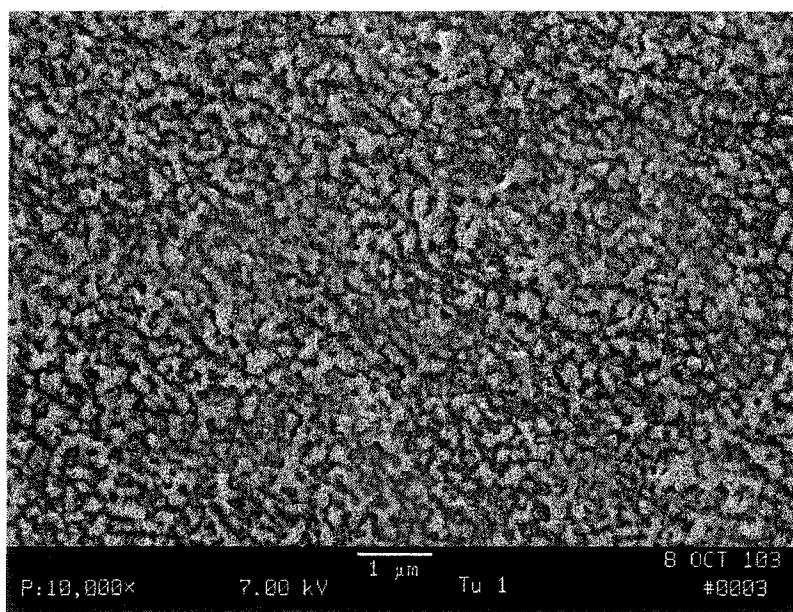


Figure 5.13 SEM micrograph of tin deposit obtained at  $-530$  mV for 8 sec in  $0.02\text{M SnMS} / 1.0\text{M MSA} / 0.02\text{M Thiourea}$  solution.

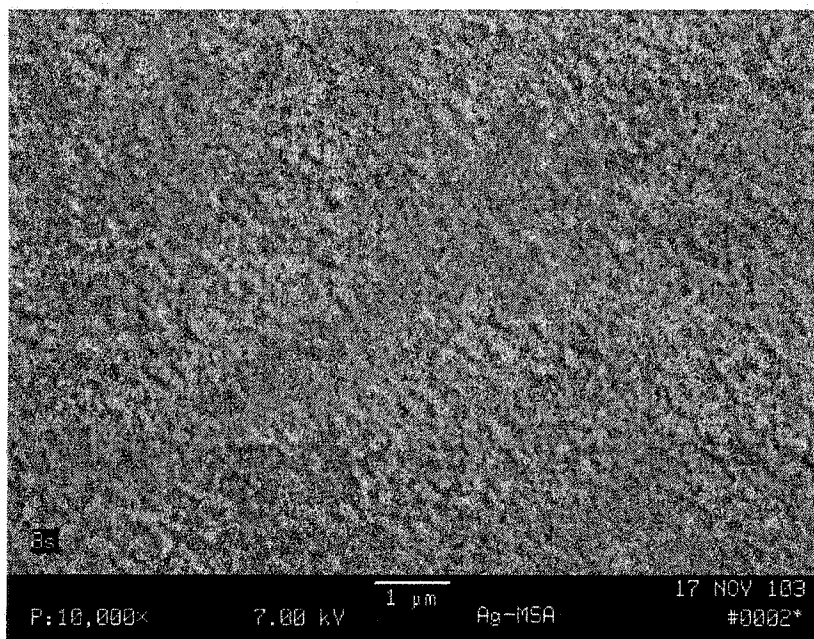


Figure 5.14 SEM micrograph of tin deposit obtained at  $-530$  mV for 8 sec in  $0.02\text{M SnMS} / 1.0\text{M MSA} / 0.02\text{M Thiourea} / 2\text{mM AgNO}_3$  solution.

## CHAPTER 6

### CONCLUSIONS

Nucleation and growth kinetics of tin and tin silver alloy in the initial stage of electrodeposition were investigated by electrochemical methods and SEM, AFM techniques. The nucleation mechanism, number density of active sites, and nucleation rate constant were determined based on multiple nucleation with three-dimensional mass transfer control. The critical nucleus size and Gibbs free energy of critical nucleus formation were evaluated by means of classical and atomistic nucleation approaches. In addition to observe the shape and topography of nuclei, SEM and AFM were used to correlate the morphological information with nucleation mechanism and growth kinetics, quantify the grain size and number density of nuclei.

Based on chronoamperometric studies and SM nucleation model analysis, in acid tin sulfate solution without additives, tin electrodeposition is instantaneous nucleation with three-dimensional diffusion controlled growth. Addition of thiourea to the acid tin solution changes the nucleation process from instantaneous to progressive, which was confirmed by SEM and AFM analysis. In the acid tin solution containing thiourea-silver complexes, the process of nucleation is unclassified because an intermediate behavior was observed.



From cyclic voltammetric studies, addition of thiourea to the acid tin solution, the onset of tin electrodeposition is shifted negative, followed by rapid increase in current to a peak current density. The reductive current peaks appear to be higher than the peaks obtained from the acid pure tin solution. In the chronoamperometric studies, The characteristic maximum current density ( $i_{\max}$ ) is smaller and corresponding time ( $t_{\max}$ ) is longer in comparison with acid pure tin solution, suggesting that nucleation of tin is retarded by thiourea. In the presence of thiourea-silver complex, the value of  $i_{\max}$  is larger and  $t_{\max}$  is smaller than that in the case of tin acid solution with thiourea, but similar to that obtained in acid tin solution without additives.

The number density of active sites is a measure of the smoothness of the surface. To produce compact, smooth deposit, high number density of nuclei, and limited nucleation rate constant are expected. Analysis of the experiment current transients by SM model, it was found that the number density of active sites ( $N_0$ ) is significantly higher in tin solution with thiourea-silver than that obtained in the solution without additives, indicating that silver favor tin nucleation, but decrease its growth rate. In all cases, the number density of active sites ( $N_0$ ) increases exponentially as the deposition potential changes to more negative values.

The surface properties of substrates also strongly affect nucleation and growth kinetics of metal electrodeposition. The electrochemical activity of substrates depends on their surface structure. In the case of tin electrodeposition on single-crystal copper, the number density of nuclei is significantly smaller compared to the deposition on polycrystalline substrates. For deposition on polycrystalline substrates, the number density of nuclei on copper is higher than on nickel.

Tin electrodeposition in various acid electrolyte solutions was studied. The results show that tin electrodeposition in MSA solution needs a greater overpotential to obtain a current-time profile similar to that in sulfuric acid solution. The shape of transients obtained in MSA solution is wider and decay is slower, indicating that nucleation is more difficult in MSA system.

According to classical and atomistic theories of nucleation, in all cases (except solutions with thiourea), the relationship between nucleation rate and  $1/\eta^2$  or  $\eta$  is linear, indicating that tin electrodeposition proceeds by three-dimensional phase formation and growth. The number of atoms forming the critical nucleus ( $N_{\text{crit}}$ ) consist of 0-2 atoms, suggesting that the substrates have similar activities. A “zero atomic” critical nucleus means that the active site itself plays the role of a critical nucleus, and the small size of critical nuclei suggests strong bond energy between tin atoms and the substrates. The critical Gibbs free energy ( $\Delta G_{\text{crit}}$ ) follows the sequence: Cu-S > Ni-P > Cu-P, which is consistent with the number density of active sites on the substrate surface.

The surface morphology of deposits on single-crystal copper substrate was characterized using SEM and AFM. In acid sulfate solutions without additives, SEM micrographs of tin deposits reveal that at low deposition potential, only a few well-defined crystallites were observed, and the tin crystallites had a tetragonal shape. At higher deposition potential, the number of nuclei increased considerably. From the AFM images, 3D structure of the nuclei was clearly observed. The nucleus size was almost the same, and no other small nuclei can be observed at high resolution, confirming instantaneous nucleation. Addition of thiourea to acid tin sulfate solution, SEM images show that more nuclei are obtained, and have wide distribution, indicating progressive

nucleation, in agreement with the chronoamperometric analysis. In the presence of thiourea-silver, it was found that the nucleus size is much smaller, and the number density of nuclei is significantly higher. The nuclei display a small range of nucleus sizes, indicating that tin nucleation has intermediate behavior under this condition.

The number density of nuclei in the AFM images was measured by means of Digital Instrumental Nanoscope Image Analysis software. In comparison with calculated nucleus densities, the measured values are much higher. At  $-550$  mV, the measured nucleus density is about 2 times as great as the calculated value in acid tin sulfate solution without additive. In the presence of silver-thiourea, the measured nucleus density is about 6 times as great as the calculated one.

## REFERENCE

1. A. C. Tan, *Tin and Solder Plating in the Semiconductor Industry: A Technical Guide*, Chapman & Hall, New York, 1992.
2. J. L. Martin and M. P. Toben, *Metal Finishing*, **86**, 39 (1988).
3. C. S. Chen C. C. Wan, and Y. Y. Wang, *Trans. IMF*, **76**, 54 (1998).
4. M. Carano, *Plat. Surf. Finish*, **89**, 49 (2002).
5. W. A. Proell, C. E. Adams, and B. H. Shoemaker, *Industrial and Engineering Chemistry*, **40**, 1129 (1948).
6. W. A. Proell, *US Patent 2525942*, 1950.
7. W. J. Tuszynski, *Specialty Chemicals*, **9**, 409 (1989).
8. N. Dohi, and K. Obata, *US Patent 4132610*, 1979
9. K. Obata, et al, *US Patent 4459185*, 1984.
10. K. Obata, et al, *US Patent 4555314*, 1985.
11. F. Nobel, I. Fred, B. Ostrow, and D. Schram, *US Patent 4565609*, 1986.
12. F. Nobel, et al, *US Patent 4599149*, 1986.
13. F. Nobel, et al, *US Patent 4617097*, 1986.
14. V. Opaskar, V. Canaris, and W. Willis, *US Patent 4582576*, 1986.
15. V. Opaskar, and G. Bokisa, *US Patent 4662999*, 1987.
16. R. Moshohoritou, I. Tsangaraki, and C. Kotira, *Plat. Surf. Finish*, **81**, 53 (1994).
17. S. Meibuhr and P. R. Carter, *Electrochem. Tech.*, **2**, 267 (1964).
18. G. S. Tzeng, *Plating & Surface Finishing*, **66**, 67 (1995).
19. F. J. Barry, and V. J. Cunnane, *J. Electroanal. Chem.*, **537**, 151 (2002).
20. S. Meibuhr, E. Yeager, A. Kozawa and F. Hovorka, *J. Electrochem. Soc.*, **110**, 190 (1963).

21. V. V. Gorodetski, I. P. Slutski, and V. V. Losev, *Elektrokhimiya*, **8**, 1401 (1972).
22. R. B. Bard, W. E. Stewart, and E. N. Lightfoot, *Transport Phenomena*, John Wiley & Sons, Singapore, 1980.
23. A. Aragon, M. G. Figueroa, R. E. Gana and J. H. Zagal, *J. Appl. Electrochem.*, **22**, 558 (1992).
24. K. G. Compton, A. Mendizza, and S. M. Arnold, *Corrosion*, **9**, 327 (1951).
25. S. C. Britton, *Trans. Inst. Met. Finish*, **52**, 95 (1974).
26. B-Z. Lee, and D. N. Lee, *Acta Mater.* **46**, 3701(1998).
27. N. A. J. Sabbagh, and H. J. McQueen, *Metal Finishing*, **73**, n3, 27 (1975).
28. L. Zakraysek, *Plating & Surface Finishing*, **64**, n3, 38 (1977).
29. M. C. Lin, *AT & T Bell Labs, Technical Memorandum*, 1984.
30. R. Schetty, *Circuit World*, **27**, n2, 17 (2001).
31. R. Kuhl, and S. Mills, *SMT Surface Mount Technology Magazine*, **9**, 48 (1995).
32. S. Arai, and T. Watanabe, *Materials Transactions, JIM*, **39**, 439 (1998).
33. E. Bradley, K. Snowdown, and R. Gedney, *Circuits Assembly*, **10**, 91 (1999).
34. M. Jordan, *Galvanotechnik*, **92**, 1225 (2001).
35. I. Artaki, and A. M. Jackson, *Journal of Electronic Materials*, **23**, 757 (1994).
36. W. Yang, L. E. Felton, and R. W. Messler, *Journal of Electronic Materials*, **24**, 1465 (1995).
37. N. Kubota, and E. Sato, *Electrochim. Acta*, **29**, 361 (1984).
38. N. Kubota, and E. Sato, *Electrochim. Acta*, **30**, 305 (1985).
39. J. C. Puipe, and W. Fluehmann, *Plat. Surf. Finish*, **70**, 46 (1983).
40. M. Bestetti, A. Vincenzo, and P. L. Cavallotti, *AESF SUR/FIN 2002 Proceedings, AESF Annual Technical Conference*, 745 (2002).
41. L. Oniciu and L. Muresan, *J. Appl. Electrochem.*, **21**, 565 (1991).
42. T. C. Franklin, *Surf. Coatings. Technol.*, **30**, 415 (1987).

43. S. Meibuhr, E. Yeager, A. Kosawa, and F. Hovorka, *J. Electrochem. Soc.*, **110**, 190 (1963).
44. B. Nagaraj, and C. K. Mital, *Metal Finishing*, **73**, 76 (1975).
45. A. Aragon, M. G. Figueroa, R. E. Gana, and J. H. Zagal, *J. Appl. Electrochem.*, **22**, 558 (1992).
46. Y. Nakamura, N. Kaneko, and H. Nezu, *J. Appl. Electrochem.*, **24**, 569 (1994).
47. Y. Nakamura, N. Kaneko, N. Nakamura, and H. Nezu, *J. Appl. Electrochem.*, **24**, 404 (1994).
48. N. Kaneko, N. Shinohara, and H. Nezu, *Electrochim. Acta*, **36**, 985 (1991).
49. N. Kaneko, N. Shinohara, and H. Nezu, *Electrochim. Acta*, **37**, 2403 (1992).
50. S. S. Abd El Rehim, S. M. Sayyah, and M. M. El Deeb, *Plat. Surf. Finish.*, **87**, 93 (2000).
51. G. S. Tzeng, S. H. Lin, Y. Wang, and C. C. Wan, *J. Appl. Electrochem.*, **26**, 419 (1996).
52. Y. Zhang, J. A. Abys, and C. H. Chen, *Plat. Surf. Finish.*, **85**, 105 (1998).
53. Y. Zhang, and J. A. Abys, *Circuit World*, **25**, 30 (1998).
54. Y. Zhang, I. S. Zavarine, and O. khaselev, *J. Electrochem. Soc.*, **150**, C202 (2003).
55. V. N. Kudryatsev, K. M. Tyutina, A. N. Popov, S. A. Maksimenko, and V. A. Zonin, *Plat. Surf. Finish.*, **79**, n7, 57 (1992).
56. G. Wouters, M. Bratoeva, J-P Celis, and J R. Roos, *Electrochim. Acta.*, **40**, 1434 (1995).
57. T. Kakeshita, K. Shimizu, R. Kawanaka, and T. Hasegawa, *J. Mat. Sci.*, **17**, 2560 (1982).
58. E. Gomez, E. Guaus, F. Sanz, and E. Valles, *J. Electroanal. Chem.*, **465**, 63(1999).
59. J. Torrent-Burgues, E. Guaus, and F. Sanz, *J. Appl. Electrochem.*, **32**, 225 (2002).
60. D. Pletcher, *A First Course in Electrode Processes*, Alresford Press Ltd, Hants, 1991.
61. I. Petersson, and E. Ahlberg, *J. Electroanal. Chem.*, **485**, 166 (2000); **485**, 179 (2000).
62. K. Kowal, L. Xie, R. Hug, G. Farrington, *J. Electrochem. Soc.*, **141**, 116 (1994).

63. R. Rynders, and R. Alkire, *J. Electrochem. Soc.*, **141**, 1166 (1994).
64. E. Gomez, E. Valles, P. Gorostiza, J. Servat, and F. Sanz, *J. Electrochem. Soc.*, **142**, 4091 (1995).
65. J. V. Zoval, R. M. Stiger, P. R. Biernacki, and R. M. Penner, *J. Phys. Chem.* **100**, 837 (1996).
66. B. Rashkova, B. Guel, R. T. Potzschke, G. Staikov, and W. J. Lorenz, *Electrochim. Acta.*, **43**, 3021 (1998).
67. F. Li, R. Newman, and G. Thompson, *Electrochim. Acta.*, **42**, 2455 (1997).
68. Y. G. Li, and A. Lasia, *J. Appl. Electrochem.*, **27**, 643 (1997).
69. K. Ondo, T. Murakami, F. Cerwinski, and K. Shinohara, *ISIJ International*, **37**, 140 (1997).
70. E. Barrera, M. Pardave, N. Batina, and I. Gonzalez, *J. Electrochem. Soc.*, **147**, 1787 (2000).
71. D. Grujicic, and B. Pesic, *Electrochim. Acta.*, **47**, 2901 (2002).
72. S. Floate, M. Hyde, and R. Compton, *J. Electroanal. Chem.*, **523**, 49 (2002).
73. M. Hyde, R. Jacobs, and R. Compton, *J. Phys. Chem. B*, **106**, 11075 (2002).
74. A. Radisic, A. West, and P. Searson, *J. Electrochem. Soc.*, **148**, C41 (2001)
75. A. Radisic, A. West, and P. Searson, *J. Electrochem. Soc.*, **149**, C94 (2002).
76. K. Marquez, G. Staikov, and J. W. Schultze, *Electrochimica Acta*, **48**, 875 (2003).
77. R. D. Armstrong, M. Fleischmann and H. R. Thirsk, *J. Electroanal. Chem.*, **11**, 208 (1966).
78. D. J. Astley, J. A. Harrison and H. R. Thirsk, *Trans. Faraday Soc.*, **64**, 192 (1968).
79. G. J. Hills, D. J. Schiffrin and J. Thompson, *Electrochim. Acta*, **19**, 657 (1974).
80. G. J. Hills, D. J. Schiffrin and J. Thompson, *Electrochim. Acta*, **19**, 671 (1974).
81. M. Y. Abyaneh, *Electrochim. Acta*, **27**, 1329 (1982).
82. M. Y. Abyaneh and M. Fleischmann, *Electrochim. Acta*, **27**, 1513 (1982).
83. E. Bosco and S. K. Rangarajan, *J. Electroanal. Chem.*, **134**, 213 (1982).

84. G. Gunawardena, G. J. Hills, I. Montenegro and B. Scharifker, *J. Electroanal. Chem.*, **138**, 225 (1982).
85. B. Scharifker and G. Hills, *Electrochim. Acta*, **28**, 879 (1983).
86. B. R. Scharifker and J. Mostany, *J. Electroanal. Chem.*, **177**, 13 (1984).
87. M. Sluyters-Rehbach, J. H. O. J. Wijenberg, E. Bosco, and J. H. Sluyters, *J. Electroanal. Chem.*, **236**, 1 (1987).
88. M. V. Mirkin and A. P. Nilov, *J. Electroanal. Chem.*, **283**, 35 (1990).
89. P. A. Bobbert, M. M. Wind, and J. Vlieger, *Physica A*, **146**, 69 (1987).
90. M. Y. Abyaneh, *Electrochim. Acta*, **36**, 727 (1991).
91. A. Milchev, *J. Electroanal. Chem.*, **457**, 35 (1998); **457**, 47 (1998).
92. A. Milchev, *Electrochim. Acta*, **30**, 125 (1985).
93. M. Fleischmann, M. Liler, *Trans. Faraday Soc.* **54**, 1370 (1958).
94. M. Fleischmann, H.R. Thirsk, *Trans. Faraday Soc.* **51**, 71 (1955).
95. D.J. Astley, J.A. Harrison, and H.R. Thirsk, *Trans. Faraday Soc.*, **64**, 192 (1968).
96. S. Toshev, A. Milchev and E. Vassileva, *Electrochim. Acta*, **21**, 1055 (1976).
97. A. Milchev, B. R. Scharifker and G. J. Hills, *J. Electroanal. Chem.*, **132**, 277 (1982).
98. M. Avrami, *J. Chem. Phys.* **7**, 1103 (1939).
99. M. Avrami, *J. Chem. Phys.* **8**, 212 (1940).
100. M. Avrami, *J. Chem. Phys.* **9**, 177 (1941).
101. A. Milchev, E. Michailova, I. Lesigiarska, *Electrochem. Commun.* **2**, 407 (2000).
102. J. Mostany, J. Mozota, B. Scharifker, *J. Electroanal. Chem.*, **177**, 25 (1984).
103. J. Mostany, J. Parra, B.R. Scharifker, *J. Appl. Electrochem.*, **16**, 333 (1986).
104. L. Heerman, E. Matthijs, S. Langerock, *Electrochim. Acta*, **47**, 905 (2001)
105. L. Heerman, A. Tarallo, *J. Electroanal. Chem.*, **451**, 101 (1998).
106. L. Heerman, A. Tarallo, *J. Electroanal. Chem.*, **470**, 70 (1999).



107. A. Milchev, *Contemporary Physics*, **32**, 321 (1991).
108. E. Budevski and V. Bostanov, *Electrochim. Acta*, **9**, 477 (1964)
109. E. Budevski, G. Staikov and W. J. Lorenz, *Electrochemical Phase Formation and Growth: An introduction to the Initial Stages of Metal Deposition*, VCH, Weinheim, 1996.
110. D. Kashchiev, *J. Chem. Phys.* **76**, 5098 (1982).
111. D. W. Oxtoby and D. Kashchiev, *J. Chem. Phys.* **100**, 7665 (1994).
112. M. Volmer and A. Weber, *Z. Phys. Chem.* **119**, 277 (1926).
113. D. Walton, *J. Chem. Phys.* **37**, 2182 (1962).
114. D. Walton, T. Rodin and R. W. Rollins, *J. chem. Phys.* **38**, 2698 (1963).
115. A. Milchev, S. Stoyanov, and R. Kaishev, *Thin Solid Films*, **22**, 255 (1974).
116. R. Schrebler, P. Cury, M. Orellana, H. Gomez, R. Cordova, and E. A. Dalchiele, *Electrochim. Acta*, **46**, 4309(2001).
117. B. H. Loo, *Chem. Phys. Lett.*, **89**, 346 (1982).
118. M. Fleischmann, I. R. Hill, and G. Sundholm, *J. Electroanal. Chem*, **157**, 359 (1983).
119. Z. Q. Tian, Y. Z. Lian, and M. Fleischmann, *Electrochim. Acta*, **35**, 879 (1990).
120. A. Lukomska, S. Smolinski, and J. Sobkowski, *Electrochim. Acta*, **46**, 3111 (2001).
121. D. Papapanayiotou, R. N. Nuzzo, and R. C. Alkire, *J. Electrochem. Soc.*, **145**, 3366 (1998).
122. M. Alodan, W. Smyrl, *Electrochim. Acta*, **44**, 299 (1998).
123. G. I. Lacconi, and V. A. Macagno, *Electrochim. Acta*, **39**, 2605 (1994).
124. S. Ahmad, A. A. Isab, and H. Perzanowski, *Transition Metal Chemistry*, **27**, 782 (2002).
125. T. C. Franklin, *Plat. Surf. Finish*, **81**, 62 (1994).
126. B. Reents, W. Plieth, V. A. Macagno, and G. I. Lacconi, *J. Electroanal. Chem*, **453**, 121 (1998).
127. M. Milkowska, *Electrochim. Acta*, **36**, 965 (1991).

128. M. Milkowska, *Electrochim. Acta*, **32**, 159 (1987).
129. M. Milkowska, *Electrochim. Acta*, **33**, 161 (1988).
130. G. M. Brown, and G. A. Hope, *J. Electroanal. Chem*, **382**, 179 (1995).
131. G. Carneval, and J. B Cusminsky, *J. Electrochem. Soc.*, **128**, 1215 (1981).
132. J. R. Vilche, and K. Juttner, *Electrochim. Acta*, **32**, 1567 (1987).
133. D. W. Hardesty, *J. Electrochem. Soc.*, **117**, 168 (1981).
134. N. Vinokur, B. Miller, Y. Avyigal, and R. Kalish, *J. Electrochem. Soc.*, **146**, 125 (1999).
135. J. Lee, B. Miller, X. Shi, R. Kalish, and K. Weeler, *J. Electrochem. Soc.*, **147**, 3370 (2000).
136. Y. Lin, and I. Sun, *J. Electrochem. Soc.*, **146**, 1054 (1999).

## NOMENCLATURE

A	Nucleation rate constant (1/sec)
B	Constant value depending on the geometry
C	Bulk concentration of the depositing metal ions (mol/cm <sup>3</sup> )
D	Diffusion coefficient of the depositing metal ions (cm <sup>2</sup> /sec)
e	Elementary electric charge
F	Faraday's Constant (96486 Coulombs/mole)
$\Delta G(n)$	Gibbs free energy of nucleus formation (J)
$\Delta G_{crit}$	Critical Gibbs free energy for critical nucleus formation (J)
$i_o$	Exchange current density (A/cm <sup>2</sup> )
$i(t)$	Current density (A/cm <sup>2</sup> )
$i_{max}$	Maximum Current density (A/cm <sup>2</sup> )
$J_{st}$	Steady state nucleation rate (1/sec-cm <sup>2</sup> )
M	Molecular weight of the deposited metal (g/mol)
N	The number of atoms in the nucleus
N	Number density of growing nuclei
$N_o$	Number density of active sites (1/cm <sup>2</sup> )
$N_\infty$	Number density of active sites (1/cm <sup>2</sup> )
$n_{crit}$	Number of atoms in a critical nucleus
$r_d$	Radius of diffusion zone (cm)

R	Gas constant (8.31 J/mol-K)
S	Surface area of the electrode (cm <sup>2</sup> )
S(t)	Planar area of one diffusion zone (cm <sup>2</sup> )
t	Deposition time (sec)
t <sub>max</sub>	Deposition time of the current transient maximum (sec)
T	Temperature (K)
V <sub>m</sub>	Volume occupied by one atom (cm <sup>3</sup> /mol)
z	Charge number of metal ion

## Greek Letters

$\alpha$	Dimensionless factor
$\alpha_a$	Cathodic transfer coefficient
$\alpha_c$	Anodic transfer coefficient
$\delta(t)$	Radius of the diffusion zone (cm)
$\eta$	overpotential (V)
$\theta$	Actual fraction of area covered by diffusion zones
$\theta_{ex}$	Fractional area covered by diffusion zones without overlap
$\nu$	Sweep rate (V/sec)
$\rho$	Density of the deposited metal (g/cm <sup>3</sup> )
$\sigma$	Average specific surface energy (J/cm <sup>2</sup> )
$\Phi(n)$	Total surface free energy (J)